

University of Windsor

Scholarship at UWindor

Electronic Theses and Dissertations

Theses, Dissertations, and Major Papers

7-7-2020

Lift-Off Behaviour of Fiber-Reinforced Elastomeric Bearings

Junfu Bai

University of Windsor

Follow this and additional works at: <https://scholar.uwindsor.ca/etd>

Recommended Citation

Bai, Junfu, "Lift-Off Behaviour of Fiber-Reinforced Elastomeric Bearings" (2020). *Electronic Theses and Dissertations*. 8345.

<https://scholar.uwindsor.ca/etd/8345>

This online database contains the full-text of PhD dissertations and Masters' theses of University of Windsor students from 1954 forward. These documents are made available for personal study and research purposes only, in accordance with the Canadian Copyright Act and the Creative Commons license—CC BY-NC-ND (Attribution, Non-Commercial, No Derivative Works). Under this license, works must always be attributed to the copyright holder (original author), cannot be used for any commercial purposes, and may not be altered. Any other use would require the permission of the copyright holder. Students may inquire about withdrawing their dissertation and/or thesis from this database. For additional inquiries, please contact the repository administrator via email (scholarship@uwindsor.ca) or by telephone at 519-253-3000ext. 3208.

LIFT-OFF BEHAVIOUR OF FIBER-REINFORCED ELASTOMERIC BEARINGS

By

Junfu Bai

A Thesis

Submitted to the Faculty of Graduate Studies
through the Department of Civil and Environmental Engineering
in Partial Fulfillment of the Requirements for
the Degree of Master of Applied Science
at the University of Windsor

Windsor, Ontario, Canada

2020

© 2020 Junfu Bai

Lift-Off Behaviour of Fiber-Reinforced Elastomeric Bearings

by

Junfu Bai

APPROVED BY:

N. Zamani

Department of Mechanical, Automotive & Materials Engineering

F. Ghrib

Department of Civil and Environmental Engineering

N. Van Engelen, Co-Advisor

Department of Civil and Environmental Engineering

S. Cheng, Co-Advisor

Department of Civil and Environmental Engineering

May 14, 2020

DECLARATION OF ORIGINALITY

I hereby certify that I am the sole author of this thesis and that no part of this thesis has been published or submitted for publication.

I certify that, to the best of my knowledge, my thesis does not infringe upon anyone's copyright nor violate any proprietary rights and that any ideas, techniques, quotations, or any other material from the work of other people included in my thesis, published or otherwise, are fully acknowledged in accordance with the standard referencing practices. Furthermore, to the extent that I have included copyrighted material that surpasses the bounds of fair dealing within the meaning of the Canada Copyright Act, I certify that I have obtained a written permission from the copyright owner(s) to include such material(s) in my thesis and have included copies of such copyright clearances to my appendix.

I declare that this is a true copy of my thesis, including any final revisions, as approved by my thesis committee and the Graduate Studies office, and that this thesis has not been submitted for a higher degree to any other University or Institution.

ABSTRACT

Elastomeric bearings are widely used for base isolation as well as accommodating displacements in bridges. Fiber-reinforced elastomeric bearings (FREBs) have been shown to have similar performance as steel-reinforced elastomeric bearings (SREBs). Unbonded FREBs exclude the stiff and heavy steel end plates used to mechanically fasten the bearing to the top and the bottom surfaces. Due to the lack of a connection, lift-off (i.e. the separation between the superstructure and the bearings) could occur under certain combinations of large rotations and relatively low axial stress. This causes the superstructure to partially lose contact with the bearing and thus decreases the effective part of the bearing. Furthermore, nonlinearities are developed during this process which renders the problem to be more complex than the bonded cases. Canadian and American bridge design codes (CSA S6 and AASHTO) have contradicting requirements in the regulation of lift-off.

In this thesis, the existing analytical model for bonded FREBs are illustrated and compared with numerical results. The analytical solutions of the lift-off initiation rotation and the moment-rotation relationship for unbonded FREBs are introduced. The shear strain distribution for unbonded FREBs is derived based on the existing analytical solutions. Eight infinite strip-shaped bearings with different number of layers, six bearings with different shape factor values, and four bearings with the same compressibility and extensibility index value but different material properties and geometry are simulated by using ABAQUS to validate the analytical lift-off behaviour.

It is concluded that the numerical results fit well with the analytical solutions in terms of moment-rotation relationship, and shear stress and normal stress distribution. The analytical solutions could be used to predict the real behaviour of unbonded FREBs. The numerical results of the moment-rotation relationship agree better with the analytical solutions for the bearings (both bonded and unbonded) with fewer number of layers and under smaller loads. Based on the results, lift-off could be allowed to occur, but the bearings should be carefully designed to avoid shear failure.

ACKNOWLEDGEMENTS

I express my sincere gratitude to my advisors Professor Niel Van Engelen and Professor Shaohong Cheng for their continued support and guidance throughout my graduate studies.

I would also like to thank Professor Faouzi Ghrib and Professor Nader Zamani-Kashani for their time and suggestions.

I would especially like to thank my parents for supporting me to achieve a good education and meet my goals.

TABLE OF CONTENTS

DECLARATION OF ORIGINALITY	iii
ABSTRACT	iv
ACKNOWLEDGEMENTS	v
LIST OF TABLES	viii
LIST OF FIGURES	ix
Chapter 1 Introduction	1
1.1 Background of Elastomeric Bearings	1
1.2 Motivation of the research	2
1.3 Objectives	5
Chapter 2 Literature Review.....	6
2.1 Base Isolation.....	6
2.1.1 Mechanism of Base Isolation.....	6
2.1.2 Requirements for Base Isolators	10
2.1.3 Applications of Base Isolation in Buildings.....	11
2.2 Types of Bridge Bearings and Base Isolators	13
2.2.1 SREIs and FREIs	13
2.2.2 Sliding Isolators	15
2.2.3 Rocker and pin bearings.....	17
2.2.4 Roller Bearing	17
2.2.5 Pot Bearing.....	18
2.2.6 Disc Bearing.....	19
2.3 Mechanics of Elastomeric Bearings.....	20
2.3.1 Mechanics of the reinforcement layers	20
2.3.2 Mechanical Model of FREBs.....	21
2.4 Code Provisions for Elastomeric Bearings	36
2.4.1 CSA S6 – Canadian Highway Bridge Design Code	36
2.4.2 AASHTO (2017).....	37
2.4.3 Limitations	39
Chapter 3 Stress Distribution after Lift-off Occurs	41
3.1 Shear Stress and Shear Strain Distribution	41
3.2 Normal Stress Distribution	43
Chapter 4 Numerical Simulation	45

4.1	Introduction.....	45
4.2	Scenario Description	45
4.2.1	Model validation	45
4.2.2	Validation and Investigation of lift-off behaviour	46
4.3	Model Description	49
4.3.1	Material	49
4.3.2	Parts and Interaction	50
4.3.3	Boundary Conditions and Loads.....	52
4.3.4	Element Type and Size	53
Chapter 5	Results and Discussions.....	58
5.1	Notes on Results	58
5.2	Model Validation	59
5.2.1	Vertical Behaviour	59
5.2.2	Rotational Behaviour	65
5.3	Lift-off Behaviour Validation	70
5.3.1	Effect of the Number of Layers	70
5.3.2	Effect of the Shape Factor.....	82
5.3.3	Effect of the Compressibility and Extensibility Index, λ	84
Chapter 6	Conclusions and Recommendations	89
6.1	Conclusions.....	89
6.2	Recommendations.....	93
	References.....	95
Appendix A	Bonding Levels	98
Appendix B	Deformed Shape and Mesh of FREBs	102
Appendix C	Results with 0.8 MPa Shear Modulus	109
Appendix D	Results for Bearings H1 to H6	114
Appendix E	Results for Bearings L1 to L4	121
Appendix F	Plots after Extrapolation.....	124
Vita Auctoris	129

LIST OF TABLES

Table 4-1	Second shape factor of bonded bearings.	46
Table 4-2	Second shape factor of Bearings U1 to U8.	47
Table 4-3	Maximum rotation that could be applied to Bearings U1 to U8 based on CSA S6-14.	47
Table 4-4	Details of Bearings H1 to H6.	48
Table 4-5	Details of Bearings L1 to L4.	49
Table 5-1	Error between the numerical and the analytical vertical displacement at an average compressive stress of 5 MPa.	60
Table 5-2	Analytical and numerical θ_0 for Bearings U1 to U8.	71
Table 5-3	Percent error between the numerical and the analytical M/M_0	74
Table 5-4	Numerical maximum shear stresses under the 0.01-radian rotation per layer after extrapolation and the corresponding error with respect to the analytical solutions.	78
Table 5-5	Numerical maximum shear stresses under the maximum rotation based on CSA S6-14 after extrapolation and the corresponding error with respect to the analytical solutions.	78
Table 5-6	Error between numerical and analytical maximum normal stress	79
Table 5-7	Errors of the numerical maximum shear strain after extrapolation and the analytical results for Bearing U1 to U8 under two levels of rotation.	81
Table 5-8	Numerical η for Bearing H1 to H6 and the corresponding error with respect to the analytical η	82
Table 5-9	Error between the numerical and the analytical results of the reaction moment when	83
Table 5-10	Error between the extrapolated numerical and the analytical results of the maximum shear stress when Bearings H1 to H6 are under two levels of rotation.	84
Table 5-11	Errors between the numerical and the analytical results of the maximum normal stress when Bearings H1 to H6 are under two levels of rotation.	84
Table 5-12	Analytical and the numerical results of η for Bearings L1 to L4 as well as the corresponding errors.	85
Table 5-13	Error between the numerical and the analytical results of the reaction moment when rotation equals to 0.02 radians.	87
Table 5-14	Error between the numerical and the analytical results of the maximum shear stress (extrapolated) and normal stress when rotation equals to 0.02 radians.	88
Table A 1	The magnitude of the applied rotation when the 5-layer bearing models diverge	100
Table A 2	The magnitude of the applied rotation when the 13-layer bearing models diverge	100

LIST OF FIGURES

Figure 1-1	Bridge bearing subjected to moment due to traffic.	1
Figure 1-2	Sketch of a laminated elastomeric bearing.	2
Figure 1-3	Illustration of (a) compression + bending = combined strain; (b) uplift for a bonded bearing and lift-off for an unbonded bearing.	3
Figure 1-4	Lift-off of the column-top base isolator in a building.	3
Figure 1-5	Configuration of an elastomeric pad subjected to compression, shear and moment identifying the location of maximum shear strain.	5
Figure 2-1	Illustration of base isolation (a) original position, (b) only consider the ground motion, and (c) final position.	7
Figure 2-2	Free-body diagram of the oscillator.	8
Figure 2-3	Transmission ratio as a function of frequency ratio for various levels of damping.	10
Figure 2-4	Elastic design spectrum (adapted from Chopra (2012)).	11
Figure 2-5	Base isolation in the US (a) Foothill Communities Law and Justice Center (Angeles Contractor Inc., 2019); (b) Los Angeles City Hall (Expedia, 2019).	12
Figure 2-6	Lord Strathcona elementary school - heritage classroom building (Ausenco, 2017).	12
Figure 2-7	Lead-plug bearing (D.S. Brwon, 2019).	14
Figure 2-8	Different kinds of isolators (a) friction pendulum system; (b) TFP system.	16
Figure 2-9	Sketch of (a) a rocker bearing; (b) a pin bearing.	17
Figure 2-10	Sketch of (a) single roller bearing; (b) multiple roller bearing.	18
Figure 2-11	Sketch of (a) fixed pot bearing; (b) guided pot bearing; (c) free pot bearing.	18
Figure 2-12	Sketch of (a) fixed disc bearing; (b) guided disc bearing; (c) free disc bearing.	20
Figure 2-13	Configuration of bearings subjected to an axial compression load (a) with no reinforcement; (b) with reinforcement.	21
Figure 2-14	Coordinate system for an infinite strip pad with thickness t and width $2b$	22
Figure 2-15	Displacement field of elastomeric pad under pure compression.	23
Figure 2-16	Force development in the reinforcement.	26
Figure 2-17	Elastomeric pad under pure bending.	30
Figure 2-18	Lift-off: Assumed bearing behaviour (Stanton & Roeder, 2008).	38
Figure 4-1	Sketch of Bearing (a) B2; (b) U2.	51
Figure 4-2	Convergence study of general behaviour for B-FREB (a) pure compression; (b) pure bending.	54

Figure 4-3	Convergence study of local behaviour for B-FREB (a) pure compression; (b) pure bending.	55
Figure 4-4	Convergence study for U-FREB (a) general behaviour; (b) local behaviour..	56
Figure 5-1	Vertical compression behaviour of B-FREBs.	59
Figure 5-2	Compression modulus under different σc values.	60
Figure 5-3	Error between the analytical solutions and the numerical results of the compression modulus.	61
Figure 5-4	Stress distribution of the five-layer bearing B2 under compression load (a) S11 (σ_{xx}); (b) S22 (σ_{zz}); (c) S33 (σ_{yy}); (d) S12 (τ_{xz}).	62
Figure 5-5	Paths selected for comparison of the stress distributions under compression.	63
Figure 5-6	Analytical and numerical normal stress distribution along the bearing width under pure compression (a) Path-1; (b) Path-2.....	64
Figure 5-7	Analytical and numerical shear stress distribution of an intermediate elastomeric layer under pure compression (a) Path-3; (b) Path-4.	65
Figure 5-8	Rotational behaviour of B-FREBs.	66
Figure 5-9	Bending modulus as a function of rotation.	67
Figure 5-10	Error between the analytical solutions and the numerical results of the bending modulus.	67
Figure 5-11	Stress distribution of the five-layer bearing B2 under pure bending (a) S11 (σ_{xx}); (b) S22 (σ_{zz}); (c) S33 (σ_{yy}); (d) S12 (τ_{xz}).	68
Figure 5-12	Analytical and numerical normal stress distribution along the width under pure bending (a) Path-1; (b) Path-2.....	69
Figure 5-13	Analytical and numerical shear stress distribution of an intermediate rubber layer under pure bending (a) Path-3; (b) Path-4.	69
Figure 5-14	Moment-rotation relationship for Bearings (a) U1 to U4; (b) U5 to U8.	72
Figure 5-15	Normalized moment-rotation relationship for Bearings (a) U1 to U4; (b) U5 to U8.	72
Figure 5-16	Deformed shape of Bearing (a) U1; (b) U4; (c) U8 under 0.01 radians rotation per layer and 5 MPa compression.	73
Figure 5-17	Error between the numerical and the analytical results of the normalized moment when the normalized rotation equals to 2, 3.38, and 7.	74
Figure 5-18	Shear stress distribution when rotation per layer is 0.01 radians for (a) Bearings U1 to U4; (b) Bearings U5 to U8.	75
Figure 5-19	Shear stress distribution when rotation is the maximum permitted from CSA S6-14 for (a) Bearings U1 to U4; (b) Bearings U5 to U8.....	76
Figure 5-20	Deformed shape of Bearing (a) U1; (b) U4; (c) U8 when the normalized rotation is 3.38.	76
Figure 5-21	Shear stress distribution when the normalized rotation equals to 3.38 after extrapolation for (a) Bearings U1 to U4; (b) Bearings U5 to U8.	77

Figure 5-22	Normal stress distribution along the top of the second elastomeric layer when rotation is the maximum from CSA S6-14 for (a) Bearings U1 to U4; (b) Bearings U5 to U8.	79
Figure 5-23	Normal stress distribution along the middle of the second elastomeric layer when rotation is the maximum from CSA S6-14 for (a) Bearings U1 to U4; (b) Bearings U5 to U8.	79
Figure 5-24	Shear strain distribution when rotation per layer is 0.01 radians for (a) Bearings U1 to U4; (b) Bearings U5 to U8.	80
Figure 5-25	Shear strain distribution when rotation is the maximum from CSA S6-14 for (a) Bearings U1 to U4; (b) Bearings U5 to U8.	80
Figure 5-26	Shear stress distribution when rotation is the maximum from CSA S6-14 for Bearing (a) H1; (b) H6.	83
Figure 5-27	Deformed shape of Bearings L1 to L4 under the combination of compression (5MPa) and rotation (0.02 radians)	86
Figure 5-28	Normalized moment as a function of normalized rotation for Bearings L1 to L4.	87
Figure 5-29	Analytical and numerical shear stress distribution as a function of x/b for Bearings L1 to L4.	88
Figure 5-30	Analytical and numerical normal stress distribution as a function of x/b for Bearings L1 to L4.	88
Figure A 1	Sketches of a 5-layer bearing with different bonding levels (a) Bearing 5-1; (b) Bearing 5-2; (c) Bearing 5-3; (d) Bearing 5-4; (e) Bearing 5-5; (f) Bearing 5-6; (g) Bearing 5-7.	98
Figure A 2	Moment-rotation relationship for different bonding levels of the (a) 5-layer bearing; (b) 13-layer bearing.	99
Figure A 3	Shear stress distribution of the second elastomeric layer top surface under specific rotation for different bonding levels of the (a) 5-layer bearing; (b) 13-layer bearing.	101
Figure B 1	Deformed shape for Bearing (a) B1; (b) B2; (c) B3; (d) B4; (e) B5 under pure compression (5 MPa).	102
Figure B 2	Deformed shape for Bearing (a) B1; (b) B2; (c) B3; (d) B4; (e) B5 under pure rotation (0.01 radians).	103
Figure B 3	The deformed shape when under the combination of 5 MPa compression and 0.01-radian rotation per layer for Bearing (a) U1; (b) U2; (c) U3; (d) U4; (e) U5; (f) U6; (g) U7; (h) U8.	104
Figure B 4	The deformed shape when under the combination of 5 MPa compression and the rotation that is the maximum from CSA S6-14 for Bearing (a) U1; (b) U2; (c) U3; (d) U4; (e) U5; (f) U6; (g) U7; (h) U8.	105
Figure B 5	Deformed shape of Bearing (a) H1; (b) H2; (c) H3; (d) H4; (e) H5; (f) H6 under the combination of 5 MPa compression and the rotation that makes the analytical $\eta = 0.7$	106
Figure B 6	Meshing of Bearing B3 when (a) no load is applied; (b) under 5 MPa compression; (c) under 0.01-radian pure rotation.	107

Figure B 7	Meshing of Bearing U3 when (a) no load is applied; (b) under the combination of 5 MPa compression and the maximum rotation based on CSA S6-14; (c) under the combination of 5 MPa compression and 0.01-radian rotation per layer.	108
Figure C 1	Force-displacement relationship of B-FREBs.	109
Figure C 2	Compressive modulus under different average compressive stress.	109
Figure C 3	Error between the numerical results and the analytical solutions of compressive modulus.	110
Figure C 4	Analytical and numerical normal stress distribution along the width under pure compression (a) Path-1; (b) Path-2.	110
Figure C 5	Analytical and numerical shear stress distribution of the intermediate rubber layer under pure compression (a) Path-3; (b) Path-4.	111
Figure C 6	Rotational behaviour of B-FREBs.	111
Figure C 7	Bending modulus as a function of rotation.	112
Figure C 8	Error between the analytical solutions and the numerical results of the bending modulus.	112
Figure C 9	Analytical and numerical normal stress distribution along the width under pure bending (a) Path-1; (b) Path-2.	113
Figure C 10	Analytical and numerical shear stress distribution of the intermediate rubber layer under pure bending (a) Path-3; (b) Path-4.	113
Figure D 1	Moment-rotation relationship for Bearing (a) H1; (b) H2; (c) H3; (d) H4; (e) H5; (f) H6 up to the rotation that make the analytical $\eta = 0.7$	115
Figure D 2	Moment-rotation relationship for Bearing (a) H1; (b) H2; (c) H3; (d) H4; (e) H5; (f) H6 up to the maximum rotation based on CSA S6-14.	116
Figure D 3	Shear stress distribution along the top surface of the second elastomeric layer for Bearing (a) H1; (b) H2; (c) H3; (d) H4; (e) H5; (f) H6 under the rotation that makes the analytical $\eta = 0.7$	117
Figure D 4	Shear stress distribution along the top surface of the second elastomeric layer for Bearing (a) H1; (b) H2; (c) H3; (d) H4; (e) H5; (f) H6 under the maximum rotation based on CSA S6-14.	118
Figure D 5	Normal stress distribution along the middle path of the second elastomeric layer for Bearing (a) H1; (b) H2; (c) H3; (d) H4; (e) H5; (f) H6 under the rotation that makes the analytical $\eta = 0.7$	119
Figure D 6	Normal stress distribution along the middle path of the second elastomeric layer for Bearing (a) H1; (b) H2; (c) H3; (d) H4; (e) H5; (f) H6 under the maximum rotation based on CSA S6-14.	120
Figure E 1	Moment-rotation relationship for Bearing (a) L1; (b) L2; (c) L3; (d) L4 up to a 0.02-radian rotation.	121
Figure E 2	Shear stress distribution along the top surface of the second elastomeric layer for Bearing (a) L1; (b) L2; (c) L3; (d) L4 under a 0.02-radian rotation.	122
Figure E 3	Normal stress distribution along the middle path of the second elastomeric layer for Bearing (a) L1; (b) L2; (c) L3; (d) L4 under 0.02-radian rotation.	123

Figure F 1	Shear stress distribution when the rotation per layer is 0.01 radians after extrapolation for (a) Bearings U1 to U4; (b) Bearings U5 to U8.	124
Figure F 2	Shear strain distribution when the rotation per layer is 0.01 radians after extrapolation for (a) Bearings U1 to U4; (b) Bearings U5 to U8.	124
Figure F 3	Shear strain distribution when the rotation is the maximum from CSA S6-14 for (a) Bearings U1 to U4; (b) Bearings U5 to U8.	125
Figure F 4	Shear stress distribution along the top surface of the second elastomeric layer after extrapolation for Bearing (a) H1; (b) H2; (c) H3; (d) H4; (e) H5; (f) H6 under the rotation that makes the analytical $\eta = 0.7$	126
Figure F 5	Shear stress distribution along the top surface of the second elastomeric layer after extrapolation for Bearing (a) H1; (b) H2; (c) H3; (d) H4; (e) H5; (f) H6 under the maximum rotation based on CSA S6-14.	127
Figure F 6	Shear stress distribution along the top surface of the second elastomeric layer after extrapolation for Bearing (a) L1; (b) L2; (c) L3; (d) L4 under a 0.02-radian rotation.	128

Chapter 1 Introduction

1.1 Background of Elastomeric Bearings

Laminated elastomeric bearings, which are normally placed between the superstructure and the substructure, are widely used in bridges and buildings. For bridges, they are installed between deck and piers and/or deck and abutments to accommodate the potentially harmful displacement (vertical, lateral and rotational) due to effects such as traffic loads and temperature change (Oladimeji, 2012), without causing damage due to high stress. They could also be designed as base isolators to protect structures from seismic loadings. This technique is called base isolation.

Elastomeric bearings in both buildings and bridges are not only subjected to different types of load (compression, shear and moment) during an earthquake, but also the loads caused by wind, traffic, etc. For example, when a vehicle brakes suddenly on the deck, the friction between the tires and the ground would be transferred to the bearings as a shear force. Also, as shown in Figure 1-1, vehicle self-weight generates moment in the supports. The difference in support moment causes moment in the bearings, which in turn induces the rotational behaviour of the bearings.



Figure 1-1 Bridge bearing subjected to moment due to traffic.

A typical laminated elastomeric bridge bearing consists of alternating layers of elastomer and reinforcement bonded to each other, as shown in Figure 1-2. The elastomeric layers provide horizontal flexibility due to the low shear modulus of the elastomer. The reinforcement layers develop the high vertical and rotational stiffness of the bearing required for stability and to support the high vertical loads.



Figure 1-2 Sketch of a laminated elastomeric bearing.

Traditionally, steel shims play the role of the reinforcement layers, and this kind of bearing is called a steel-reinforced elastomeric bearing (SREB). Alternatively, when fiber is used as the reinforcement, it is called a fiber-reinforced elastomeric bearing (FREB) (Al-Anany & Tait, 2015). SREBs are widely used in engineering, but recent research (Tsai & Kelly, 2001) show that FREBs may be more economical and perform better than SREBs.

Elastomeric bearings can be further classified into two categories, i.e. bonded and unbonded, in terms of the interaction between the upper and the lower surfaces to the superstructure and substructure (Al-Anany & Tait, 2015). For a FREB, if rigid steel end-plates are bonded to the top and the bottom of the bearing to fasten it to the superstructure and the substructure, it is called a bonded FREB (B-FREB); whereas if the bearing is simply placed between the superstructure and the foundation, it is termed as an unbonded FREB (U-FREB).

1.2 Motivation of the research

When subjected to the self-weight of the superstructure compressive strain is generated in the bearings. For B-FREB, if it is also subjected to bending moment, and the amplitude of the tensile strain at the edge caused by the bending moment is higher than the compressive strain caused by the vertical load, then the edge would have a net tensile strain, as shown in Figure 1-3 (a). The upper surface of the B-FREB is bonded to the top end-plate, and it will follow the contour of the end-plate to move upward. This phenomenon is called uplift. However, for U-FREB, the upper surface won't follow the upward movement of the superstructure and a separation occurs, as illustrated in Figure 1-3 (b). Such separation is called lift-off (Stanton & Roeder, 2008).

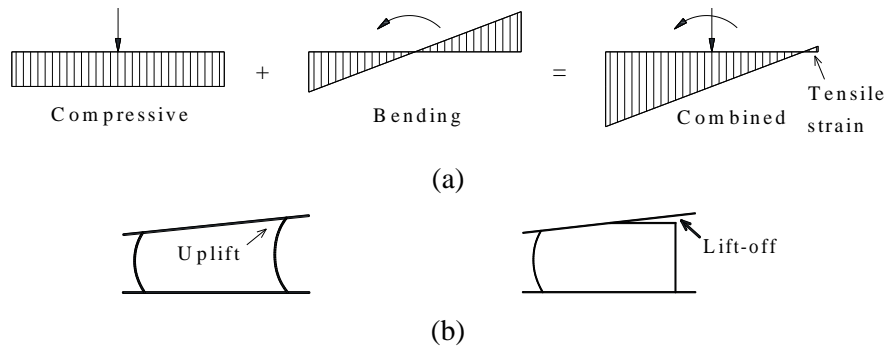


Figure 1-3 Illustration of (a) compression + bending = combined strain; (b) uplift for a bonded bearing and lift-off for an unbonded bearing.

Lift-off could also occur in buildings with U-FREBs when they are installed on the top of the first floor columns, which are referred to as column-top base isolators. As shown in Figure 1-4, when the building is subjected to a shear force, the columns would deflect laterally and the top surface of the column would rotate, which may cause lift-off of an U-FREB. In this case, the loading condition for the bearing becomes more complicated since it is subjected to the combination of axial load, moment and shear forces.

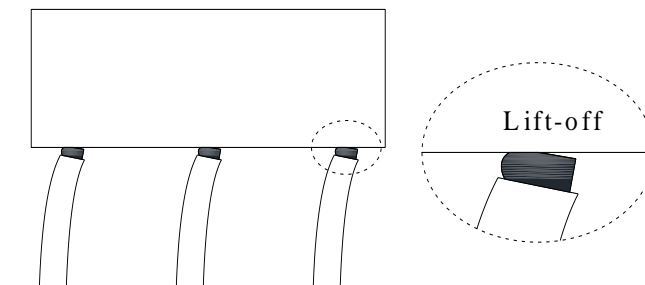


Figure 1-4 Lift-off of the column-top base isolator in a building.

The Canadian Highway Bridge Design Code (CSA S6-19 (2019)) and the AASHTO (American Association of State Highway and Transportation Officials) LRFD Bridge Design Specifications (2017) have contradicting provisions on lift-off towards SREBs. In the previous edition of CSA (S6-14), uplift for B-SREBs (bonded steel-reinforced elastomeric bearings) was constrained, but there was no clear statement about lift-off for unbonded ones. However, the latest edition of CSA (S6-19) updates their provisions to explicitly state that lift-off is to be prevented. In the previous editions of AASHTO (before AASHTO (2010)), lift-off was prevented. But in AASHTO (2010)

and all the editions after, the no-lift-off provision have been removed. Also, the two codes only consider SREBs, and there are no provisions about FREBs. Therefore, it is necessary to give an overall instruction about the lift-off behaviour for FREBs such that the contradiction between codes can be appropriately rectified and fiber reinforcement included.

The analytical solutions of the compression modulus and bending modulus of a steel-reinforced elastomeric pad (based on one layer of rubber with the upper and lower surfaces bonded to the reinforcement layers) considering the compressibility of rubber have been derived based on four different geometric shapes: infinite strip, rectangular, circular and annular (Kelly & Konstantinidis, 2011). The bending and compressive behaviour of the infinite strip pad considering both the rubber compressibility and the fiber extensibility has been derived by Kelly & Takhirov (2002). Al-Anany & Tait (2015) compared these analytical solutions with numerical results and found they agreed well with each other.

Although both CSA and AASHTO consider lift-off, they have limited provisions and lack any consideration of FREBs. In a recent work by Van Engelen (2019), the bending behaviour of U-FREB was studied considering the lift-off behaviour of the bearing. The developed solutions lacked validation with finite element analysis, therefore, it is necessary to compare this analytical solution to the numerical result for validation.

Figure 1-5 illustrates the configuration of an elastomeric pad subjected to pure compression, pure shear and pure moment, respectively. The small rectangular rubber element before deformation becomes a parallelogram after applying loads to it, which reflects the location of maximum shear strains in the bearing (Stanton & Roeder, 2008). High shear strain may cause shear failure in the bearing such as tensile debonding and shear delamination (Stanton & Roeder, 2008), and there is a limitation towards the maximum shear strain developed in elastomer in both codes (AASHTO and CSA) to prevent such failure. In order to make comments on the lift-off behaviour, it is of great importance to study the maximum shear strain of unbonded bearings.

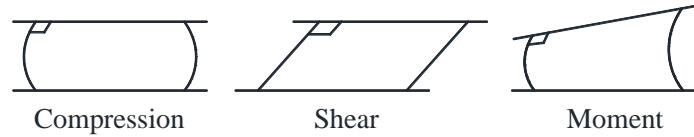


Figure 1-5 Configuration of an elastomeric pad subjected to compression, shear and moment identifying the location of maximum shear strain.

1.3 Objectives

The objectives of this research are to:

- use finite element simulations to validate the analytical solution of the bending behaviour and the lift-off initiation rotation of the unbonded infinite strip elastomeric bearing derived by Van Engelen (2019);
- derive and validate with FEA the analytical shear stress distribution and the maximum shear stress for unbonded bearings under the combination of compression and rotation; and,
- conduct a parametric study on the lift-off behaviour of FREBs by varying the number of layers, shape factor values, and keeping same λ but varying the material properties and bearing geometry, to provide recommendations for design.

Chapter 2 Literature Review

2.1 Base Isolation

Engineering considerations are not limited to the structures themselves; extra systems could be introduced to improve force transmission in the structures and resist the earthquake. Such systems are called structural vibration control systems. They can be classified into two basic categories, which are passive and active control systems (Buckle, 2000). The operation of passive control system does not require any additional energy, it is activated by the vibration of the structure itself (Buckle, 2000). The active control system is much more efficient than the passive one, but it needs a large amount of external energy to operate.

Base isolation is one of the most widely used passive seismic resistance techniques. It is achieved by introducing structural elements with a low horizontal stiffness (i.e. isolators) between the superstructure and the foundation (Naeim & Kelly, 1999). By this approach, the fundamental frequency of the structure would be lower, which in turn could reduce the seismic response of the structures. In addition, the damping of the bearings will dissipate energy during earthquakes, which also protects the structure from strong ground motion. The dynamic analysis associated with base isolation is briefly reviewed in the following section.

2.1.1 Mechanism of Base Isolation

Figure 2-1 illustrates the mechanism of base isolation. As shown in Figure 2-1 (a), an oscillator with mass, m , is connected to the ground by a horizontal linear spring with stiffness, k , and a horizontal linear viscous damper with damping coefficient, c . The single-degree-of-freedom system is subjected to ground motion excitation in terms of a harmonic ground displacement in the horizontal direction in the form of

$$u_g(t) = u_{g0} \sin \bar{\omega} t \quad (2.1)$$

where the subscript g represents “ground”, u_{g0} is the amplitude or maximum value of the ground displacement, $\bar{\omega}$ is the exciting frequency, and t is time. Figure 2-1 (a) shows the original position of the system. In order to illustrate the motion of the system more clearly, the ground motion and the deformation of the spring and the damper are illustrated separately in Figure 2-1 (b) and (c). The difference between the oscillator position in Figure 2-1 (a) and Figure 2-1 (c) represents the total displacement of the oscillator, which is designated by $u_t(t)$; the difference between the oscillator position in Figure 2-1 (b) and Figure 2-1 (c) represents the relative displacement, $u_r(t)$, between the oscillator and the ground. Therefore:

$$u_t(t) = u_r(t) + u_g(t) \quad (2.2)$$

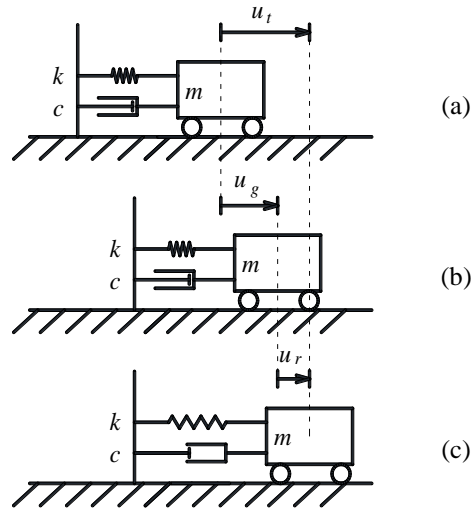


Figure 2-1 Illustration of base isolation (a) original position, (b) only consider the ground motion, and (c) final position.

The free-body diagram of the oscillator is shown in Figure 2-2, where \dot{u}_r represents the relative velocity and \ddot{u}_t the total acceleration. The gravity force in the vertical direction is cancelled out with the reaction force. In the horizontal direction, $c\dot{u}_r$, ku_r and $m\ddot{u}_t$ represent the damping force, the spring force and the inertia force, respectively. The equilibrium equation in the horizontal direction is

$$m\ddot{u}_t + c\dot{u}_r + ku_r = 0 \quad (2.3)$$

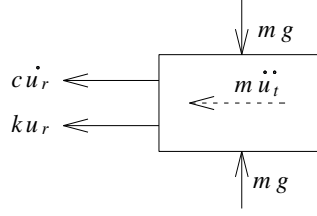


Figure 2-2 Free-body diagram of the oscillator.

The total acceleration of the oscillator, according to Eq. (2.2), is given by

$$\ddot{u}_t(t) = \ddot{u}_r(t) + \ddot{u}_g(t) \quad (2.4)$$

After substituting the second derivative of $u_g(t)$ from Eq. (2.1) into Eq. (2.4), it becomes

$$\ddot{u}_t(t) = \ddot{u}_r(t) - \bar{\omega}^2 u_{g0} \sin \bar{\omega} t \quad (2.5)$$

Substituting Eq. (2.5) into Eq. (2.3) and moving the ground motion part to the right hand side as the excitation force gives

$$m\ddot{u}_r + c\dot{u}_r + ku_r = m\bar{\omega}^2 u_{g0} \sin \bar{\omega} t \quad (2.6)$$

The solution of the steady-state response is

$$u_r(t) = \rho \sin(\bar{\omega} t - \varphi) \quad (2.7)$$

where ρ is the steady-state response amplitude expressed as

$$\rho = u_{g0} \frac{r^2}{\sqrt{(1 - r^2)^2 + (2\zeta r)^2}} \quad (2.8)$$

and the phase angle φ is expressed as

$$\varphi = \tan^{-1} \frac{2\zeta r}{1 - r^2} \quad (2.9)$$

ζ is the damping ratio which is defined as

$$\zeta = \frac{c}{2m\omega} \quad (2.10)$$

ω is the circular frequency of the system which has the definition of

$$\omega = \sqrt{k/m} \quad (2.11)$$

$r = \bar{\omega}/\omega$ is the frequency ratio between the excitation frequency of the ground motion and the natural frequency of the structure. The total displacement of the oscillator becomes

$$u_t(t) = \Lambda \sin(\bar{\omega}t - \gamma) \quad (2.12)$$

where the peak amplitude of the total transmitted displacement

$$\Lambda = u_{g0} \sqrt{\frac{1 + (2\zeta r)^2}{(1 - r^2)^2 + (2\zeta r)^2}} \quad (2.13)$$

and the phase angle γ has the expression of

$$\gamma = \tan^{-1} \frac{2\zeta r^3}{(1 - r^2) + 4\zeta^2 r^2} \quad (2.14)$$

The transmission ratio, TR, is defined as

$$\text{TR} = \frac{\Lambda}{u_{g0}} = \sqrt{\frac{1 + (2\zeta r)^2}{(1 - r^2)^2 + (2\zeta r)^2}} \quad (2.15)$$

The relationship between the TR and the frequency ratio r for different ζ values are shown in Figure 2-3.

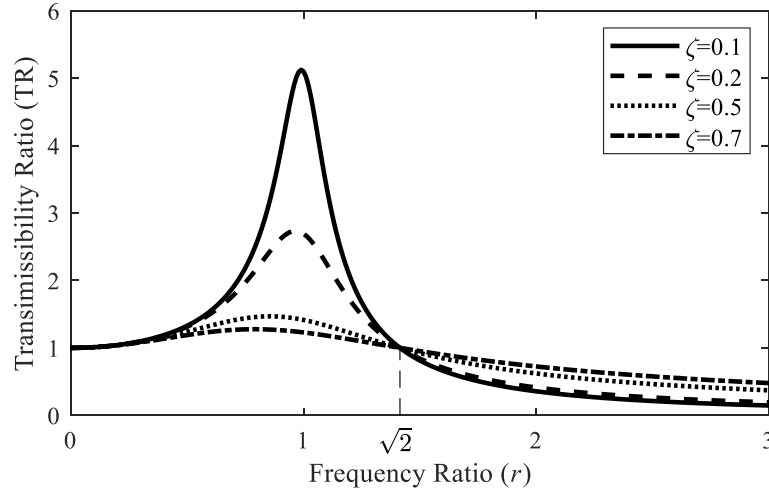


Figure 2-3 Transmission ratio as a function of frequency ratio for various levels of damping.

In Figure 2-3, when r is less than about one, the transmission ratio increases with the increase of r (lower damping ratio results in a greater increase); after reaching a maximum it decreases rapidly with increasing r . When r surpasses $\sqrt{2}$, TR becomes less than one which means the transmitted displacement of the oscillator is smaller than the ground motion and the objective of base isolation is achieved. In order to increase r to such level, the angular frequency of the structure, ω , should be reduced. According to Eq. (2.11), this could be achieved by either decreasing the stiffness k or increasing the mass m . During design, m corresponds to the mass of superstructure which cannot be changed efficiently. However, low stiffness base isolators can be installed between the superstructure and the substructure to mitigate vibrations caused by ground motions.

2.1.2 Requirements for Base Isolators

There are three basic requirements for base isolators, as summarized by Derham et al. (1985). Firstly, the bearings or isolators should have a high vertical stiffness to support the superstructure. Also, the high vertical stiffness of bearings could reduce the vertical response of the structure subjected to the vertical component of the earthquake load. Secondly, the horizontal stiffness of the

bearing should be small enough to lengthen the natural period of the structure. According to the elastic design spectrum shown in Figure 2-4 adapted from Chopra (2012), by lengthening the natural period, the pseudo-acceleration is reduced at the cost of increasing displacement. Thirdly, the bearings should contain sufficient damping to dissipate energy. As illustrated in Figure 2-4, this will reduce both the amplitude of the deformation and the pseudo-acceleration.

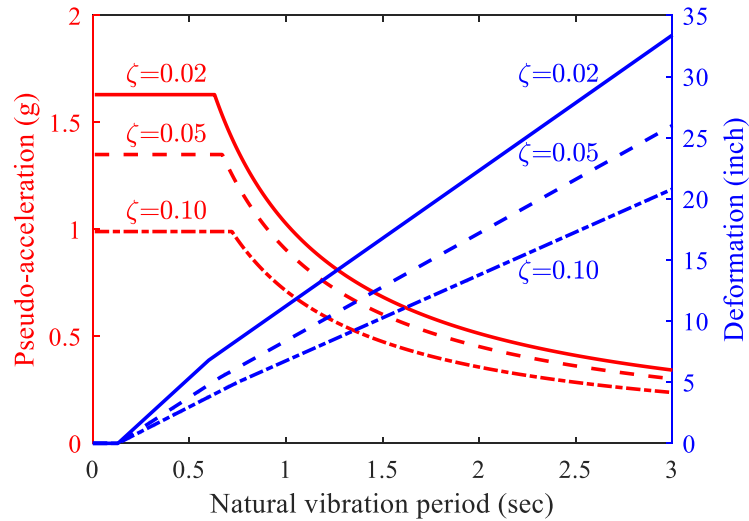


Figure 2-4 Elastic design spectrum (adapted from Chopra (2012)).

2.1.3 Applications of Base Isolation in Buildings

There are many base-isolated buildings in the world. The first base-isolated building in the United States was the Foothill Communities Law and Justice Center, and it is also the first building isolated by high-damping natural rubber bearings in the world (Naeim & Kelly, 1999). It is situated at about 97 km (60 miles) east of downtown Los Angeles in the city of Rancho Cucamonga (Naeim & Kelly, 1999). The building was constructed in 1985 with the total cost \$38 million, and there are 98 bearings used as isolators.

Also, some buildings were retrofitted using base isolation to preserve historic fabric (Naaseh, 1995; Naeim & Kelly, 1999). The Los Angeles City Hall was completed in 1982 and was damaged in the 1994 Northridge earthquake (Naeim & Kelly, 1999). The building was then retrofitted by placing it on top of an isolation system consisting of about 475 high-damping rubber isolators, 60 sliding

isolators with the supplement of 52 viscous dampers in order to reduce the seismic response (Naeim & Kelly, 1999). In addition, 12 viscous dampers are mounted between the 20th and 26th floors to control inter-story drifts (Naeim & Kelly, 1999).

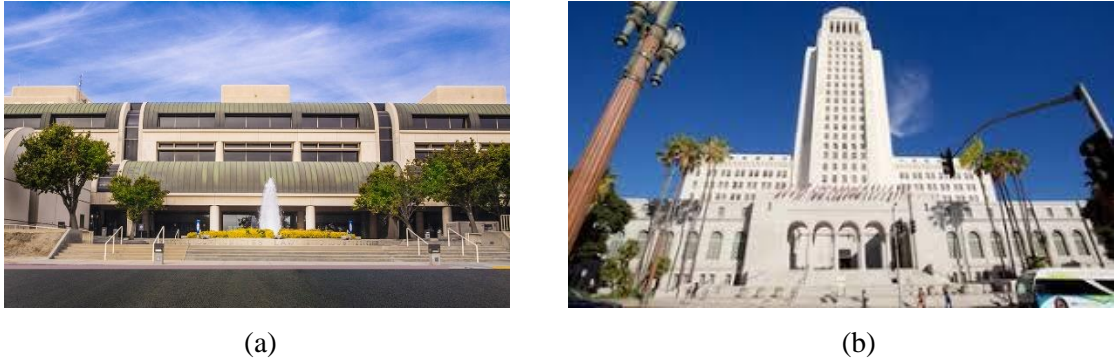


Figure 2-5 Base isolation in the US (a) Foothill Communities Law and Justice Center (Angeles Contractor Inc., 2019); (b) Los Angeles City Hall (Expedia, 2019).

Vancouver's Lord Strathcona Elementary School is one of the oldest continuously operating schools in Canada. The seismic upgrade of the heritage (1897) three storey load bearing brick/stone building of the school was done by using base isolation in 2016 (Ausenco, 2017). The existing load bearing walls were demolished, together with constructing new floor slabs, columns and beams. Twelve lead core rubber bearings and 18 stainless-Teflon sliders were installed between the superstructure and a new rigid concrete foundation (the dotted line shown in Figure 2-6).



Figure 2-6 Lord Strathcona elementary school - heritage classroom building (Ausenco, 2017).

In China, the application of base isolation started in 1991, and increased significantly after the 2008 Wenchuan earthquake. In 2013, during the Lushan earthquake, two closely situated primary schools

showed quite different behaviours. For the one which was conventionally built (i.e. not base-isolated), the peak ground acceleration, 0.2 g, was amplified to 0.72 g at the top (Zhou, 2015; Zhou & Tan, 2013). However, for the isolated one, the acceleration peak was reduced to 0.12 g, only 1/6 of the former one.

In Japan, where earthquakes often occur, the base isolation technique is frequently used. The four storey National Western Art Le Corbusier Museum in Tokyo was retrofitted by installing high damping natural rubber bearings in 1999 (Saito, 2015). The isolation system performed well during the 2011 Tohoku earthquake, reducing the peak ground accelerations along the two horizontal directions respectively from 0.19 g and 0.27 g to 0.08 g and 0.10 g at the top (Saito, 2015).

2.2 Types of Bridge Bearings and Base Isolators

There are mainly two kinds of base isolators, which are elastomeric isolators and sliding isolators (Naeim & Kelly, 1999), and they could also be used as bridge bearings. Other types of bridge bearings are rocker and pin bearings, roller bearings, curved bearings, pot bearings and disc bearings.

2.2.1 SREIs and FREIs

The low horizontal stiffness of the elastomeric isolator is controlled by the low shear modulus of the rubber; whereas the high vertical stiffness is achieved by composite action with the reinforcement layers. The damping property of this kind of isolator can be increased by using high-damping rubber or inserting one or more lead-plugs to the bearing (Naeim & Kelly, 1999), as shown in Figure 2-7. The term rubber here refers to an elastomer which is either natural or synthetic rubber, such as neoprene (Belivanis, 2017).

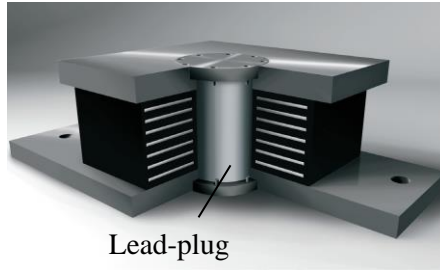


Figure 2-7 Lead-plug bearing (D.S. Brown, 2019)

Compared with a SREB, a FREB has several advantages. Firstly, steel is heavy and makes up the dominating weight of a SREB, but fiber is much lighter than steel which results in a lighter isolator and that is easier to transport and install. Secondly, the manufacturing process of a FREB can be much simpler than that for a SREB, which also results in a significant labour and cost reduction. For both of them, the rubber and reinforcement layers are bonded together by vulcanization, which is a process of adding chemical material into rubber and subjecting the raw rubber to high pressure and temperature (Stanton & Roeder, 2008). It not only changes the engineering properties of the rubber, but also forms it to the shape of the mold. But before this process, for a SREB, the steel plates should be cleaned to prevent it from corrosion and to achieve a better bonding effect with the rubber layers during vulcanization. However, fiber does not need such treatment because it will not corrode and rubber could fit into small fiber grids to achieve a good bonding without acid cleaning the fiber. SREBs also require a rubber cover added to the side surfaces to protect the steel (also achieved in vulcanization process), but a FREB does not need this. Due to this reason, a FREB could be created by cutting a large piece into the required shape and size, which is not applicable for SREBs (Das & Dutta, 2012). Therefore, using FREBs could save much expense and labour.

Furthermore, steel reinforcement is assumed to be inextensible and rigid in flexure. The fiber reinforcement is made up of individual fibers coiled and grouped together into cords (Kelly & Takhirov, 2001) and is flexible in bending and extensible in tension. Therefore, the analytical model describing SREBs and FREBs are different, the latter is more complicated.

2.2.2 Sliding Isolators

There are several kinds of sliding isolators discussed by Girish & Pranesh (2015) and Moeindarbari & Taghikhany (2012) such as the pure friction system (PF system), the friction pendulum system (FPS), the triple pendulum system (TFP), the conical friction pendulum isolator (CFPI) and the polynomial friction pendulum isolator (PFPI). Only the first three systems, i.e. the PF system, the FPS and the TFP, are introduced here. The sliding isolator works based on the principle of friction (Girish & Pranesh, 2015).

In the PF system, two flat stainless steel plates are added between the superstructure and the foundation. The upper plate slides over the lower one under the condition that the excitation force is greater than the static friction force. The structure resting on the upper plate is considered as a rigid body. The behaviour of the isolator depends on the friction coefficient of the slider (Girish & Pranesh, 2015). A lower friction coefficient would result in less shear transmitted, but this could also cause large sliding and residual displacement. In order to avoid unnecessary movement, the friction coefficient needs to be increased. However, this could make the isolator insensitive to the excitation, which means the isolator would not be activated under ground motion due to small scale earthquakes. PF system is seldom used due to its unrecoverable displacement.

The FPS overcomes the drawback of residual movement in the PF system by applying the principle of pendulum motion. As shown in Figure 2-8 (a), the FPS has an articulated slider with polytetrafluoroethylene (PTFE) coating. The slider can slide over the stainless steel concave surface of the concave plate under excitation to achieve isolation (Naeim & Kelly, 1999). After an earthquake, the slider moves back to the original location under the gravitational force, which restores the structure and decreases the residual displacement (Girish & Pranesh, 2015; Naeim & Kelly, 1999). During ground motion, energy is dissipated by the friction between the slider and the concave surface. The natural period of the structure is controlled by the radius of the concave surface (Naeim & Kelly, 1999).

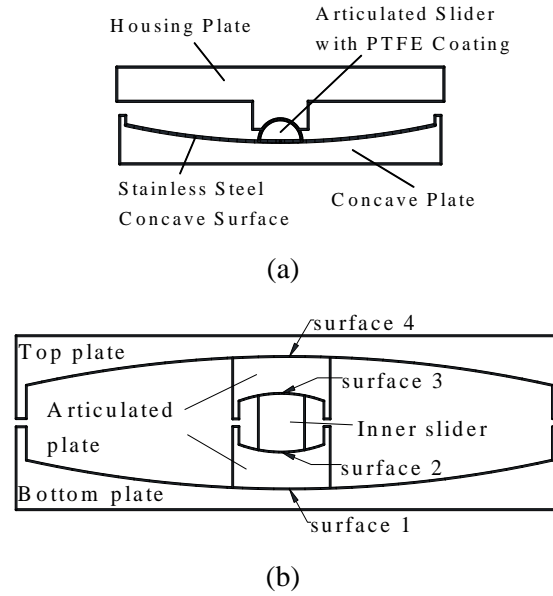


Figure 2-8 Different kinds of isolators (a) friction pendulum system; (b) TFP system

The TFP system is more sophisticated but also more efficient (multiple surfaces slide over one another to dissipate more energy) than a FPS, the sketch of which is shown in Figure 2-8 (b). It has an inner slider which slides along two concave surfaces (surface 2 and surface 3) of the articulated plates, and this makes up the inner pendulum; the two articulated plates slide along the two main concave surfaces (surface 1 and surface 4) of the top and the bottom plates comprising two more pendulums (EPS, 2019). Compared with the FPS, the TFP system is more adaptive because it exhibits different hysteretic properties at different levels of displacement. The TFP system also saves space because more sliding surfaces makes the total displacement distributed between multiple sliding surfaces (Moeindarbari & Taghikhany, 2012). Different stages of the TFP are realized by the slider or plates sliding along different combinations of surfaces. For instance, under low levels of excitation, only the low friction and short period inner pendulum is activated (the inner slider slides on surface 2 and 3) (EPS, 2019). For stronger levels of excitation, the pendulums that sliding over surface 1 and 4 are activated, resulting in longer period (larger horizontal displacement) and more energy dissipation. The effective radius and friction coefficient of all surfaces are specifically designed to achieve the optimal effect.

2.2.3 Rocker and pin bearings

A rocker bearing consists of a curved surface at the bottom to accommodate translational movement (Hamakareem Izat, 2017), and a pin at the top to accommodate rotational movement as illustrated in Figure 2-9 (a). The pin bearing only allows rotational movement through the steel pin, as illustrated in Figure 2-9 (b). Both rocker and pin bearings are applicable to steel bridges whose movement is adequately predicted, since they can only accommodate movement in one direction (Hamakareem Izat, 2017).

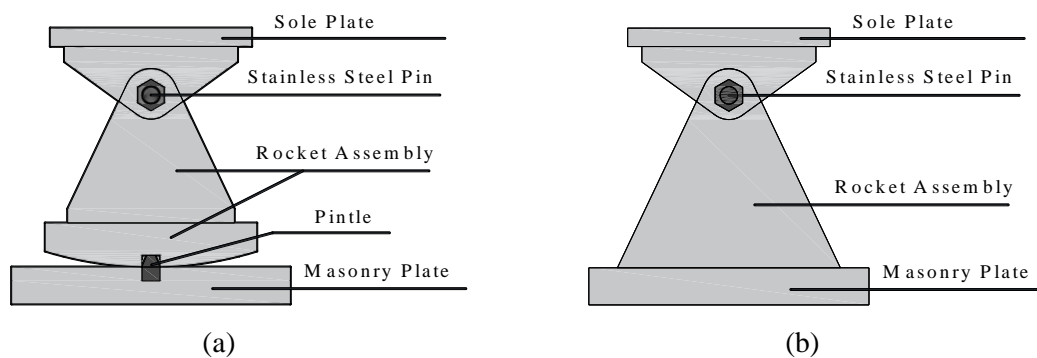


Figure 2-9 Sketch of (a) a rocker bearing; (b) a pin bearing.

2.2.4 Roller Bearing

There are two configurations of roller bearings. Single roller bearing consists of a roller placed between two plates, as shown in Figure 2-10 (a). It can accommodate both rotational and translational movement in longitudinal direction and it is easy and cheap to produce. But it has low vertical load capacity (Hamakareem Izat, 2017). The improved one is called multiple roller bearing, which consists of several rollers placed between two plates. It can make room for translational displacement and could accommodate rotational movement if combined with a pin bearing, as shown in Figure 2-10 (b). Multiple roller bearings are much more expensive and could support more vertical load. Since roller bearings are easy to corrode and damage, they need regular inspections and maintenance (Hamakareem Izat, 2017).

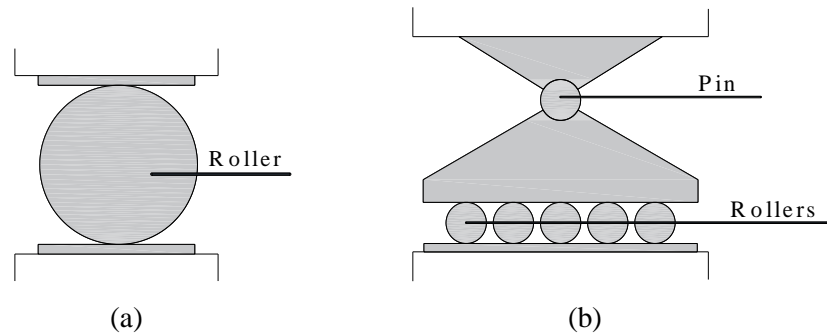


Figure 2-10 Sketch of (a) single roller bearing; (b) multiple roller bearing.

2.2.5 Pot Bearing

There are three types of pot bearings, namely fixed, guided and free pot bearings, as illustrated in Figure 2-11.

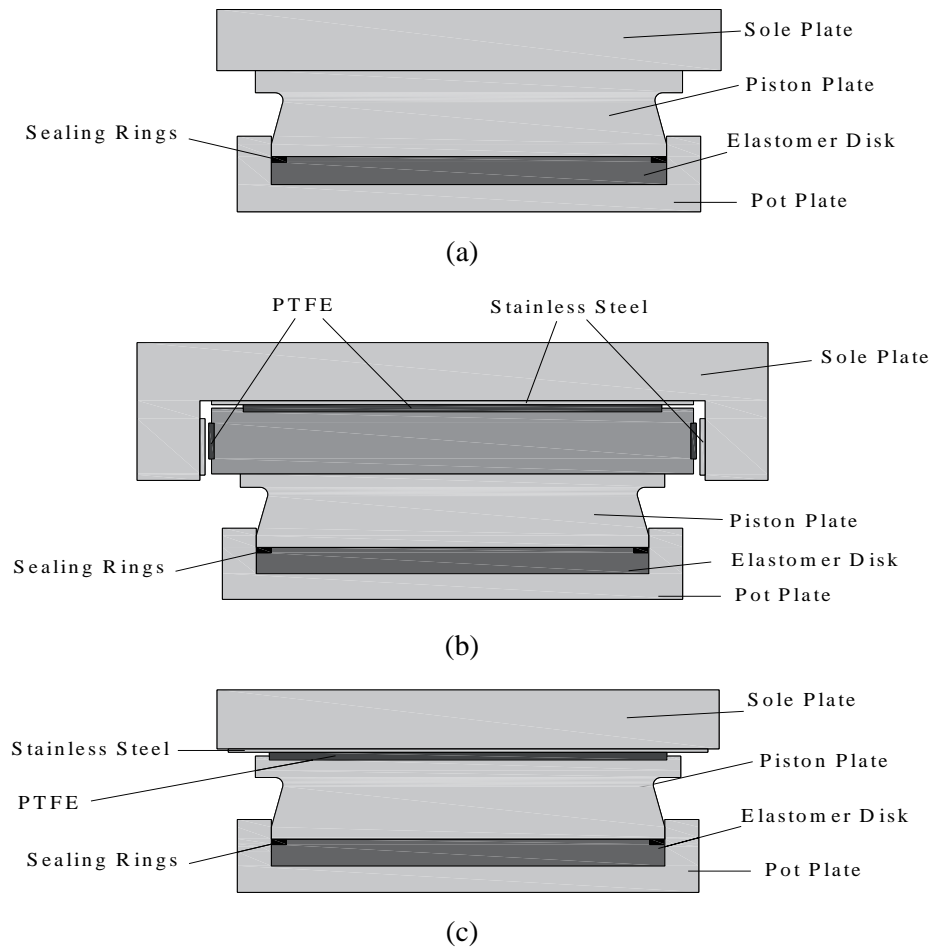


Figure 2-11 Sketch of (a) fixed pot bearing; (b) guided pot bearing; (c) free pot bearing.

They all consist of an elastomeric disk confined in a pot plate. The sealing rings are used to confine the elastomeric disk within the pot plate. The external load is transferred through piston plate to elastomeric disk. Due to the near incompressibility of elastomers, the elastomeric disk performs as an incompressible confined fluid which enables rotation along any axis. It can also support considerable vertical load; thus pot bearings are suitable for use when large bearing reactions are needed. Translational movement is limited in fixed pot bearings. Guided pot bearing with steel guides can accommodate translational movement in only one direction. Free pot bearings can accommodate translational movement in all directions (Hengshui Jingtong Rubber Co., n.d.).

2.2.6 Disc Bearing

Different types of disc bearings are shown in Figure 2-12. The polyurethane disc in the bearing can accommodate very high vertical loads, and at the same time allows rotational displacement in both longitudinal and transverse directions. The threaded shear pin with high shear strength transfers the horizontal loads between top and bottom bearing plate to protect the polyurethane disc. Similar to pot bearings, there are three common types of disc bearings (fixed, guided, and free) in terms of degrees of freedom in the horizontal direction. Compared to pot bearings, disc bearings have a relatively low profile, which make ideal for bridges and buildings with narrow room for bearings (Hengshui Jingtong Rubber Co., n.d.).

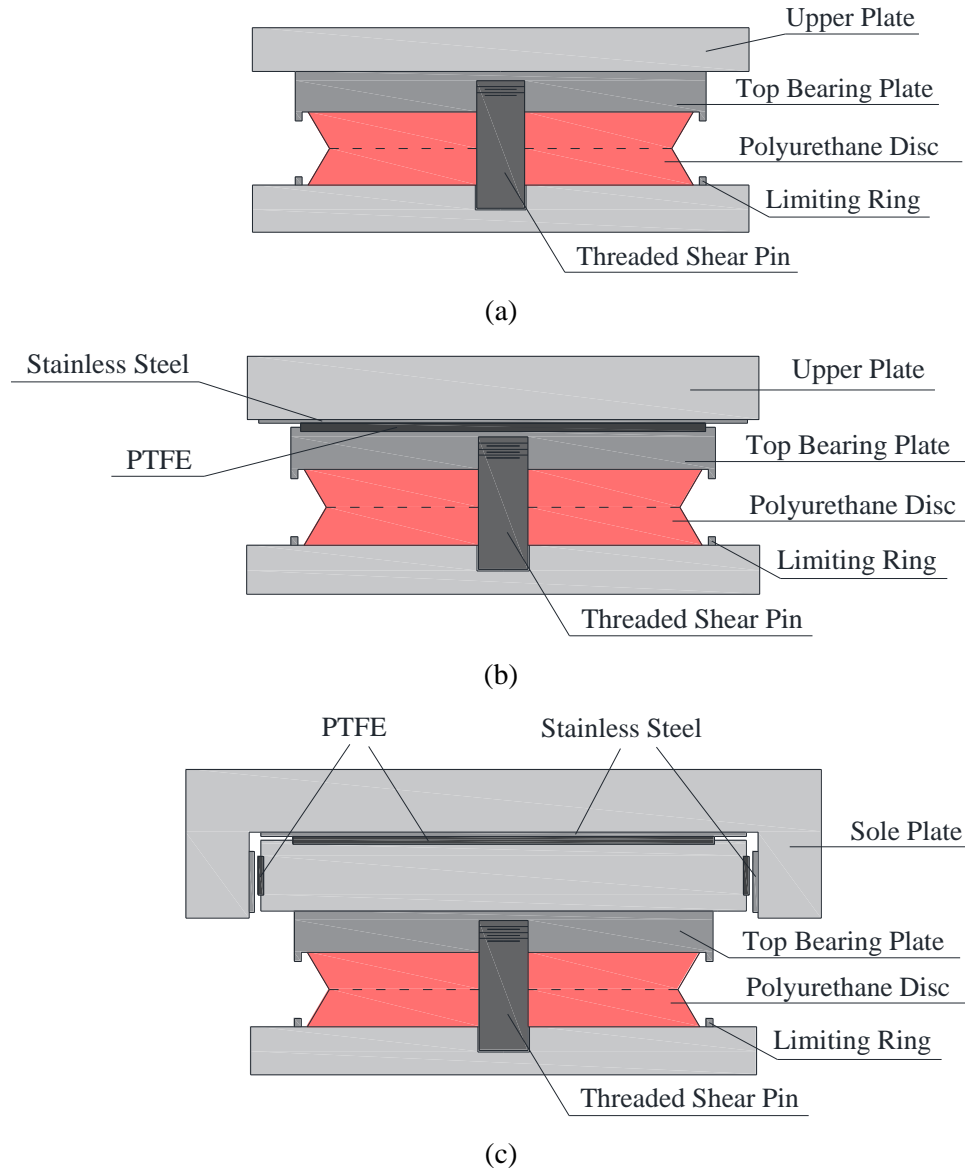


Figure 2-12 Sketch of (a) fixed disc bearing; (b) guided disc bearing; (c) free disc bearing.

2.3 Mechanics of Elastomeric Bearings

2.3.1 Mechanics of the reinforcement layers

According to AASHTO (2017), the top and the bottom layers of an elastomeric bearing are rubber layers with a thickness no more than 0.7 times the intermediate rubber layers. Stanton & Roeder (2008) illustrated the reason why the reinforcement layers provide vertical stiffness to the bearing. As shown in Figure 2-13 (a), an elastomeric pad is subjected to a vertical load. The top and bottom

surfaces of the pad are restrained against outward movement by the bonded condition for B-FREB and by friction for U-FREB, but the intermediate part of the pad is free to deform laterally (Stanton & Roeder, 2008). Rubber is a nearly incompressible material with a Poisson's ratio of approximately 0.5, therefore, when rubber is subjected to compression, it bulges to maintain the volume (Belivanis, 2017). In Figure 2-13 (a), V_1 is the volume calculated as the vertical deflection of the elastomer multiplied by the width of the pad based on a unit length, and V_2 is the volume of lateral bulging of elastomer on a single free edge of the pad based on a unit length. According to the incompressibility of elastomer, V_1 approximately equates to $2V_2$. The lateral bulging is related to the vertical deflection of the pad. By comparison, after inserting fiber-reinforced layers, the lateral expansion of rubber is significantly reduced. Again, because of the near incompressibility of the rubber, the volume of rubber remains the same, and small lateral bulging will lead to less vertical deflection (Stanton & Roeder, 2008). Therefore, the vertical (and rotational) stiffness of the bearing is increased by the addition of the reinforcement.

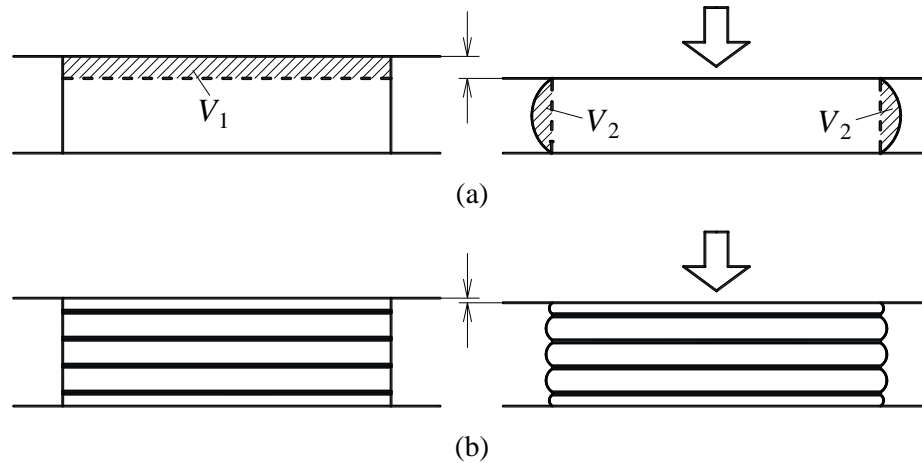


Figure 2-13 Configuration of bearings subjected to an axial compression load (a) with no reinforcement; (b) with reinforcement

2.3.2 Mechanical Model of FREBs

In this section, the compressive and the bending behaviour of the reinforced elastomeric bearings will be discussed. The analysis is based on one layer of an elastomeric pad with the shape of an

infinite strip. The procedures and equations for elastomeric pads of other shapes such as rectangular, circular and annular are similar to the infinite strip shape. The upper and lower surfaces are bonded to the fiber reinforcement layers. It was derived by Kelly & Takhirov (2002) using the assumptions of the pressure solution. The assumptions for the infinite strip pad are summarized below.

- Points on a vertical line in the elastomer before deformation lie on a parabola after loading.
- Under pure compression, horizontal planes remain plane and horizontal.
- Under pure bending, horizontal planes remain plane but tilted.
- The in-plane shear stresses, τ_{xy} and τ_{zy} , according to the coordinate system shown in Figure 2-14, are negligible.
- The stress state of the rubber is dominated by the internal pressure.
- The elastomer is linear elastic and compressible.
- Fiber is flexible and extensible.

The coordinate system for the infinite strip pad with thickness t and width $2b$ is shown in Figure 2-14. The strip is infinitely long in the y -direction, therefore, the problem is two dimensional, and the deformation is plain strain.

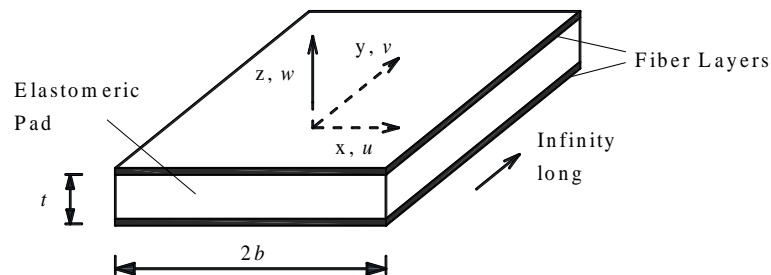


Figure 2-14 Coordinate system for an infinite strip pad with thickness t and width $2b$.

Before demonstrating the analysis procedure, the definition of the shape factor, S , is introduced. It is a geometric factor defined as the loaded area divided by the unloaded area of the pad. For the infinite strip, the shape factor is

$$S = b/t \quad (2.16)$$

2.3.2.1 Behaviour under pure compressive load

Figure 2-15 illustrates the displacements, u and w , in x - and z -direction of the pad under pure compression load. The total compressive deformation is Δ ($\Delta > 0$ in compression).

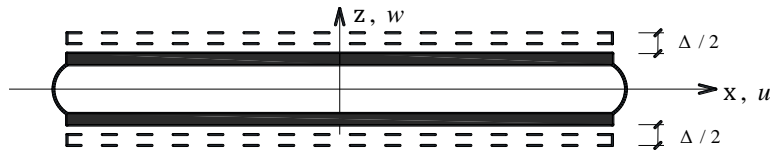


Figure 2-15 Displacement field of elastomeric pad under pure compression.

The displacements, u and w , are expressed respectively as

$$u(x, z) = u_0(x) \left(1 - \frac{4z^2}{t^2} \right) + u_1(x) \quad (2.17)$$

$$w(x, z) = w(z)$$

where u_0 represents the displacement of the points in the elastomer along the x -axis with respect to the origin (pad center), and u_1 represents the stretching of the reinforcement and is a constant through the thickness. The pattern of the displacement field is based on the assumptions of pressure solution. The first term of $u(x, z)$ corresponds to the parabola displacement profile of the point on the vertical line before deformation. The pattern of w indicates that the vertical displacement of the points on the same horizontal line are the same when under pure compression. Pinarbasi et al. (2006) found that the assumptions of the pressure solution are appropriate. The expression of $u_0(x)$, $u_1(x)$, and $w(z)$ could be determined by solving the differential equations. Due to the compressibility of the rubber, the two components of the strain,

$$\varepsilon_{xx} = \frac{\partial u}{\partial x}, \quad \varepsilon_{zz} = \frac{\partial w}{\partial z} \quad (2.18)$$

have the relationship that

$$\varepsilon_{xx} + \varepsilon_{zz} = -p/K \quad (2.19)$$

where p is the internal pressure and K represents the bulk modulus of the elastomer. After substituting the expression of ε_{xx} and ε_{zz} into Eq. (2.19), we have

$$\frac{\partial u_0}{\partial x} \left(1 - \frac{4z^2}{t^2} \right) + \frac{\partial u_1}{\partial x} + \frac{\partial w}{\partial z} = -\frac{p}{K} \quad (2.20)$$

Integrating Eq. (2.20) with respect to z over thickness, we have

$$\frac{2}{3} \frac{\partial u_0}{\partial x} + \frac{\partial u_1}{\partial x} + \frac{p}{K} = \frac{\Delta}{t} \quad (2.21)$$

Since w represents the displacement field in the vertical direction as shown in Figure 2-15, integrating the third term, $\partial w / \partial z$, of Eq. (2.20) with respect to z over the thickness would give the vertical deflection Δ . The equations of equilibrium for the stresses are

$$\begin{aligned} \frac{\partial \sigma_{xx}}{\partial x} + \frac{\partial \tau_{xy}}{\partial y} + \frac{\partial \tau_{xz}}{\partial z} &= 0 \\ \frac{\partial \tau_{xy}}{\partial x} + \frac{\partial \sigma_{yy}}{\partial y} + \frac{\partial \tau_{yz}}{\partial z} &= 0 \\ \frac{\partial \tau_{xz}}{\partial x} + \frac{\partial \tau_{yz}}{\partial y} + \frac{\partial \sigma_{zz}}{\partial z} &= 0 \end{aligned} \quad (2.22)$$

The stress state of the rubber is assumed to be dominated by p , which means the three components of the stress σ_{xx} , σ_{yy} and σ_{zz} are approximately equal to p , i.e.

$$\sigma_{xx} \approx \sigma_{yy} \approx \sigma_{zz} \approx -p \quad (2.23)$$

Because the elastomer is an isotropic material, Eq. (2.23) indicates that the Poisson's ratio of the elastomer is nearly 0.5, which in turn means the elastomer is nearly incompressible. After applying the assumptions mentioned before, and also replacing σ_{xx} , σ_{yy} and σ_{zz} by $-p$, Eq. (2.22) reduces to

$$\frac{\partial \tau_{xz}}{\partial z} = \frac{\partial p}{\partial x} \quad (2.24)$$

Assuming the materials are linear elastic, the shear stress τ_{xz} is related to the shear strain γ_{xz} by

$$\tau_{xz} = G\gamma_{xz} \quad (2.25)$$

with G is the shear modulus of the elastomer. A constant G is used in the derivation, which is commonly used and widely accepted as a simplification as part of the pressure solution (Al-Anany & Tait (2015) and Kelly & Konstantinidis (2011)). It would be exceptionally difficult to derive the solutions based on a nonlinear G since the stress state varies significantly throughout the elastomeric layer. Since $\gamma_{xz} = \partial u / \partial z + \partial w / \partial x$, after substituting Eq. (2.17) and Eq. (2.24) into Eq. (2.25), we have

$$\tau_{xz} = -\frac{8G}{t^2} zu_0 \quad (2.26)$$

and

$$\frac{\partial p}{\partial x} = -\frac{8Gu_0}{t^2} \quad (2.27)$$

As shown in Figure 2-16, the internal force per unit length of the fiber layer, $F(x)$, relates to the shear stresses on the upper and lower surfaces of the pad by

$$\frac{dF}{dx} - \tau_{xz} \Big|_{z=\frac{t}{2}} + \tau_{xz} \Big|_{z=-\frac{t}{2}} = 0 \quad (2.28)$$

After substituting the expression of τ_{xz} in Eq. (2.26) into this, we have

$$\frac{dF}{dx} = -\frac{8Gu_0}{t} \quad (2.29)$$

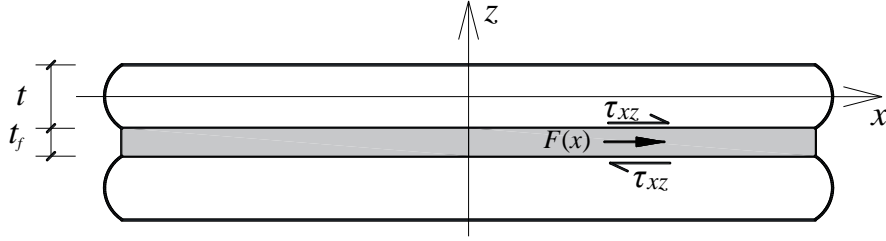


Figure 2-16 Force development in the reinforcement.

The extensional strain of the reinforcement, ε_f , relates to the internal force through the elastic modulus of the reinforcement, E_f , and the reinforcement thickness, t_f , such that

$$\varepsilon_f = \frac{\partial u_1}{\partial x} = \frac{F}{E_f t_f} \quad (2.30)$$

After combining this with Eq. (2.29), we have

$$\frac{\partial^2 u_1}{\partial x^2} = -\frac{8Gu_0}{E_f t_f t} \quad (2.31)$$

The complete system of equations for the combined effects of reinforcement extensibility and compressibility includes Eq. (2.27), Eq. (2.31) and Eq. (2.21), which are summarized below in Eq. (2.32).

$$\frac{\partial p}{\partial x} = -\frac{8Gu_0}{t^2} \quad (2.32)$$

$$\frac{\partial^2 u_1}{\partial x^2} = -\frac{8Gu_0}{E_f t_f t}$$

$$\frac{2}{3} \frac{\partial u_0}{\partial x} + \frac{\partial u_1}{\partial x} + \frac{p}{K} = \frac{\Delta}{t}$$

Differentiating the third expression of Eq. (2.32) with respect to x once, and substituting the first two expressions of Eq. (2.32) into it, we have

$$\frac{2}{3} \frac{\partial^2 u_0}{\partial x^2} - \frac{12GtS^2}{E_f t_f} \frac{2u_0}{3b^2} - \frac{12GS^2}{K} \frac{2u_0}{3b^2} = 0 \quad (2.33)$$

It is convenient to introduce two parameters, α and β , that represent respectively the extensibility of the reinforcement and the compressibility of the elastomer by

$$\alpha^2 = \frac{12Gt}{E_f t_f} S^2, \quad \beta^2 = \frac{12GS^2}{K} \quad (2.34)$$

It can be found that when E_f approaches infinity $\alpha = 0$ which means the reinforcement is rigid and inextensible. Also, when K approaches infinity $\beta = 0$ which means the elastomer is incompressible.

The variables u_0 and u_1 in Eq. (2.17) reflect the displacement field in the rubber. They are symmetric due to the symmetry of boundary and loading conditions. Therefore, u_0 and u_1 are odd functions of x . The two boundary conditions that solve the differential equations in Eq. (2.32) are that the pressure, p , and the stress in the reinforcement are zero at edges ($x = \pm b$). After solving Eq. (2.32) by using the symmetry and boundary conditions, the expression of u_0 , u_1 and p are determined as follows

$$u_0 = \frac{3}{2} \frac{\lambda b \sinh(\lambda x/b) \Delta}{\lambda^2 \cosh(\lambda) t} \quad (2.35)$$

$$u_1 = b \frac{\alpha^2}{\lambda^2} \left[\frac{x}{b} - \frac{\sinh(\lambda x/b)}{\lambda \cosh(\lambda)} \right] \frac{\Delta}{t} \quad (2.36)$$

$$p = \frac{K\beta^2}{\lambda^2} \left[1 - \frac{\cosh(\lambda x/b)}{\cosh(\lambda)} \right] \frac{\Delta}{t} \quad (2.37)$$

where λ is the compressibility and extensibility index, defined as

$$\lambda^2 = \alpha^2 + \beta^2 \quad (2.38)$$

The expression of $w(x)$ is obtained by substituting Eq. (2.35), Eq. (2.36), and Eq. (2.37) into Eq. (2.20), and then integrate both sides with respect to z , which when $\lambda = 0$, it is (Kelly & Konstantinidis, 2011)

$$w(z) = -\frac{3\Delta}{2t} \left(z - \frac{4z^3}{3t^2} \right) \quad (2.39)$$

Substituting Eq. (2.37) into Eq. (2.24) obtains the expression of the shear stress due to compression, τ_c , as

$$\tau_c = -\frac{\beta^2 K \varepsilon_c \sinh(\lambda x/b)}{\lambda b \cosh(\lambda)} z \quad (2.40)$$

where $\varepsilon_c = \Delta/t$ is the compressive strain of the pad. The maximum shear stress due to compression occurs at the edge where $z = t/2$ and $x = \pm b$, the amplitude is

$$\tau_{c,max} = \frac{6GS\varepsilon_c}{\lambda} \tanh(\lambda) \quad (2.41)$$

The amplitude of the maximum shear strain is

$$\gamma_{c,max} = \frac{6S\varepsilon_c}{\lambda} \tanh(\lambda) \quad (2.42)$$

The load per unit length of the infinite strip, P , is given by

$$P = \int_{-b}^b p(x)dx = \frac{2Kb\Delta\beta^2}{\lambda^2 t} \left[1 - \frac{\tanh(\lambda)}{\lambda} \right] \quad (2.43)$$

The loaded area of the pad per unit length is $A = 2b$. Considering the pad is the j^{th} layer of an infinite strip bearing, and the compression modulus of the layer, E_{cj} , is given by

$$E_{cj} = \frac{Pt_j}{\Delta_j A} = \frac{12GS_j^2}{\lambda_j^2} \left[1 - \frac{\tanh(\lambda_j)}{\lambda_j} \right] \quad (2.44)$$

The vertical stiffness of the infinite strip pad, K_{vj} , is then given by

$$K_{vj} = \frac{E_{cj}A}{t_j} \quad (2.45)$$

The n -layer bearing could be considered as n springs, with the vertical stiffness K_{vj} , connected in series. The load acting on the bearing will transfer to each elastomeric layer and results in deformation for each. The vertical stiffness for a bearing is then given by

$$K_v = \frac{1}{\sum_{j=1}^n \frac{1}{K_{vj}}} \quad (2.46)$$

Note that since the reinforcement layers are much stiffer than the elastomeric layers, they are not included in Eq. (2.46). The compression modulus of the bearing is

$$E_c = \frac{K_v t_r}{A} \quad (2.47)$$

where $t_r = \sum_{j=1}^n t_j$ is the thickness of all the elastomeric layers. Kelly & Konstantinidis (2011) studied the effect of K/G and S on the compressive modulus for infinite strip elastomeric pads. For

bearings with S larger than 5, the results of E_c show a large decrease with smaller K/G value (smaller K/G indicates the elastomer is more compressible if G is kept as a constant); and for bearings with S smaller than 5, the difference between E_c with different K/G value is small. Therefore, the compressibility of elastomer could be neglected only for bearings with S smaller than 5, depending on the pad geometry.

2.3.2.2 Behaviour under pure bending

Under pure bending, the elastomeric pad deforms as shown in Figure 2-17, and the displacement field is given by (Kelly & Takhirov, 2002)

$$u(x, z) = u_0(x) \left(1 - \frac{4z^2}{t^2} \right) + u_1(x) - \theta \frac{z^2}{2t} \quad (2.48)$$

$$w(x, z) = \frac{\theta z x}{t}$$

where θ is the relative rotation between the upper and the lower surfaces of the pad.

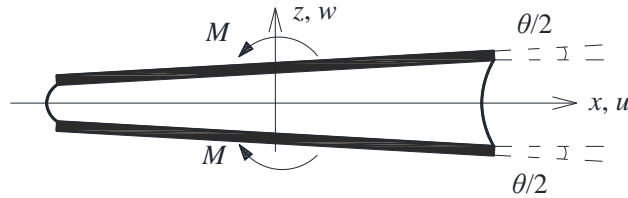


Figure 2-17 Elastomeric pad under pure bending.

Substitute Eq. (2.48) into Eq. (2.18) and Eq. (2.19), and integrating with respect to z over the thickness, gives

$$\frac{2}{3} \frac{\partial u_0}{\partial x} + \frac{\partial u_1}{\partial x} + \frac{p}{K} = -\frac{\theta x}{t} \quad (2.49)$$

The complete system of equations for the combined effects of reinforcement extensibility and compressibility includes Eq. (2.27), Eq. (2.49), Eq. (2.31) and Eq. (2.30). They are summarized in Eq. (2.50) with the boundary conditions.

$$\begin{aligned}
\frac{\partial p}{\partial x} &= -\frac{8Gu_0}{t^2}, \quad p(\pm b) = 0 \\
\frac{2}{3} \frac{\partial u_0}{\partial x} + \frac{\partial u_1}{\partial x} + \frac{p}{K} &= -\frac{\theta x}{t} \\
\frac{\partial^2 u_1}{\partial x^2} &= -\frac{8Gu_0}{E_f t_f t}
\end{aligned} \tag{2.50}$$

$$F(x) = E_f t_f \frac{\partial u_1}{\partial x}, \quad F(\pm b) = 0$$

Solving the above differential equations and using the symmetric conditions obtains the expression of p

$$p = \frac{K\beta^2 b\theta}{\lambda^2 t \sinh(\lambda)} \sinh\left(\frac{\lambda}{b}x\right) - \frac{K\beta^2 \theta}{\lambda^2 t} x \tag{2.51}$$

Substituting Eq. (2.51) into Eq. (2.24) obtains the expression of τ_{xz} , or the shear stress due to rotation, τ_r , as

$$\tau_r = \frac{K_e \theta}{t} \left[\frac{\lambda}{\sinh \lambda} \cosh\left(\frac{\lambda}{b}x\right) - 1 \right] z \tag{2.52}$$

where K_e accounts for the compressibility of the elastomer and the extensibility of the fiber reinforcement and is expressed by

$$\frac{1}{K_e} = \frac{1}{K} + \frac{t}{E_f t_f} \tag{2.53}$$

Note, K_e has the relationship with λ such that

$$\lambda^2 = \frac{12GS^2}{K_e} \tag{2.54}$$

The amplitude of the maximum shear strain due to rotation is

$$\gamma_{r,max} = \frac{6S^2\theta}{\lambda^2} [\lambda \coth(\lambda) - 1] \quad (2.55)$$

The moment applied to the pad is given by

$$M = - \int_{-b}^{+b} p(x)x dx = \frac{2K\beta^2\theta}{3\lambda^2t} b^3 + \frac{2K\beta^2b^3\theta}{\lambda^4t} - \frac{2K\beta^2b^3\theta}{\lambda^3t} \coth(\lambda) \quad (2.56)$$

Considering the pad is the j^{th} layer of an infinite strip bearing, and effective bending stiffness of the layer is

$$E_{b_j}I = \frac{M}{\theta_j/t_j} = \frac{24b^3GS_j^2}{\lambda_j^4} \left[\frac{\lambda_j^2}{3} + 1 - \lambda_j \coth(\lambda_j) \right] \quad (2.57)$$

where I is the second moment of area of the pad based on a unit length, therefore

$$I = \frac{(2b)^3}{3} \quad (2.58)$$

The bending modulus of the j th layer is

$$E_{b_j} = \frac{36GS_j^2}{\lambda_j^4} \left[\frac{\lambda_j^2}{3} + 1 - \lambda_j \coth(\lambda_j) \right] \quad (2.59)$$

The bending stiffness of the strip pad is then given by

$$K_{b_j} = \frac{E_{b_j}I}{t_j} \quad (2.60)$$

Similar to the compression case, the bending stiffness for a bearing with n layers of elastomer is

$$K_b = \frac{1}{\sum_{j=1}^n \frac{1}{K_{b_j}}} \quad (2.61)$$

The bending modulus of the bearing is

$$E_b = \frac{K_b t_r}{I} \quad (2.62)$$

2.3.2.3 Lift-off behaviour under the combination of compression and rotation

The pressure distribution along the width generated by the compressive load or bending moment is given by Eq. (2.37) and Eq. (2.51), respectively. After introducing K_e , they are rewritten as

$$p_c(x) = K_e \left(1 - \frac{\cosh(\lambda x/b)}{\cosh \lambda} \right) \varepsilon_c \quad (2.63)$$

$$p_r(x) = -K_e \left(\frac{x}{b} - \frac{\sinh(\lambda x/b)}{\sinh \lambda} \right) \frac{\theta b}{t} \quad (2.64)$$

where the subscript c and r represent compression and rotation, respectively.

Van Engelen (2019) derived the relationship between the applied moment and the rotation of the pad upper surface corresponding to an infinite strip geometry, amongst other geometries. The derivation for an infinite strip pad is briefly introduced here.

When lift-off occurs, the hydrostatic pressure caused by compression and rotation at a certain location, x , is zero, which means

$$p_c(x) + p_r(x) = 0 \quad (2.65)$$

Also, the tangent of the hydrostatic pressure is zero (i.e. a local minimum), which means

$$\frac{dp_c(x)}{dx} + \frac{dp_r(x)}{dx} = 0 \quad (2.66)$$

The above two conditions, i.e. Eq. (2.65) and Eq. (2.66), are based on the principle of superposition and a linear elastic material. If the value of ε_c is given, then, the two unknowns are x and θ_0 , where θ_0 is the lift-off initiation rotation. Taking the partial derivatives of Eq. (2.63) and Eq. (2.64) with respect to x and substituting the results into Eq. (2.66) gives

$$\varepsilon_c = -\frac{\cosh\lambda}{\lambda \sinh(\lambda x/b)} \left[1 - \lambda \frac{\cosh(\lambda x/b)}{\sinh\lambda} \right] \frac{\theta_0 b}{t} \quad (2.67)$$

Eliminate ε_c by combining Eq. (2.67) with Eq. (2.65), which gives an equation in terms of x :

$$\frac{x}{b} - \frac{\cosh\left(\frac{\lambda x}{b}\right) \cosh\lambda}{\sinh\left(\frac{\lambda x}{b}\right) \sinh\lambda} + \frac{1}{\sinh\left(\frac{\lambda x}{b}\right) \sinh\lambda} - \frac{\cosh\left(\frac{\lambda x}{b}\right)}{\lambda \sinh\left(\frac{\lambda x}{b}\right)} + \frac{\cosh\lambda}{\lambda \sinh\left(\frac{\lambda x}{b}\right)} = 0 \quad (2.68)$$

Eq. (2.68) is only satisfied on condition that $x = \pm b$, which means lift-off occurs at the edges of the pad, which is intuitively expected. Consider a positive rotation and the solution is $x = b$, after substituting into Eq. (2.67), it becomes:

$$\frac{\varepsilon_c t}{\theta_0 b} = \coth\lambda \left(\coth\lambda - \frac{1}{\lambda} \right) \quad (2.69)$$

Eq. (2.69) gives the expression of θ_0 as a function of λ and ε_c for a given size of infinite strip pad (t and b , i.e., the shape factor is known). After lift-off occurs, the remaining part of the pad (which maintains contact) keeps reducing in size with increasing rotation. During this process, the initiation of lift-off is continuously occurring for the instantaneous reduced pad, and the relationship given by Eq. (2.69) is always satisfied. For a given P , and θ (larger than θ_0), Eq. (2.69) becomes:

$$\frac{\varepsilon_{ci}t}{\theta b_i} = \coth\lambda_i \left(\coth\lambda_i - \frac{1}{\lambda_i} \right) \quad (2.70)$$

where the subscript i means that the variable is an instantaneous value and is a function of θ (Van Engelen, 2019). The instantaneous compression modulus is based on Eq. (2.44) expressed as

$$E_{ci} = K_e \left(1 - \frac{1}{\lambda_i} \tanh\lambda_i \right) \quad (2.71)$$

E_{ci} corresponds to the applied vertical load, P , by

$$\frac{P}{2b_i} = E_{ci}\varepsilon_{ci} \quad (2.72)$$

Substituting Eq. (2.71) into Eq. (2.72) and further into Eq. (2.70) gives:

$$\frac{Pt}{2\theta K_e} = b_i^2 \left(\coth\lambda_i - \frac{1}{\lambda_i} \right)^2 \quad (2.73)$$

The instantaneous variables can be related to those variables before lift-off occurs by a parameter η , which is also a function of θ :

$$S_i = \eta S ; \quad \lambda_i = \eta \lambda ; \quad b_i = \eta b \quad (2.74)$$

Introducing the average compressive stress, σ_c , based on the unit-length area of the pad

$$\sigma_c = \frac{P}{2b} \quad (2.75)$$

Substitute Eq. (2.75) into Eq. (2.73) gives:

$$\frac{\sigma_c}{\theta S K_e} = \eta^2 \left(\coth\eta\lambda - \frac{1}{\eta\lambda} \right)^2 \quad (2.76)$$

According to Eq. (2.59), the instantaneous bending modulus is

$$E_{bi} = \frac{36GS^2}{\eta^2\lambda^4} \left(\frac{\eta^2\lambda^2}{3} + 1 - \eta\lambda\coth(\eta\lambda) \right) \quad (2.77)$$

The relationship between E_{bi} and θ could be derived by combining Eq. (2.76) and Eq. (2.77) together. Although it is hard to eliminate η because both of the equations are implicit functions of η , the $E_{bi} - \theta$ relationship could be found using MATLAB (2018) by vector operation. After the $E_{bi} - \theta$ relationship is established, integrating $E_{bi}I_i/t$ with respect to θ gives the relationship between the applied moment, M , and the rotation, θ . The moment-rotation relationship for a bearing with n layers could be derived only if all the elastomeric layers have the same thickness. It could be realized by multiplying the θ vector with n , while keeping the M vector the same.

2.4 Code Provisions for Elastomeric Bearings

2.4.1 CSA S6 – Canadian Highway Bridge Design Code

In CSA S6-14 (2014), uplift for bonded bearings is prevented by constraining the magnitude of the applied rotation; there is no such provision about lift-off. In CSA S6-19 (2019) C1. 11.6.6.8, a new statement is added:

“Laminated bearings not bonded to the adjacent components of the bridge shall not be subject to lift-off under any permanent loading conditions.”

This new statement constrains lift-off behavior. The following limitation described in the code is based on Stanton & Roeder's (2008) research. Lift-off is prevented by letting $\alpha_c > 1/3$ in the following equation

$$\alpha_c = \frac{\varepsilon_\alpha}{S} \frac{n}{\theta_s} \quad (2.78)$$

where n is the number of layers, θ_S is the total rotation applied to the bearing, and

$$\varepsilon_\alpha = \frac{f_s}{3BGS^2} \quad (2.79)$$

is the compressive strain, where B accounts for the geometry. The value of f_s shall be taken as the compressive stress due to dead and live load at SLS (Serviceability Limit State) with the live load multiplied by a factor of 1.75. B shall be taken as 1.6 when evaluating both rectangular and circular bearings. For rectangular bearings, B may instead be calculated as

$$B = (2.31 - 1.86\lambda_c) + (-0.90 + 0.96\lambda_c) \left[1 - \min\left(\frac{L_e}{W_e}, \frac{W_e}{L_e}\right) \right]^2 \quad (2.80)$$

where L_e and W_e are the length and the width of the bearing, respectively. For circular bearings, B can also be calculated as

$$B = \frac{2}{1 + 2\lambda_c^2} \quad (2.81)$$

where

$$\lambda_c = S \sqrt{\frac{3G}{K}} \quad (2.82)$$

is the compressibility index.

2.4.2 AASHTO (2017)

In AASHTO (2017) C14.7.5.3.3 a statement that “‘no-lift-off’ provisions have been removed’ is made based on the research by Stanton & Roeder (2008). In the previous version of the code (before the 5th edition AASHTO (2010)), both uplift and lift-off were prohibited, which made it challenging

for the designer, because the thickness of the bearing should be large to meet such requirements but then would cause stability problems (according to the research by Stanton & Roeder (2008)).

Consider an infinite strip pad of width $2b$, as shown in Figure 2-18. A rigid plate rests on it that is rotated an angle θ and subjected to a load P . The compressive load is small enough that lift-off occurs. The following assumptions are made:

- The pad could be divided into two parts: the loaded part and the unloaded part, the dividing line between the two parts is where contact is lost.
- The unloaded part experiences no vertical load and negligible internal stress and strain.
- The vertical edge of the loaded part behaves as a free surface.
- The upper plate is rigid.
- The elastomer is incompressible.

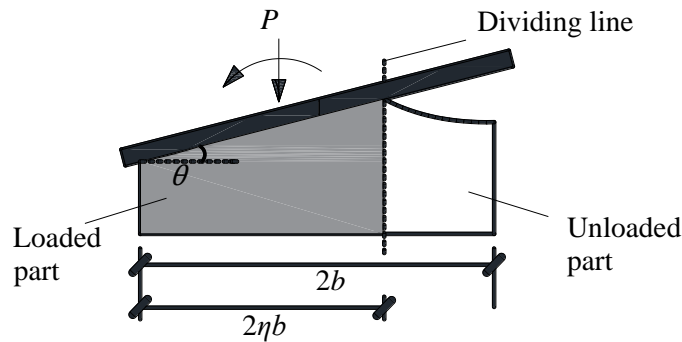


Figure 2-18 Lift-off: Assumed bearing behaviour (Stanton & Roeder, 2008).

For a given value of P , there exists a rotation at which the vertical displacement on the tension edge of the pad is zero. Such a rotation is represented by θ_c , which could also be interpreted as the rotation when the axial strain on the tension edge caused by both p and θ are cancelled out. This is defined as the characteristic rotation. Notice that θ_c is different from the lift-off initiation rotation. Stanton & Roeder (2008) found that lift-off started at a rotation of $\theta = 3\theta_c$. They also derived the analytical solution of the total shear strain on the compressive edge of the elastomeric pad as a

function of rotation, which is linear before lift-off occurs and nonlinear after the initiation of lift-off. The piecewise function is continuous at $\theta = 3\theta_c$. The relationship shows that after lift-off occurs, the increasing rate of total shear strain at the compression edge is slightly reduced (the nonlinear curve slightly flattens out). Thus, even if the linear relationship is used after lift-off, the error would be small and the results would be conservative. Stanton & Roeder (2008) also gave the physical explanation of why lift-off could reduce the total shear strain at the compression edge. Consider an elastomeric pad that lift-off has occurred. Firstly fix the position of rigid plate and pull the separated elastomer upwards to make it attach to the rigid plate again. The elastomer in the lift-off region will experience tensile stress. Then, release the vertical displacement of the rigid plate but still keep the same rotation. The plate will move downwards due to the tensile stress. This increases the bulge on the compression side and the shear strain will be larger when the elastomer is bonded to the plate. This conclusion was also verified by a numerical simulation performed by Stanton & Roeder (2008).

They also did experiments to study the effect of rotation on debonding (which is one of the failure modes of elastomeric bearings). Results showed that even with large axial loads combined with monotonic rotation, debonding did not occur until the rotation reached at least 0.05 radians (Stanton & Roeder, 2008)

2.4.3 Limitations

The above studies strongly indicate that permitting lift-off for bridge SREBs is reasonable. But it has its own limitations. It only considers the bearing geometry of an infinite strip and it assumes the elastomer is incompressible and the reinforcement is inextensible, which are only applicable to SREBs. As FREB may be easier to manufacture than SREB, it is of great significance to develop the design guidelines for FREB. Therefore, the extensibility of fiber reinforcement and the compressibility of elastomer should be considered when studying the lift-off behaviour.

This leads to the first two objectives of my research in Section 1.3, which are to validate the existing analytical solution of lift-off initiation rotation and moment-rotation relationship based on extensible reinforcement and a compressible elastomer, and to further derive the analytical solution of shear and normal stress distribution and validate them. Also, since Canadian and American bridge design codes have different provisions regarding lift-off of bearing, more studies are needed to figure out whether lift-off could be allowed to occur or not.

Chapter 3 Stress Distribution after Lift-off Occurs

Based on the research done by Van Engelen (2019) and Kelly & Takhirov (2002), the shear strain and normal stress distribution of the unbonded bearing along the horizontal path after lift-off can be derived. The details of the derivation is discussed below.

3.1 Shear Stress and Shear Strain Distribution

Before lift-off, the shear stress distribution caused by compression along the top surface of an elastomeric pad could be derived by substituting $z = t/2$ into Eq. (2.40), which, after simplification, gives

$$\tau_c = -6GS \frac{\sinh(\lambda x/b)}{\lambda \cosh(\lambda)} \varepsilon_c \quad (3.1)$$

After substituting the expression of ε_c

$$\varepsilon_c = \frac{\sigma_c}{E_c} = \frac{P/2b}{K_e \left[1 - \frac{\tanh(\lambda)}{\lambda} \right]} \quad (3.2)$$

Eq. (3.1) becomes

$$\tau_c = -3GS \frac{\sinh(\lambda x/b)}{K_e [\lambda \cosh(\lambda) - \sinh(\lambda)]} \frac{P}{b} \quad (3.3)$$

The shear stress caused by rotation at the top surface could be further derived from Eq. (2.52) by the same method as for the compression case, which, after simplification, is

$$\tau_r = \left[\frac{\lambda}{\sinh \lambda} \cosh \left(\frac{\lambda}{b} x \right) - 1 \right] \frac{K_e \theta}{2} \quad (3.4)$$

Substituting S , λ and b with ηS , $\eta \lambda$ and ηb into Eq. (3.3) and Eq. (3.4), respectively, the shear strain distribution after lift-off for an elastomeric pad under compression or rotation could be derived as

$$\tau_{ci} = -3GS \frac{\sinh(\lambda x/b)}{K_e[\eta\lambda \cosh(\eta\lambda) - \sinh(\eta\lambda)]} \frac{P}{b} \quad (3.5)$$

and

$$\tau_{ri} = \left[\frac{\eta\lambda}{\sinh(\eta\lambda)} \cosh\left(\frac{\lambda}{b}x\right) - 1 \right] \frac{K_e\theta}{2} \quad (3.6)$$

Note that the limit of x in Eq. (3.5) and Eq. (3.6) is $-\eta b \leq x \leq \eta b$. Based on the principle of superposition, the complete expression of the shear stress distribution caused by the combination of compression and rotation along the top surface of an elastomeric pad is then given by

$$\tau = \begin{cases} -3GS \frac{\sinh\left(\frac{\lambda x}{b}\right)}{K_e[\lambda \cosh(\lambda) - \sinh(\lambda)]} \frac{P}{b} + \left[\frac{\lambda}{\sinh(\lambda)} \cosh\left(\frac{\lambda}{b}x\right) - 1 \right] \frac{K_e\theta}{2} & (\theta < \theta_0) (-b \leq x \leq b) \\ -3GS \frac{\sinh\left(\frac{\lambda x}{b}\right)}{K_e[\eta\lambda \cosh(\eta\lambda) - \sinh(\eta\lambda)]} \frac{P}{b} + \left[\frac{\eta\lambda}{\sinh(\eta\lambda)} \cosh\left(\frac{\lambda}{b}x\right) - 1 \right] \frac{K_e\theta}{2} & (\theta \geq \theta_0) (-\eta b \leq x \leq \eta b) \end{cases} \quad (3.7)$$

where η is related to θ by Eq. (2.76). The maximum shear stress appears at the compressive edge of the pad, therefore, by substituting $x = -b$ for $\theta < \theta_0$ and $x = -\eta b$ for $\theta \geq \theta_0$ into Eq. (3.9), we can get the maximum value of τ as

$$\tau_{max} = \begin{cases} 6GS \frac{\tanh(\lambda)}{\lambda K_e \left[1 - \frac{\tanh(\lambda)}{\lambda} \right]} \frac{P}{2b} + \left[\frac{\lambda}{\tanh(\lambda)} - 1 \right] \frac{K_e\theta}{2} & (\theta < \theta_0) \\ 6GS \frac{\tanh(\eta\lambda)}{\lambda K_e \left[1 - \frac{\tanh(\eta\lambda)}{\eta\lambda} \right]} \frac{P}{2b} + \left[\frac{\eta\lambda}{\tanh(\eta\lambda)} - 1 \right] \frac{K_e\theta}{2} & (\theta \geq \theta_0) \end{cases} \quad (3.8)$$

The complete expression of the shear strain distribution as well as the maximum shear strain are then further derived by dividing Eq (3.7) and Eq. (3.8) by G , which gives

$$\gamma = \begin{cases} -3S \frac{\sinh\left(\frac{\lambda x}{b}\right)}{K_e[\lambda \cosh(\lambda) - \sinh(\lambda)]} \frac{P}{b} + \left[\frac{\lambda}{\sinh(\lambda)} \cosh\left(\frac{\lambda}{b}x\right) - 1 \right] \frac{K_e \theta}{2G} & (\theta < \theta_0) (-b \leq x \leq b) \\ -3S \frac{\sinh\left(\frac{\lambda x}{b}\right)}{K_e[\eta \lambda \cosh(\eta \lambda) - \sinh(\eta \lambda)]} \frac{P}{b} + \left[\frac{\eta \lambda}{\sinh(\eta \lambda)} \cosh\left(\frac{\lambda}{b}x\right) - 1 \right] \frac{K_e \theta}{2G} & (\theta \geq \theta_0) (-\eta b \leq x \leq \eta b) \end{cases} \quad (3.9)$$

$$\gamma_{max} = \begin{cases} 6S \frac{\tanh(\lambda)}{\lambda K_e \left[1 - \frac{\tanh(\lambda)}{\lambda}\right]} \frac{P}{2b} + \left[\frac{\lambda}{\tanh(\lambda)} - 1 \right] \frac{K_e \theta}{2G} & (\theta < \theta_0) \\ 6S \frac{\tanh(\eta \lambda)}{\lambda K_e \left[1 - \frac{\tanh(\eta \lambda)}{\eta \lambda}\right]} \frac{P}{2b} + \left[\frac{\eta \lambda}{\tanh(\eta \lambda)} - 1 \right] \frac{K_e \theta}{2G} & (\theta \geq \theta_0) \end{cases} \quad (3.10)$$

3.2 Normal Stress Distribution

Before lift-off, the internal pressure (normal stress) distribution caused by compression and rotation along the horizontal path of an elastomeric pad are given by Eq. (2.37) and Eq. (2.51), they are simplified and rewritten here for convenience.

$$p_c = \frac{\lambda [\cosh(\lambda) - \cosh(\lambda x/b)]}{\cosh(\lambda) [\lambda - \tanh(\lambda)]} \frac{P}{2b} \quad (3.11)$$

and

$$p_r = K_e \left[\frac{\sinh(\lambda x/b) S}{\sinh(\lambda)} - \frac{x}{t} \right] \theta \quad (3.12)$$

After substituting S , λ and b with ηS , $\eta \lambda$ and ηb , they become

$$p_{ci} = \frac{\eta \lambda [\cosh(\eta \lambda) - \cosh(\lambda x/b)]}{\cosh(\eta \lambda) [\eta \lambda - \tanh(\eta \lambda)]} \frac{P}{2b} \quad (3.13)$$

and

$$p_{ri} = K_e \left[\frac{\sinh(\lambda x/b) \eta S}{\sinh(\eta \lambda)} - \frac{x}{t} \right] \theta \quad (3.14)$$

Therefore, under the combination of compression and rotation, the expression of normal stress distribution along the horizontal path of the top surface is

$$p = \begin{cases} \frac{\lambda \left[\cosh(\lambda) - \cosh\left(\frac{\lambda x}{b}\right) \right]}{\cosh(\lambda) [\lambda - \tanh(\lambda)]} \frac{P}{2b} + K_e \left[\frac{\sinh\left(\frac{\lambda x}{b}\right) S}{\sinh(\lambda)} - \frac{x}{t} \right] \theta & (\theta < \theta_0) (-b \leq x \leq b) \\ \frac{\eta \lambda \left[\cosh(\eta \lambda) - \cosh\left(\frac{\lambda x}{b}\right) \right]}{\cosh(\eta \lambda) [\eta \lambda - \tanh(\eta \lambda)]} \frac{P}{2b} + K_e \left[\frac{\sinh\left(\frac{\lambda x}{b}\right) \eta S}{\sinh(\eta \lambda)} - \frac{x}{t} \right] \theta & (\theta \geq \theta_0) (-\eta b \leq x \leq \eta b) \end{cases} \quad (3.15)$$

Chapter 4 Numerical Simulation

4.1 Introduction

The purposes of performing the numerical simulations are to

- validate the analytical solution of the lift-off initiation rotation and the moment-rotation relationship for an unbonded pad derived by Van Engelen (2019);
- validate the expression of shear strain and normal stress distribution for an unbonded pad after lift-off derived and given by Eq. (3.9) and Eq. (3.15);
- conduct parametric studies by considering the number of layers, shape factor, and the compressibility and extensibility index, λ , and study their effect on the lift-off behaviour.

The details of the scenarios will be discussed in Section 4.2. The model validation was conducted by comparing the numerical and the analytical solutions of the compression modulus and bending modulus given respectively by Eq. (2.44) and Eq. (2.59), and also comparing the numerical and analytical stress distribution given by Eq. (2.40), Eq. (2.52), Eq. (2.63) and Eq. (2.64). Bearings with different number of layers were simulated during the validation. The finite element analysis was conducted by using the commercial software ABAQUS (2016). As it is a static problem, the Static/General procedure was selected. A two-dimensional simulation was conducted based on the plane strain assumption for the infinite strip bearing. Since large deformation and strain would develop in elastomer, the simulations were based on large deformation.

4.2 Scenario Description

4.2.1 Model validation

In order to validate the FEA model of the bearing, five bonded bearings with different number of layers (3, 5, 7, 9 and 11 layers) were modelled. They are named as Bearing B1 to Bearing B5 by

sequence. Either 5 MPa compression or 0.01-radian rotation was applied to these bearings. The shape factor of the top and bottom elastomeric layer (according to Eq. (2.16)) is 31.25, and for the intermediate layer is 15.63, respectively. The second shape factor S_2 is defined as the bearing width divided by the total thickness of the intermediate elastomeric layers. The S_2 value for Bearing B1 to Bearing B5 are shown in Table 4-1. Take Bearing B3 as an example, there are 7 elastomeric layers in total, and there are 5 intermediate elastomeric layers. The total thickness of the 5 intermediate layers is $5 \times 12 \text{ mm} = 60 \text{ mm}$. The bearing width is $2b = 375 \text{ mm}$. Therefore, $S_2 = 375/60 = 6.25$.

Table 4-1 Second shape factor of bonded bearings.

Bearing	B1	B2	B3	B4	B5
Number of Elastomeric Layers	3	5	7	9	11
S_2	31.25	10.41	6.25	4.46	3.47

The effective elastic modulus of the fiber is 30 GPa and Poisson's ratio is 0.2. The initial shear modulus and the bulk modulus of the elastomer are 0.8 MPa and 2000 MPa, respectively. The initial shear modulus is the tangential shear modulus when the shear strain in the elastomer is zero. The material properties were selected to be the same as those used in the FEA model by Al-Anany & Tait (2015) for model validation.

4.2.2 Validation and Investigation of lift-off behaviour

In order to validate the analytical moment-rotation relationship of U-FREB derived by Van Engelen (2019) as well as the normal and shear stress distribution under the combination of compression and rotation, three groups of bearings were modelled. For each group, one of the parameters was considered (i.e. number of layers, S , and λ).

4.2.2.1 Number of Layers

Eight U-FREBs with a different number of elastomeric layers (3, 5, 7, 9, 11, 13, 15, and 17 layers) were modelled. They are named as Bearing U1 to Bearing U8 by sequence. The material properties are the same as Bearings B1 to B5. The width of each bearing is 375 mm, the thickness of the reinforcement layers is 1 mm, and the thickness of the top and the bottom elastomeric layers are the same as the intermediate layers, which is 12 mm. The same thickness makes it possible to do the comparison between the analytical and numerical solutions. The S_2 value for Bearing U1 to U8 are shown in Table 4-2.

Table 4-2 Second shape factor of Bearings U1 to U8.

Bearing	U1	U2	U3	U4	U5	U6	U7	U8
Number of Layers	3	5	7	9	11	13	15	17
S_2	31.25	10.41	6.25	4.46	3.47	2.84	2.40	2.08

In CSA S6-14, there is a provision that states the rotation applied to the bridge bearings should not result in an edge deformation larger than $0.07t_r$, where t_r is the total height of the elastomeric layers. According to this provision, the maximum rotation that can be applied to these eight bearings as well as the corresponding normalized rotation are calculated and shown in Table 4-3. The normalized rotation is defined as the applied rotation divided by the analytical lift-off initiation rotation θ_0 .

Table 4-3 Maximum rotation that could be applied to Bearings U1 to U8 based on CSA S6-14.

Bearing	U1	U2	U3	U4	U5	U6	U7	U8
Maximum rotation ($\times 10^{-2}$ radians)	1.34	2.24	3.14	4.03	4.92	5.82	6.71	7.60
Corresponding normalized rotation	3.38	3.38	3.38	3.38	3.38	3.38	3.38	3.38

Note that the maximum rotation shown in Table 4-3 is only for bridge bearings based on CSA S6-14 and may not be applicable to bearings used in other areas. Bearings U1 to U8 were investigated

under the combination of 5 MPa compression and two levels of rotation. The first is to apply a 0.01 radians rotation per layer (take Bearing U4 for example, since it has 9 elastomeric layers, the applied rotation in this case is 0.09 radians), and the other level of rotation is the maximum rotation based on CSA S6-14 shown in Table 4-3.

4.2.2.2 Shape Factors

In order to study the lift-off behaviour of bearings with different shape factors, five-layer Bearings H1 to H6 were created. The material properties and the thickness of the elastomeric and reinforcement layer are the same as Bearing U2. The details of the bearings are shown in Table 4-4. The applied average compressive stress was 5 MPa, and there were two levels of rotations investigated. The first level makes the analytical $\eta = 0.7$ (the rotation was determined based on Eq. (2.76)); the other level is the maximum rotation based on CSA S6-14. The values of these two levels of rotations are shown in the last two rows of Table 4-4. Note that S_2 changes as well and could be partly responsible for the results shown in Chapter 5, but the main focus of Bearings H1 to H6 is to study the effect of S .

Table 4-4 Details of Bearings H1 to H6.

Bearing	H1	H2	H3	H4	H5	H6
$2b$ (mm)	750	625	550	469	375	268
Shape factor	31.25	26.04	22.92	19.54	15.63	11.17
Second shape factor	20.83	17.36	15.28	13.03	10.42	7.4
Rotation that makes the analytical $\eta = 0.7 (\times 10^{-2} \text{radians})$	0.43	0.66	0.89	1.33	2.40	6.10
Maximum rotation based on CSA S6-14 ($\times 10^{-2} \text{radians}$)	1.12	1.34	1.53	1.79	2.24	3.13

4.2.2.3 Compressibility and Extensibility Index, λ

The parameter λ plays an important role in the analytical solutions of the compression and bending modulus (Eq. (2.71) and Eq. (2.77)), shear stress (Eq. (3.7)), shear strain (Eq. (3.9)), and normal

stress (Eq. (3.15)) distribution. Therefore, it is of great importance to study if bearings with the same λ but different material properties and geometry would show the same lift-off behaviours. If true, it implies that designers have multiple options to achieve identical bearing properties. According to Eq. (2.71), Eq. (2.77), Eq. (3.7), Eq. (3.9), and Eq. (3.15), in order to have the same analytical results for bearings with the same λ value, η , σ_c , G , S , and θ should also be the same. Four bearings, L1 to L4, were modelled and the details are shown in Table 4-5.

Table 4-5 Details of Bearings L1 to L4.

Bearing	L1	L2	L3	L4
$2b$ (mm)	375	475	312.5	250
G (MPa)	0.8	0.8	0.8	0.8
K (MPa)	2000	1500	1800	2300
E_f (MPa)	30000	21715	19350	14330
t (mm)	12	15.2	10	8
t_f (mm)	1	3	1.5	1.2
S	15.625	15.625	15.625	15.625
λ	1.452	1.452	1.452	1.452
Number of layers	5	5	5	5
Max. rotation based on CSA S6-14 (radians)	0.022	0.022	0.022	0.022
Applied rotation (radians)	0.02	0.02	0.02	0.02

4.3 Model Description

4.3.1 Material

The two material models, namely the elastomer and the fiber, are created within the elastic domain. A linear elastic isotropic model is used to represent the fiber, which is defined by two constants, the elastic modulus, E_f , and the Poisson's ratio, ν . The elastomer was modeled as a nonlinear, elastic, nearly incompressible material, which was achieved by using a hyperelastic material model

in ABAQUS. Hyperelastic materials are described in terms of a strain energy potential, $U(\varepsilon)$, which defines the strain energy stored in the material per unit of reference volume as a function of the strain at that point in the material (ABAQUS documentation, 2016).

The Neo-Hookean model is the simplest hyperelastic model and has been selected by other researchers (Kelly & Calabrese, 2013; Al-Anany & Tait, 2015) to simulate elastomeric bearings. There are other kinds of models (such as the Mooney-Rivlin model and Ogden model), but they typically require material testing to fit the parameters, and they have more nonlinearity than the Neo-Hookean model, which makes the model more difficult to converge. The expression of the Neo-Hookean strain energy potential when considering the compressibility is

$$U = C_{10}(\bar{I}_1 - 3) + \frac{1}{D_1}(J^{el} - 1)^2 \quad (4.1)$$

where C_{10} and D_1 correspond respectively to the shear modulus, G , and the bulk modulus, K , by

$$C_{10} = \frac{G}{2}, \quad D_1 = \frac{2}{K} \quad (4.2)$$

\bar{I}_1 is the first strain invariant of the right Cauchy-Green deformation tensor, and J^{el} is the elastic volume ratio (Belivanis, 2017). For a shear modulus of $G = 0.8$ MPa, and bulk modulus of $K = 2000$ MPa, these two parameters are $C_{10} = 0.4$ and $D_1 = 0.001$.

4.3.2 Parts and Interaction

For an n -layer bearing, $(2n + 1)$ parts are created, which includes n elastomeric layers, $(n - 1)$ fiber reinforcement layers and 2 contact supports. The upper and lower contact supports were represented by two rigid wires, and each has a reference point (RP) at the center. According to AASHTO (2017), the thickness of all the intermediate elastomeric layers are the same, and the upper and the lower elastomeric layers should be less than 0.7 times the thickness of intermediate elastomeric layers. Thinner top and bottom layers results in lower shear strain at the top and the bottom of the bearing which makes the failure of the bearing more likely to occur in the

intermediate layers which is easier to detect. For validation of the model with the bonded condition, the thickness of the top and bottom elastomeric layers are selected as half of the intermediate elastomeric layer. For validation of the lift-off behaviour, the thickness of all elastomeric layers are the same. This is because the lift-off behaviour for different thickness elastomeric layers is different; currently no analytical solution is available that accounts for different layer thicknesses. Therefore, the same thickness for all elastomeric layers makes it possible to do the comparison between the analytical and numerical solutions. The sketches of Bearing B2 and Bearing U2 models are shown in Figure 4-1.

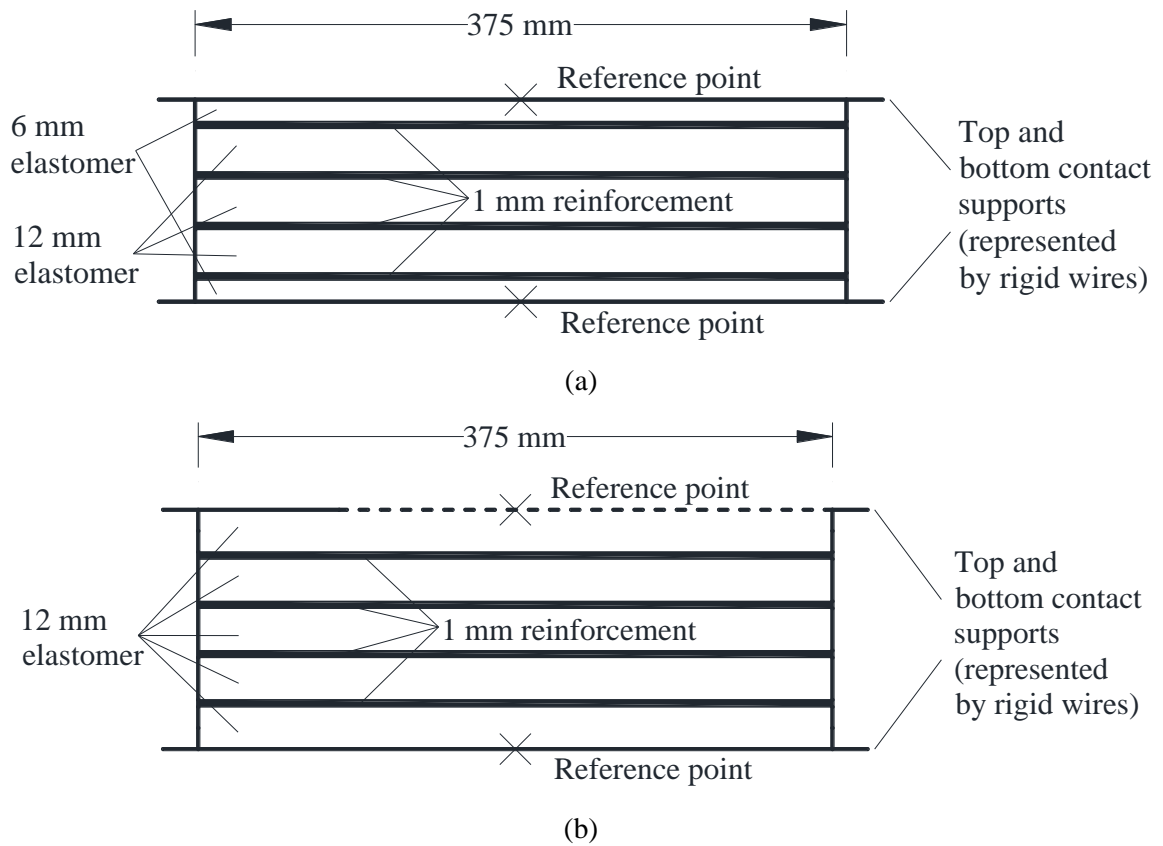


Figure 4-1 Sketch of Bearing (a) B2; (b) U2.

All the adjacent elastomer and fiber surfaces are connected to each other by the tie constraint. For bonded cases, the top and the bottom rigid wires are also tied to the adjacent elastomeric surfaces to simulate the bonding condition. However, for unbonded cases, the connection between the rigid wire and the adjacent surfaces is supposed to be represented by the rough friction formulation for

the tangential behaviour and hard contact for the normal behaviour. The rough formulation prevents slip once points are in contact (ABAQUS documentation, 2016), which means the frictional coefficient is infinite. However, due to convergence issues, only 75% of the top elastomeric surface (shown as the black dotted line in Figure 4-1 (b)) was defined to interact with the top contact support as unbonded. The remaining interaction was set to be bonded. Note that the slippage between the contact support and the adjacent elastomeric layer is neglected for the unbonded bearings considered in this research. The same technique of high friction was also used by Al-Anany & Tait (2015), Toopchi-Nezhad et al. (2011), and Spizzuoco et al., (2014); it is common when modelling elastomeric bearings. The effect of slippage on the behavior of the bearings is beyond the scope of this research. In fact, this approach assumes that there would be no slip in the contact areas where lift-off does not occur. Numerous variations of bonded areas were considered and it was found that there was no significant impact on the results provided the bonded area did not influence lift-off (see Appendix A). Thus, this simplification was considered acceptable. Kelly et al. (2009) studied the effect of friction on the behavior of bearing. They found that with the decrease of the friction coefficient, the peak internal pressure in the elastomer will be considerably decreased.

4.3.3 Boundary Conditions and Loads

During simulations, the loading sequence is important, and this is realized by creating different steps in ABAQUS. In the steps different loads and boundary conditions were applied. ABAQUS has a special initial step by default at the beginning of model's step sequence, which defines boundary conditions and predefined field at the very beginning of the analysis (ABAQUS documentation, 2016). For all the simulations, the lower contact support was fixed in the initial step and maintained through the entire simulation by constraining all the degrees of freedom of the RP. The Nlgeom (nonlinear geometry) was switched on for all cases because the deformation of the elastomer is large and causes geometric nonlinearity; this also accounts for large strain.

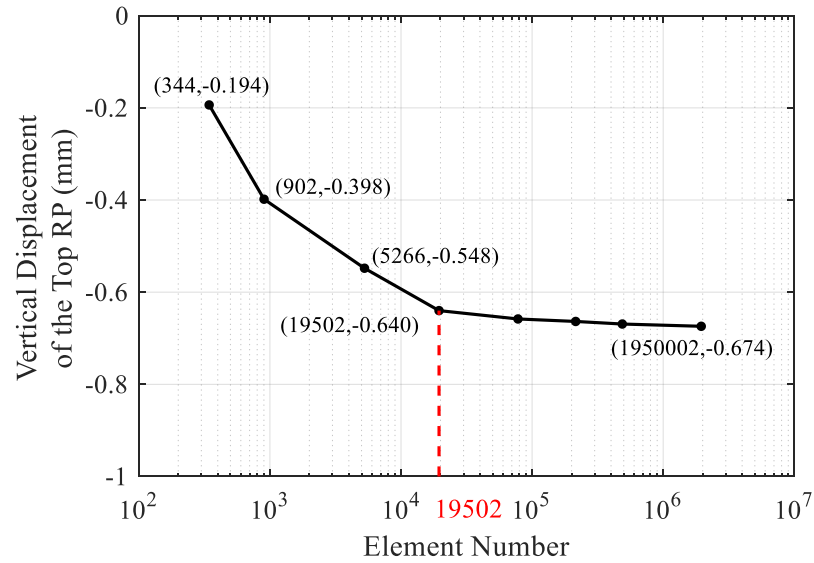
When validating the model, only one step (step-1) was created besides the initial step. For pure compression scenarios, the compression was realized by applying downward concentrated force to the RP on the upper rigid wire in step-1. The applied average compressive stress was selected to be 5 MPa, and the amplitude of the force based on a unit length (1 mm) was 1875 N. For the pure bending case, U_1 and U_2 (the horizontal and the vertical displacement) of the RP on the upper rigid wire were constrained in the initial step and kept through the entire simulation, which corresponds to the assumption of the analytical pressure solution. Note that this does not result in any substantial lateral loads. The moment was developed by the displacement control method. A rotational displacement of 0.01 radians was applied to the RP of the upper wire in step-1.

When validating the analytical lift-off behaviour, the bearings were subjected to the combination of compression and rotation. Two steps (step-1 and step-2) were created besides the initial step. The applied average compressive stress was 5 MPa, which was applied to the top RP in step-1 and held on to step-2. The rotation was applied to the top RP. During lift-off, the effective area of the bearing in contact with the supports is reduced resulting in lower compressive stiffness and more downward displacement. Therefore, in step-2, only U_1 of the top RP was constrained.

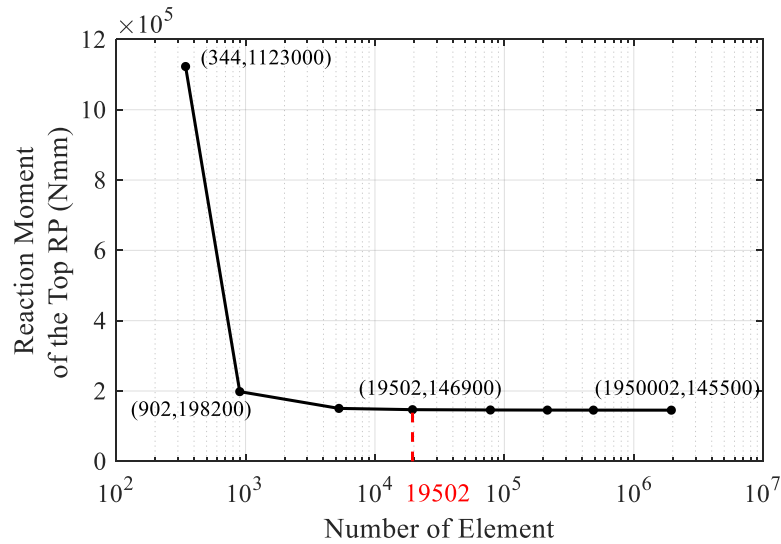
4.3.4 Element Type and Size

The four-node bilinear plane strain quadrilateral, hybrid element (CPE4H) was used to model the elastomer and the fiber reinforcement layers. A convergence study was conducted based on Bearing B2 under pure compression (5 MPa) and pure rotation (0.01 radians). The element size for elastomer and reinforcement layers were kept the same. The general behaviour, namely the vertical displacement (U_2) and the reaction moment of the RP on the upper rigid wire, were compared for the pure compression and pure bending scenario, respectively. Apart from that, the shear stress on the compressive edge of the second elastomeric layer top surface is also considered in the convergence study as the local behaviour.

Figure 4-2 shows the convergence trend with more elements being created for general behaviours. The errors for 19502-element case results are 0.65% and 0.82% for pure compression and pure bending cases, respectively, compared with the 1950002-element case. This error was considered small enough to obtain accurate results while retaining computation efficiency. When the number of elements was 19502 for the five-layer bearing, the element size was 1 mm.



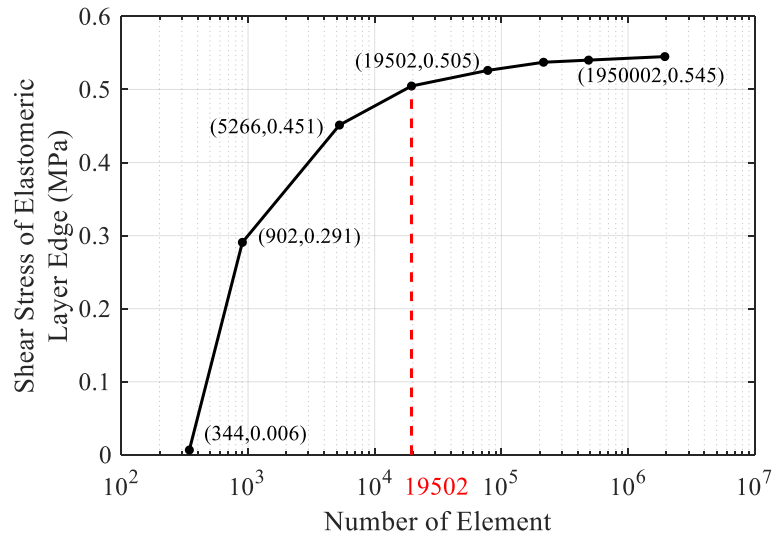
(a)



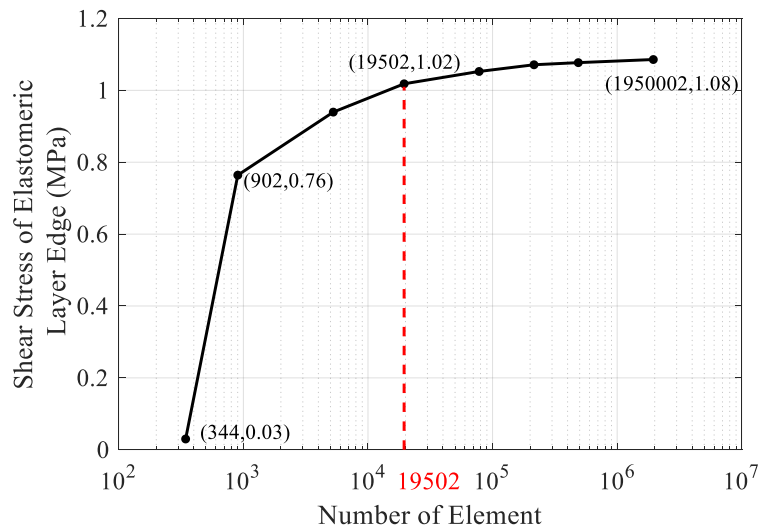
(b)

Figure 4-2 Convergence study of general behaviour for B-FREB (a) pure compression; (b) pure bending.

Figure 4-3 illustrates the convergence trend of local shear stress for the compression and bending cases. Note that there are numerical errors for the shear stress distribution on the compressive edge; therefore, the shear stress data on the edge was derived by extrapolation within the nearby stable range. The extrapolation technique to find an accurate value of shear stress was also used by Constantinou et al. (2011). When the number of elements was 19502, the relative error is 4.67% and 5.96% for compression and bending cases, respectively, which is also accurate.



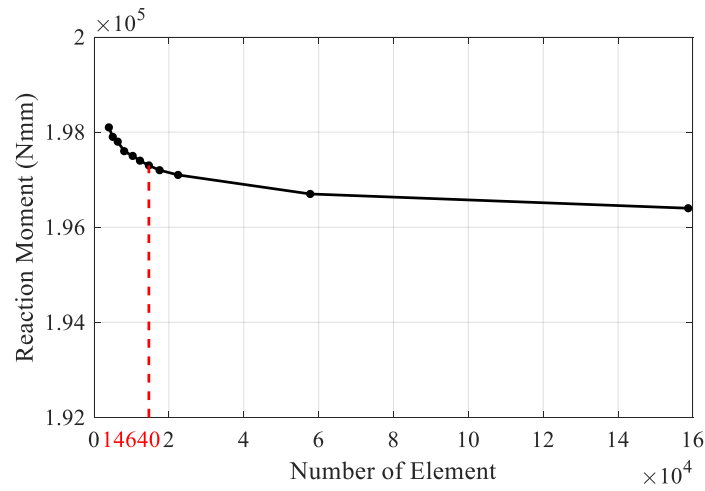
(a)



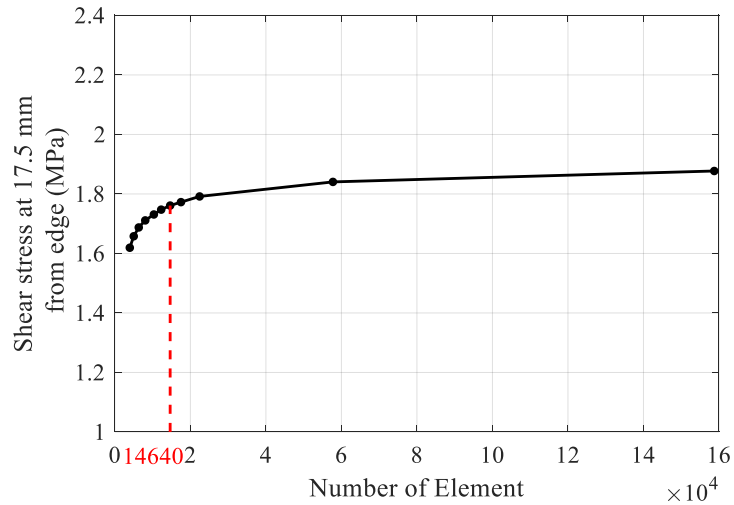
(b)

Figure 4-3 Convergence study of local behaviour for B-FREB (a) pure compression; (b) pure bending.

Therefore, 1 mm was selected as the element size for all bonded scenarios. This size is also used in Al-Anany & Tait's (2015) and Van Engelen et al. (2014). A similar convergence study was conducted based on Bearing U1 under the combination of compression (5 MPa) and rotation (0.03 radians). The reaction moment is also studied as the general behaviour (the result is shown in Figure 4-4 (a)), and the shear stress at the location which is 17.5 mm from the compressive edge of the intermediate elastomeric layer top surface is used to conduct the local convergence study (the result is shown in Figure 4-4 (b)).



(a)



(b)

Figure 4-4 Convergence study for U-FREB (a) general behaviour; (b) local behaviour.

When the number of element equals to 14640 (the corresponding element size is 1 mm), the error for general and local results are 0.31% and 4.3%, respectively. This means 1 mm element size could also be used for the unbonded cases. Overall, the element size for all cases in this research is selected as 1 mm.

Chapter 5 Results and Discussions

5.1 Notes on Results

The deformed shape of all the bearings considered in this research as well as the meshing of 7-layer bearings are shown in Appendix B. During the simulation, the mechanical properties of the elastomer vary with strain level due to the nonlinearity of the Neo-Hookean model. This makes it difficult to select the material property based on only one strain level to substitute into the analytical expressions, which assume a linear elastic material, for comparison. Based on experimental experience (Das et al. 2016) and recommendations in codes (ISO 22762-3:2018, BS EN 15129:2018), the shear modulus of the elastomer was selected at a shear strain of 1.0. The amplitude of the shear modulus when the shear strain equals 1.0 was derived from the Neo-Hookean model in ABAQUS, which was $G = 1.0$ MPa. It could be found that some of the numerical plots do not fit well with the analytical curve, but it is intuitively expected because $G = 1.0$ MPa is only a reference; it does not reflect the real shear modulus of the bearing under certain loading condition, which varies with strain amplitude. The numerical results for B-FREBs under pure compression and pure bending conditions are also compared with the analytical results based on $G = 0.8$ MPa and shown in Appendix C. For the U-FREBs under the combination of compression and rotation, the value of $G = 1.0$ MPa is considered appropriate, as shown in Section 5.3. Finding a value of G that reflects the real state of the bearing is beyond the scope of this research. If the tendency of the numerical and the analytical curves agree with each other, it means the analytical solution is correct and reasonable based on the code recommended value of G . By changing the G value, they could fit better than what they shown in the following subsections. Selected results for Bearings H1 to H6 and Bearings L1 to L4 are shown in Appendix D and Appendix E, respectively. Appendix F shows the shear stress and shear strain distribution results of all the unbonded bearings after extrapolating the unsmooth part in the compressive edge.

The percent error in this chapter are defined as

$$\text{Error} = \frac{(\text{Numerical result} - \text{Analytical result})}{\text{Analytical result}} \times 100\% \quad (5.1)$$

A positive error means that the numerical results are greater than the analytical results in magnitude, and a negative error means that the numerical results are smaller than the analytical results in magnitude.

5.2 Model Validation

5.2.1 Vertical Behaviour

Figure 5-1 shows the numerical and the analytical force-displacement relationship of B-FREBs under 5 MPa compression. The legends of the plots are defined such that B3 N means Bearing B3 numerical and B5 A means Bearing B5 analytical, this convention applies to all the figures in this chapter. The force-displacement relationship is nearly linear for all scenarios considered. When the applied force equals to 1875 N (namely the average compressive stress is 5 MPa), the errors between the numerical and the analytical vertical displacement for the five bearings are shown in Table 5-1. As the number of layers increases, the error also increases.

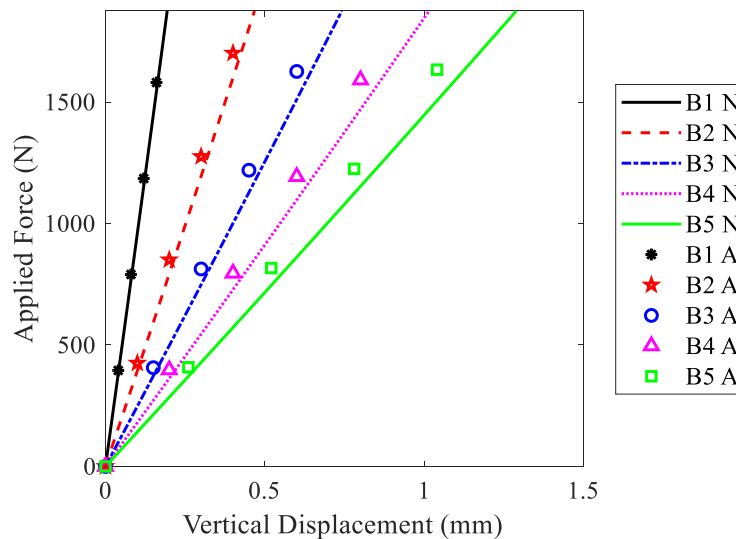


Figure 5-1 Vertical compression behaviour of B-FREBs.

Table 5-1 Error between the numerical and the analytical vertical displacement at an average compressive stress of 5 MPa.

Bearing	B1	B2	B3	B4	B5
Error (%)	1.99	6.03	7.14	7.66	7.95

Figure 5-2 gives the compression modulus (E_c) under different amplitudes of applied average compressive stress (σ_c), and the error between the analytical solutions and the numerical results is illustrated in Figure 5-3. As the number of elastomeric layers increases, the numerical E_c drops from approximately 630 MPa to 476 MPa when σ_c equals to 5 MPa. The numerical results of E_c increase slightly with the increase of σ_c , while the analytical values of E_c remain constant. This is because the analytical pressure solution assumes the elastomer is linear-elastic, whereas the Neo-Hookean model is applied in the FEA model exhibits nonlinear behaviour. Since the stress-strain relationship of Neo-Hookean model becomes stiffer with increased strain, the compression modulus increases as the stress level increases.

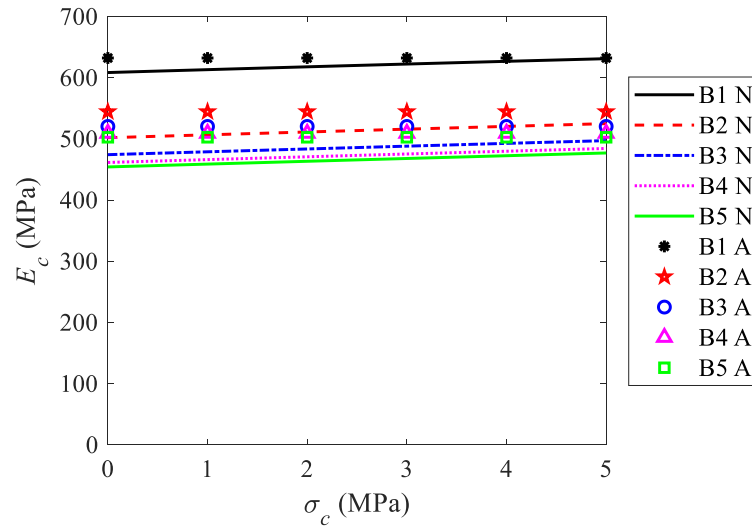


Figure 5-2 Compression modulus under different σ_c values.

With the increasing number of elastomeric layers, the error between the analytical and the numerical result increases, and with the increase of σ_c , the absolute error decreases. Under zero σ_c ,

the absolute error increases from slightly below 4% for Bearing B1 to around 10% for Bearing B5, whereas under 5 MPa σ_c the absolute error increases from around 0.2% for Bearing B1 to 5% for Bearing B5.

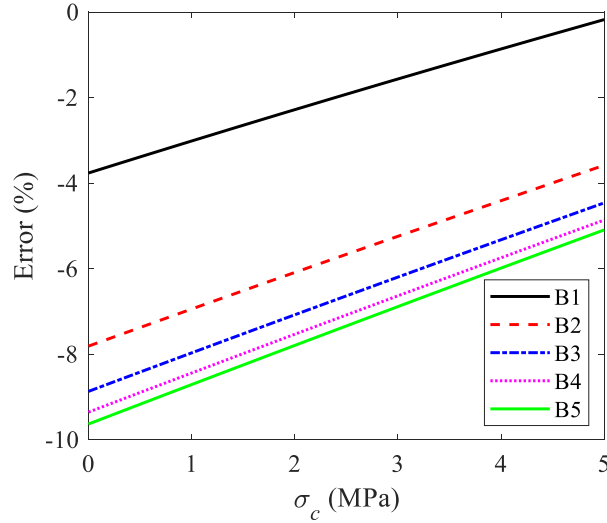


Figure 5-3 Error between the analytical solutions and the numerical results of the compression modulus.

If $G = 0.8$ MPa is substituted into the analytical expression (see Figure C 2 and Figure C 3 in Appendix C), when σ_c equals to zero, the error decreases from 6.16% for Bearing B1 to 1.23% for Bearing B5, whereas under a σ_c of 5 MPa, the error drops from 10.11% for Bearing B1 to 6.32% for Bearing B5. Figure 5-4 shows the stress distribution of Bearing B2 under 5 MPa average compressive stress, where S11, S22, S33 and S12 represent σ_{xx} , σ_{zz} , σ_{yy} and τ_{xz} in Eq. (2.22), respectively. Because nodes common to two or more elements will receive multiple contributions of stress extrapolated from each element, the average threshold is used to govern the extent of averaging. The 75% shown in the legend of Figure 5-4 means that if the relative difference between contributions at a node is larger than 75%, Abaqus will not average the contributing values and the results will appear discontinuous at that node. By using a higher percentage of the average threshold, the contour plots will become smoother and achieve a more continuous effect (ABAQUS documentation, 2016).

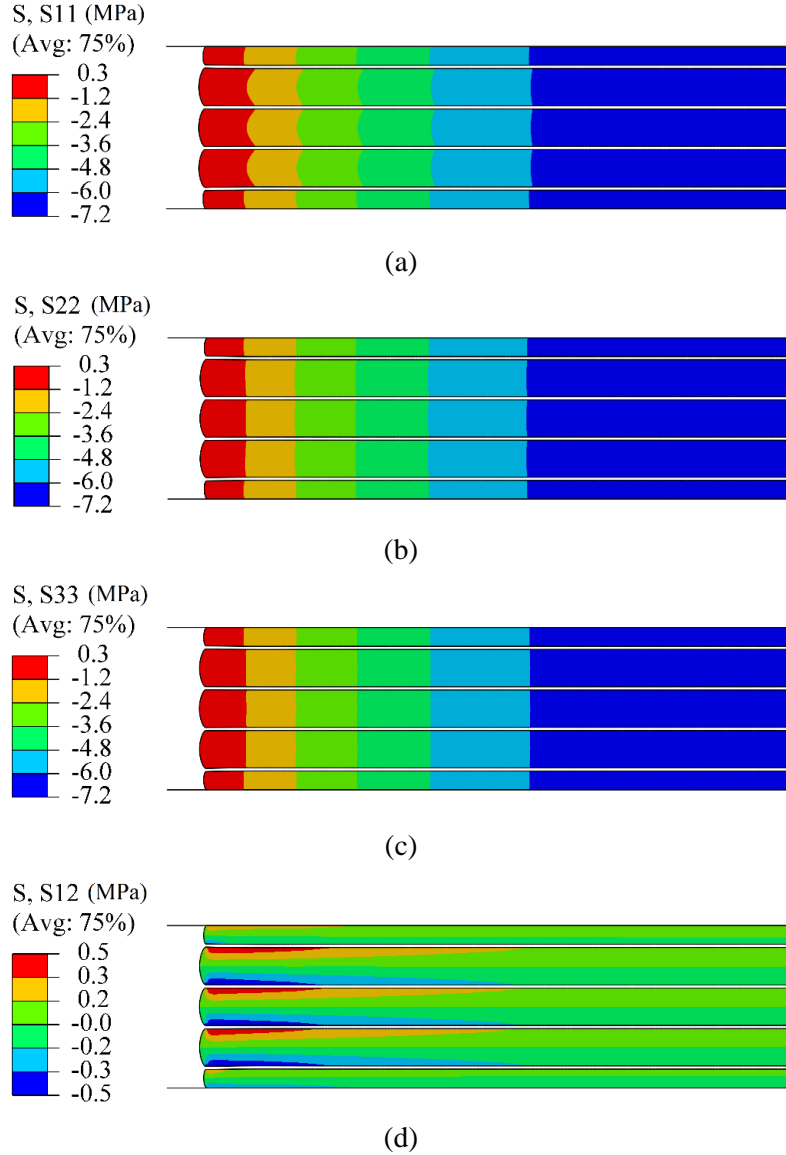


Figure 5-4 Stress distribution of the five-layer bearing B2 under compression load (a) S11 (σ_{xx}); (b) S22 (σ_{zz}); (c) S33 (σ_{yy}); (d) S12 (τ_{xz}).

Due to symmetry, only the left-hand side of the bearing is shown. Since the fiber is much stiffer than rubber, the stress level in the fiber is much higher than the rubber. Therefore, the fiber is excluded in Figure 5-4. The distribution of the three normal stress components in the rubber are close to each other, the relative error between any two of the three components are mostly below 1%. This means the assumption described by Eq. (2.23), namely the stress state of the rubber is dominated by the internal pressure, is reasonable and correct. The stress remains nearly constant

along the thickness of each layer, which verifies that p_c in Eq. (2.63) is not a function of z . Figure 5-4 (d) shows that τ_{xz} varies along both the width and the thickness, which means it is the function of both x and z , as illustrated in Eq. (2.40). The maximum shear stress occurs at the top and bottom of each elastomeric layer near the edge, as indicated by Eq. (2.41).

Four paths in the bearing were selected to compare the analytical and the numerical results of the stress distribution under compression, they are shown in Figure 5-5. Path-1 and Path-2 were selected as the middle plane of the third and the first elastomeric layer, respectively. Path-3 was selected as a plane that is a 3 mm distance from the upper surface of the second elastomeric layer. Path-4 was 10 mm from the left edge of the second elastomeric layer.

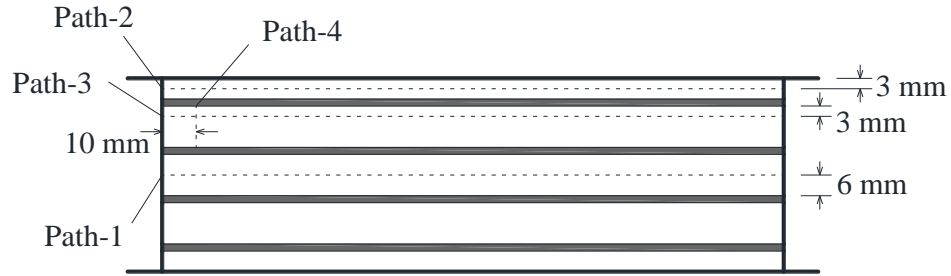


Figure 5-5 Paths selected for comparison of the stress distributions under compression.

Figure 5-6 illustrates the normal stress distribution along Path-1 and Path-2. The maximum normal stress occurs in the middle of the pad's width. The numerical curve of the normal stress distribution along Path-1 visibly fits better with the analytical curve than that along Path-2. This is because Path-1 is located in the intermediate elastomeric layer, which is bonded between two extensible and flexible reinforcement layers. This matches with the analytical model shown in Figure 2-14. However, Path-2 is located in the top elastomeric layer, which is bonded between a rigid wire and a reinforcement layer. The boundary condition is different from that of the analytical model, and it deviates from the analytical curve. The maximum errors between the numerical and the analytical results occur in the middle of the two paths, which are -0.6% and 5.1% for Path-1 and Path-2, respectively. If $G = 0.8$ MPa (see Figure C 4 in Appendix C), the maximum errors are -1.6% and 3.8% for Path-1 and Path-2, respectively.

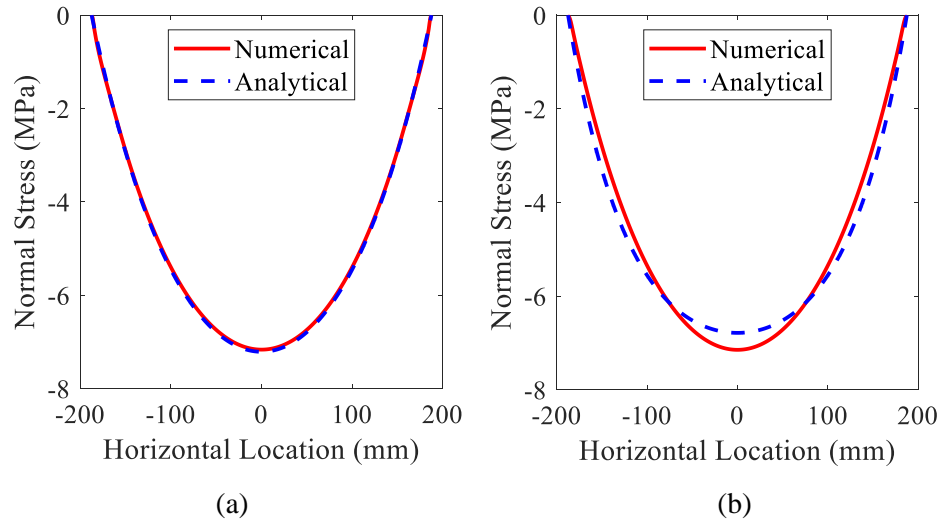


Figure 5-6 Analytical and numerical normal stress distribution along the bearing width under pure compression (a) Path-1; (b) Path-2.

Figure 5-7 illustrates the shear stress distribution of an intermediate elastomeric layer along Path-3 and Path-4. There are sharp changes at the two ends of the shear stress distribution along Path-3. Theoretically, the shear stress should be zero on the vertical free edges of the elastomer in the FE model, thus, for equilibrium, the shear stress at the two edges of the intermediate rubber layer should also be zero. But the analytical model predicts non-zero shear stress along the horizontal interface between the elastomer and the reinforcement layers as a simplification. The error between the numerical and the analytical maximum shear stress along Path-3 and Path-4 is -7.5% and -10.5% by observation, respectively. If $G = 0.8$ MPa (see Figure C 5 in Appendix C), the maximum errors are -4.8% and -8.7% for Path-3 and Path-4, respectively. The difference between the errors for different G values indicates the importance of identifying the proper value of G to be used in the analytical solutions.

Overall, good agreement of the analytical and the numerical results are shown in Figure 5-6 and Figure 5-7. Deviations in the analytical and the numerical results can be explained based on the simplifying assumptions made when deriving the analytical solutions.

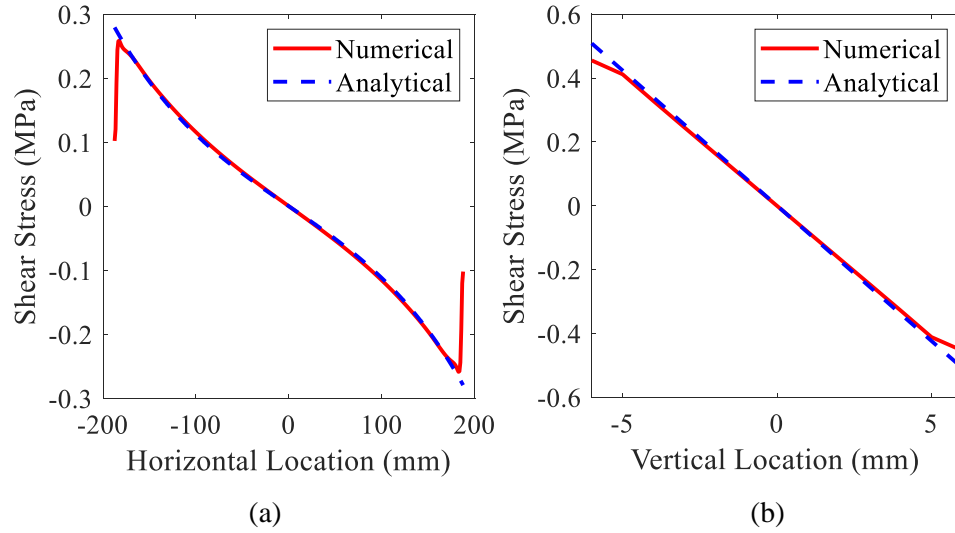


Figure 5-7 Analytical and numerical shear stress distribution of an intermediate elasotmeric layer under pure compression (a) Path-3; (b) Path-4.

5.2.2 Rotational Behaviour

Figure 5-8 illustrates the numerical and analytical results for the pure rotation scenarios. The relationship is approximately linear and the analytical curves are stiffer than the numerical ones. The error between the numerical and the analytical results of the reaction moment when the applied rotation equals to 0.01 radians are -13.7%, -14.1%, -14.4%, -14.5%, and -14.6%, respectively for Bearing B1 to B5. Such divergence is likely because the magnitude of G (1.0 MPa) substituted into the analytical solution may not reflect the real material condition under 0.01-radian rotation; the effective G may be smaller than 1.0 MPa. The errors for the five bearings are approximately the same, but also show a slightly increasing magnitude as the number of layers increases.

If $G = 0.8$ MPa (see Figure C 6), the error between the numerical and the analytical results of the reaction moment when the applied rotation equals to 0.01 radians are 2.3%, 2.7%, 2.5%, 2.4%, and 2.4%, respectively for Bearing B1, B2, B3, B4, and B5.

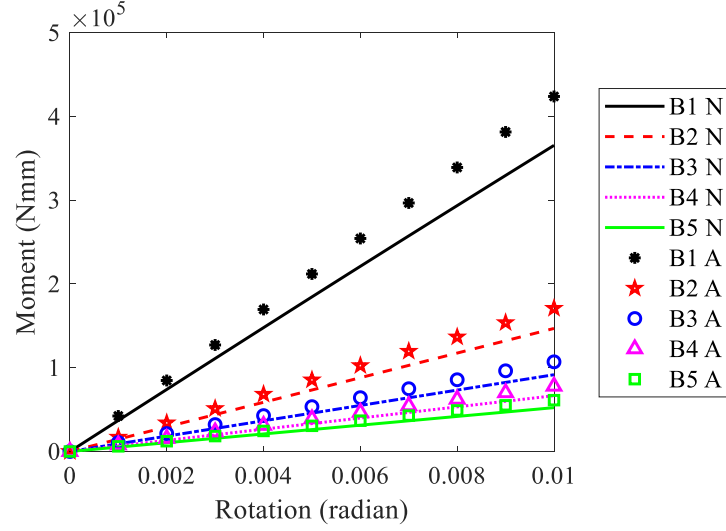


Figure 5-8 Rotational behaviour of B-FREBs.

Figure 5-9 illustrates the analytical and the numerical results of the bending modulus (E_b) under different amplitudes of the applied rotation. The amplitude of the numerical E_b decreases from about 200 MPa for Bearing B1 to around 140 MPa for Bearing B5. The numerical results are not sensitive to increasing rotation except for the Bearing B1, which shows a decreasing trend. A minor increasing trend is observed in the other case due to the stiffening material properties. The error between the numerical results and the analytical solutions of E_b is illustrated in Figure 5-10. The maximum error is approximately -14.5% under different rotations for all scenarios except for Bearing B1, where the error increases rapidly from -12.5% to -15.5%. The reason for the sudden reduction of E_b for Bearing B1 is postulated to be as follows. Bearing B1 has only 3 elastomeric layers, and therefore, the rotation per layer is the largest among the 5 B-FREBs. The rotation per layer is large enough to make the fiber layers start to warp (as shown in Figure B 2 (a)), and this makes the bending modulus decrease. Actually, as the magnitude of the applied rotation passes 0.01 radians and becomes larger and larger, the bending modulus for all the other four bearings will also reduce due to warping effects. Warping is important (Pinarbasi & Mengi, 2008), but the effects are not considered in this research and are also not include in design codes (e.g. CSA S6-14, 2014).

If $G = 0.8$ MPa (see Figure C 7 and Figure C 8), the error is around 2.5% under different rotations for all the bearings except for Bearing B1, of which the error drops rapidly from 3.5% to 0.5%.

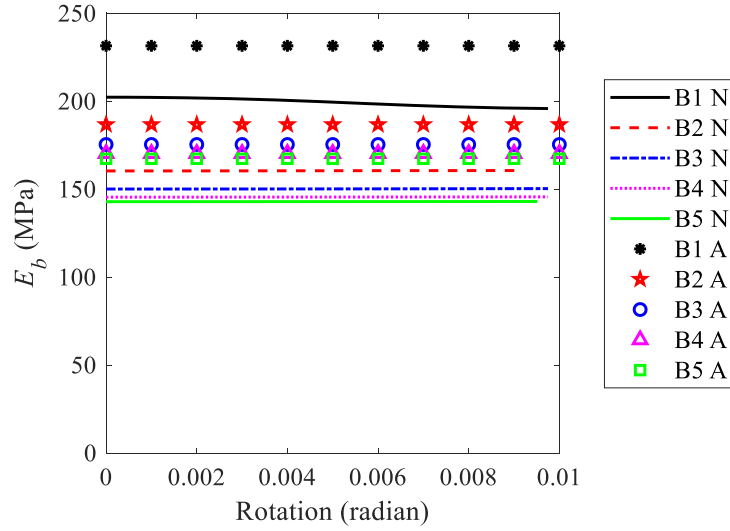


Figure 5-9 Bending modulus as a function of rotation.

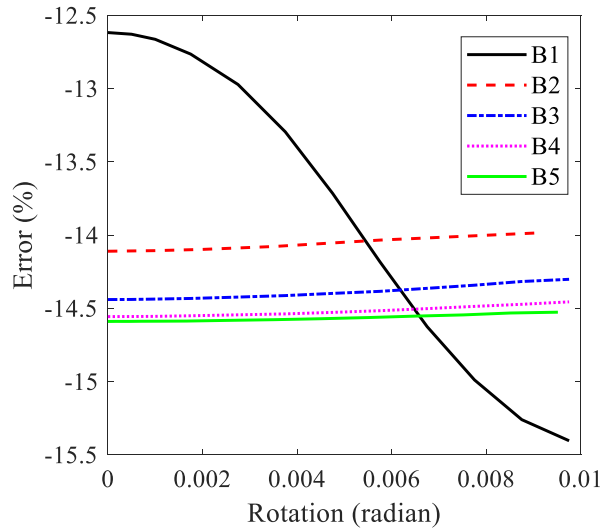


Figure 5-10 Error between the analytical solutions and the numerical results of the bending modulus.

The stress distribution of Bearing B2 under 0.01-radian rotation is shown in Figure 5-11. Similar to the compression case, the stress distribution contour plots verify the pressure solution assumptions.

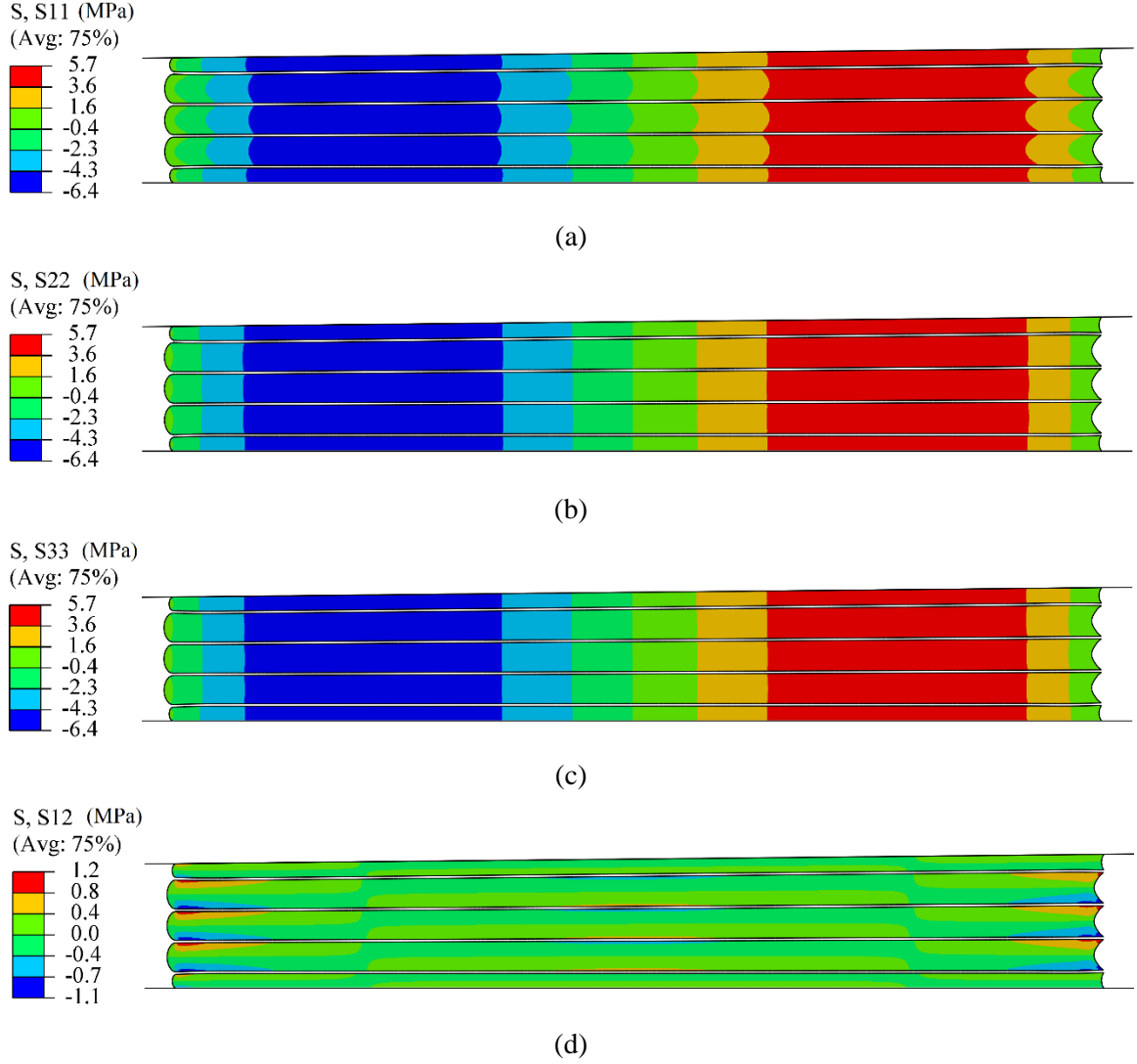


Figure 5-11 Stress distribution of the five-layer bearing B2 under pure bending (a) S11 (σ_{xx}); (b) S22 (σ_{zz}); (c) S33 (σ_{yy}); (d) S12 (τ_{xz}).

When the applied rotation equals to 0.01 radians the normal stress distribution along Path-1 and Path-2 and the shear stress distribution along Path-3 and Path-4 in Figure 5-5 are shown in Figure 5-12 (a), Figure 5-12 (b), Figure 5-13 (a) and Figure 5-13 (b), respectively. Similar to the bending modulus results, the numerical results of the stress distribution deviate to some extent from the analytical solution. The maximum error between the numerical and the analytical normal stress distribution along Path-1 and Path-2 are -21% and -18.9%, respectively. The error between the

maximum shear stress along Path-3 and Path-4 are -27.5% and -20.2%, respectively. Extrapolation could be used to get more accurate numerical results of the maximum shear stress at the edge.

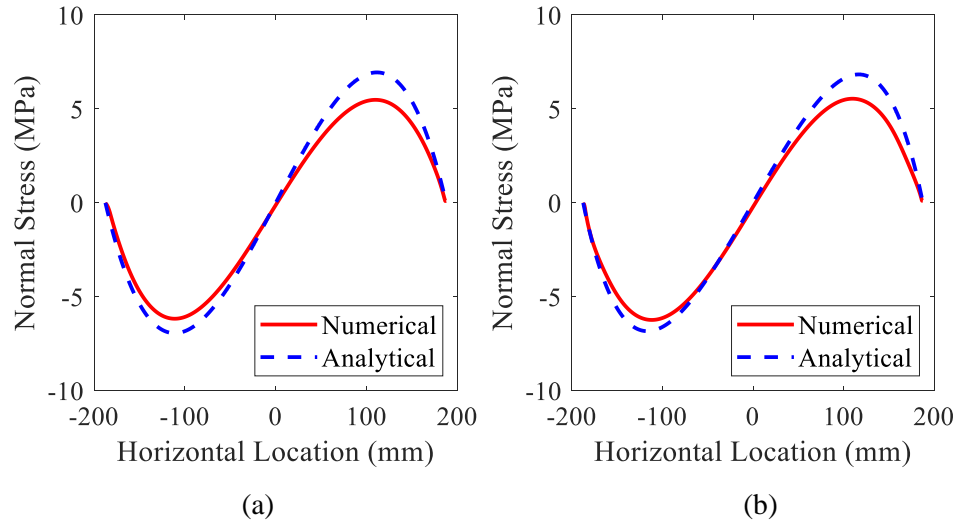


Figure 5-12 Analytical and numerical normal stress distribution along the width under pure bending (a) Path-1; (b) Path-2.

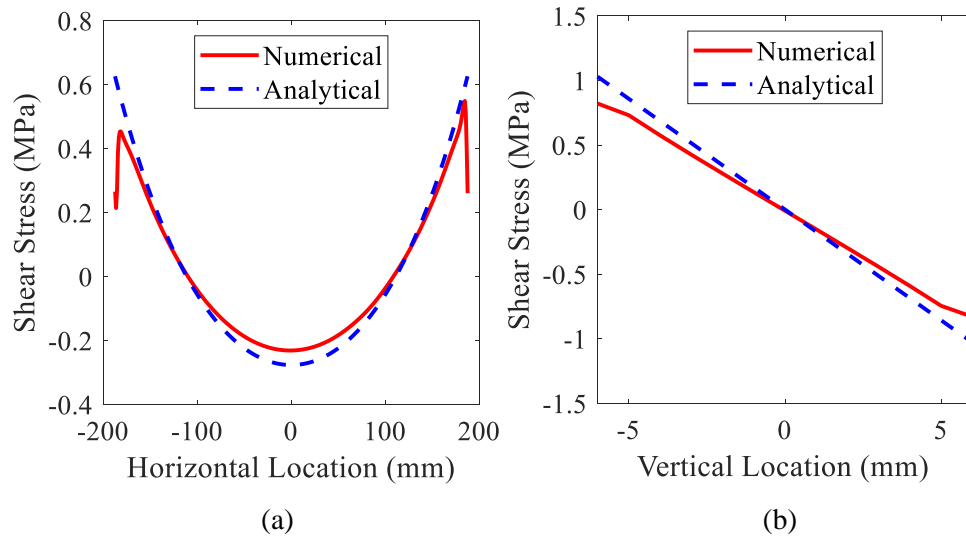


Figure 5-13 Analytical and numerical shear stress distribution of an intermediate rubber layer under pure bending (a) Path-3; (b) Path-4.

If $G = 0.8$ MPa (see Figure C 9 and Figure C 10), the maximum error between the numerical and the analytical normal stress distribution along Path-1 and Path-2 are 6% and 8.6%, respectively. The error between the maximum shear stress along Path-3 and Path-4 are -12.2% and -3.9% (with

no extrapolation), respectively. The smaller error compared with the ones when $G = 1.0$ MPa indicates that the effective value of G in the pure bending scenarios considered is closer to the initial value (0.8 MPa).

5.3 Lift-off Behaviour Validation

The numerical and analytical behaviour of the U-FREBs are shown in the following subsections, which include the scenarios considering the effect of the number of layers, the shape factors, and the compressible and extensible index, λ . When evaluating the effect of the number of layers, the lift-off initiation rotation, the moment-rotation relationship, the shear stress, the normal stress, and the shear strain distributions will be discussed for Bearings U1 to U8. When assessing the influence of the shape factors and the compressibility and extensibility index λ , the effective part of the bearings, the moment-rotation relationship, and the shear stress distribution will be discussed for Bearings H1 to H6 and Bearings L1 to L4.

5.3.1 Effect of the Number of Layers

5.3.1.1 Lift-off Initiation Rotation

The analytical and the numerical results of θ_0 for Bearings U1 to U8 are shown in Table 5-2. Also, θ_0 per layer (θ_0/n), and the absolute error as well as the percent error between the numerical and the analytical θ_0/n are shown in the same table. The numerical θ_0 was determined by setting the increments in the vicinity of the lift-off initiating point very small (the approximate lift-off initiating point was determined by running relatively rough models previously), and letting θ_0 be equal to the applied rotation when there is a just-visible gap generated between the top rigid wire and the adjacent elastomeric surface.

Table 5-2 Analytical and numerical θ_0 for Bearings U1 to U8.

Bearing	Analytical θ_0 ($\times 10^{-2}$ radians)	Numerical θ_0 ($\times 10^{-2}$ radians)	Analytical θ_0/n (\times 10^{-2} radians)	Numerical θ_0/n (\times 10^{-2} radians)	Absolute error of θ_0/n ($\times 10^{-2}$ radians)	Percent error of θ_0/n (%)
U1	0.40	0.42		0.141	0.008	6.2
U2	0.67	0.73		0.146	0.013	9.6
U3	0.93	1.04		0.149	0.016	11.9
U4	1.20	1.37	0.133	0.152	0.019	14.3
U5	1.46	1.72		0.156	0.023	17.1
U6	1.73	2.08		0.160	0.026	19.9
U7	2.00	2.43		0.162	0.029	21.4
U8	2.26	2.80		0.164	0.031	23.5

Note that the analytical θ_0 per layer is the same for bearings with a different number of layers. The numerical θ_0 per layer is higher than the analytical result (note that this is beneficial according to CSA S6-19 because the analytical solution (Van Engelen, 2019) is conservative, and the code currently prohibits lift-off to occur), and it increases as the number of layers increase. One of the reasons is that the magnitude of shear modulus substituted into the analytical expression may not reflect the real material property. Also, as the number of layers increases, the interaction between adjacent layers becomes more complex (as shown in Figure B 3). The analytical solution is based on one layer and does not account for global effects which appear to become more prevalent as the number of layers increases. Even though the percent error is from 6.2% for Bearing U1 to 23.5% for Bearing U8, the absolute error is small (0.00008 radians for Bearing U1 and 0.00031 radians for Bearing U8).

5.3.1.2 Moment-Rotation Relationship

The numerical and the analytical moment-rotation relationship for Bearings U1 to U8 subjected to the combination of axial compression (5 MPa) and rotation (0.01 radians per layer) are shown in Figure 5-14. The comparison between the results for different bearings is better illustrated in the normalized relationship shown in Figure 5-15. The horizontal axis represents θ/θ_0 , and the vertical axis represents M/M_0 , where θ_0 and M_0 are the analytical solution of the lift-off initiation rotation and the reaction moment corresponding to the lift-off initiation, respectively.

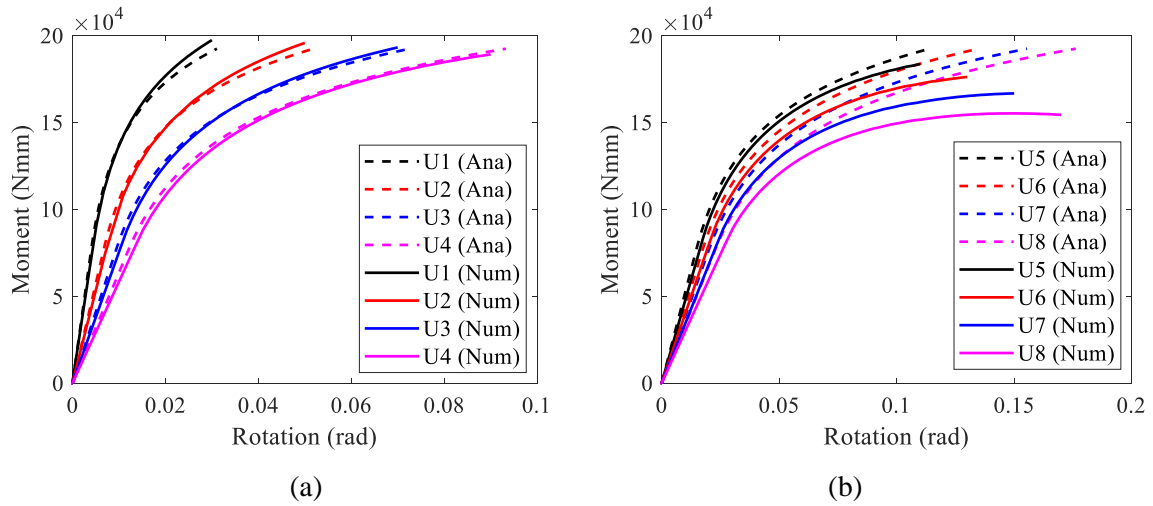


Figure 5-14 Moment-rotation relationship for Bearings (a) U1 to U4; (b) U5 to U8.

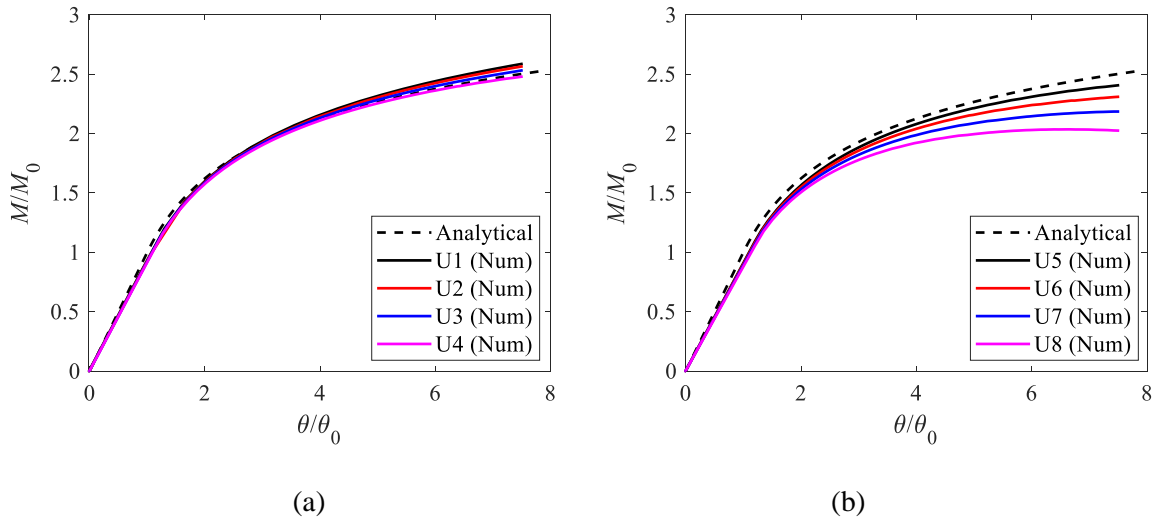


Figure 5-15 Normalized moment-rotation relationship for Bearings (a) U1 to U4; (b) U5 to U8.

When the normalized rotation is smaller than 2, the curves for all the bearings are very close. But when the normalized rotation increases, the numerical normalized moment decreases as the number of layers increases, which means more layers makes the normalized bending stiffness softer. Especially for Bearing U5 to U8, this tendency starts even before the normalized rotation reaches 2. The deformed shape of Bearing U1, U4, and U8 are shown in Figure 5-16 (the deformed shape of all eight bearings are shown Figure B 3 in Appendix B). As the number of layers increases, the global effects, represented by the deformation, become more obvious. The reinforcement layers warp, and that could be one of the reasons that the bending stiffness decreases as the rotation increases for bearings with more layers. For Bearing U8, the reaction moment even decreases when the normalized rotation is around 7, which could mean the stability problem comes into play.

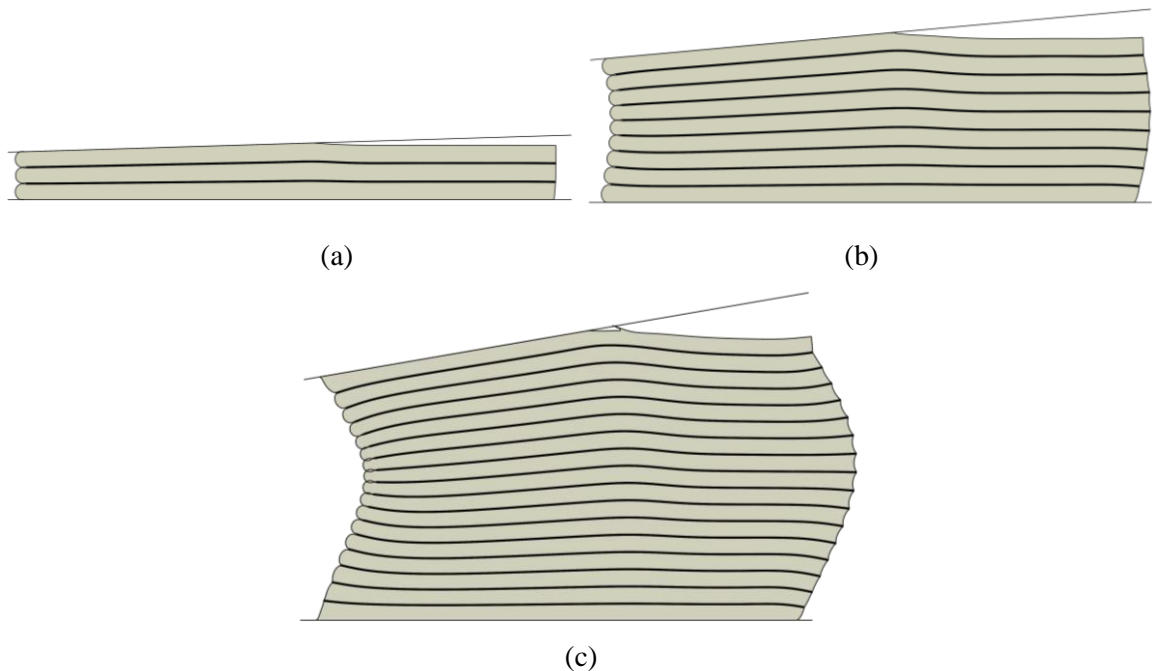


Figure 5-16 Deformed shape of Bearing (a) U1; (b) U4; (c) U8 under 0.01 radians rotation per layer and 5 MPa compression.

The error between the numerical and the analytical result of the normalized moment when the normalized rotation equals to 2 and 7, and the maximum based on CSA S6-14 (normalized rotation equals to 3.38) are listed in Table 5-3, and also plotted in Figure 5-17. The overall tendency is that

as the rotation increases, the error also increases. Note that the numerical curves cross over the analytical curves for Bearing U1, U2 and U3. For Bearing U4, the numerical curve approaches the analytical curve as the rotation increases. For Bearing U5, the numerical curve diverges with the analytical curve, but the tendency is small compared to Bearing U6, U7, and U8.

Table 5-3 Percent error between the numerical and the analytical M/M_0 .

Bearing	$\theta/\theta_0=2$	$\theta/\theta_0=3.38$	$\theta/\theta_0=7$
U1	-1.43	0.38	3.17
U2	-1.94	0.20	2.39
U3	-2.10	-0.19	1.12
U4	-2.84	-1.04	-0.76
U5	-3.58	-2.21	-3.41
U6	-4.52	-3.77	-7.06
U7	-5.68	-5.80	-11.58
U8	-7.39	-8.40	-17.46

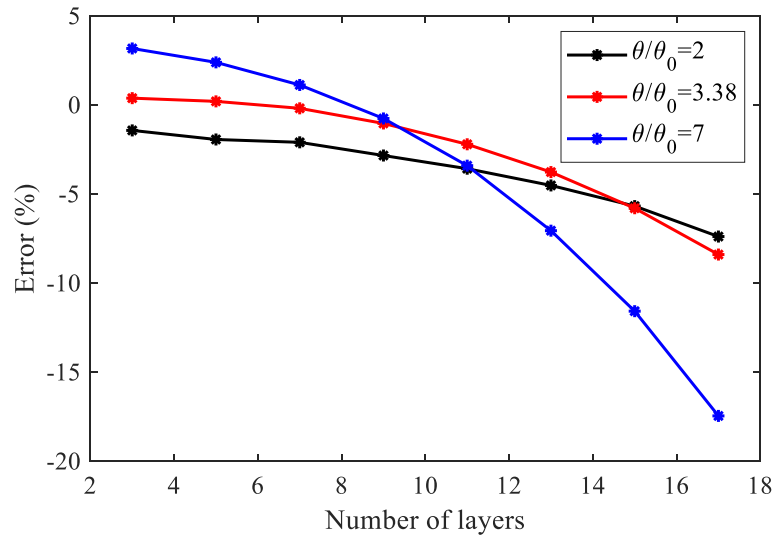


Figure 5-17 Error between the numerical and the analytical results of the normalized moment when the normalized rotation equals to 2, 3.38, and 7.

5.3.1.3 Shear Stress Distribution

The analytical and the numerical shear stress distributions along the top surface of the second elastomeric layer when the average rotation applied to each layer is 0.01 radians are shown in Figure 5-18. Theoretically, the curve for all the cases should overlap each other, as the geometry and the loading conditions are the same for the second elastomeric layer of all U-FREBs considered. But the reality is that they do not match perfectly. According to the assumption that the unloaded part has no internal force, the analytical result of the shear stress in the unloaded part is zero. But as the number of layers increases, the magnitude of the shear stress within the unloaded part becomes larger. As shown in Figure 5-16 (and in Figure B 3), as the number of layers increases, the bearing becomes slenderer, which tends to deform from the central vertical axis. This makes the bearing globally bulge laterally on the right-hand-side, and therefore shear stress is developed in it. For Bearings U1 to U6, on the compressive edge (left-hand-side), even if the shear stress distributions do not fit well with each other, the overall tendency match well with the analytical curve. For Bearings U7 and U8, the shear stress shows a different tendency (i.e. decreases near the edge and then increases at the edge) on the compression edge compared to Bearings U1 to U6.

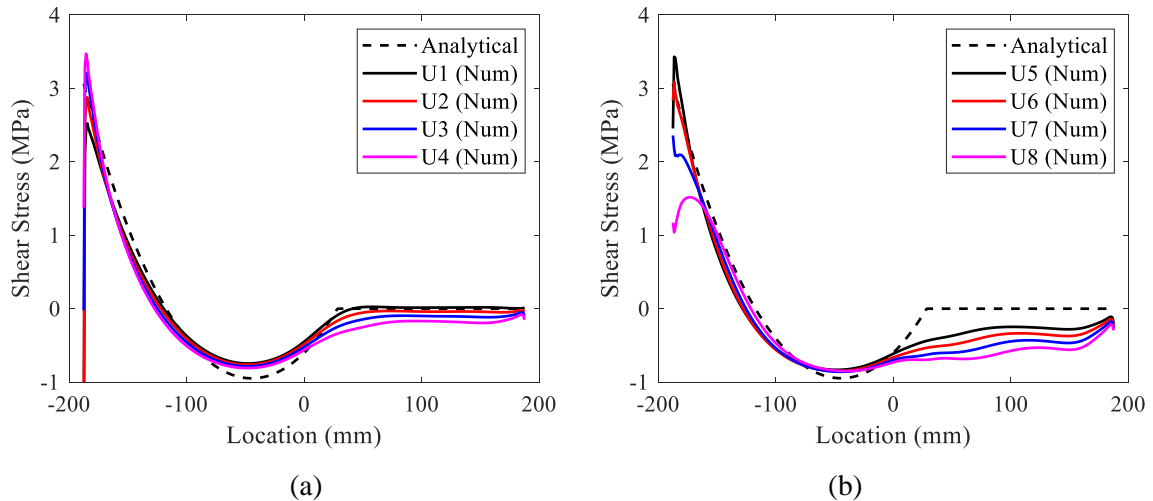


Figure 5-18 Shear stress distribution when rotation per layer is 0.01 radians for (a) Bearings U1 to U4; (b) Bearings U5 to U8.

The shear stress distributions for the condition that the applied rotation equals to the maximum rotation (based on CSA S6-14) listed in Table 4-3 are shown in Figure 5-19. The agreement between the numerical curves and the analytical one is better than those shown in Figure 5-18, because the global effects, as shown in Figure 5-20, are not as prevalent as the case when the rotation per layer is 0.01 radians (Figure B 4 in Appendix B includes the deformed shape of Bearings U1 to U8 when the normalized rotation is 3.38).

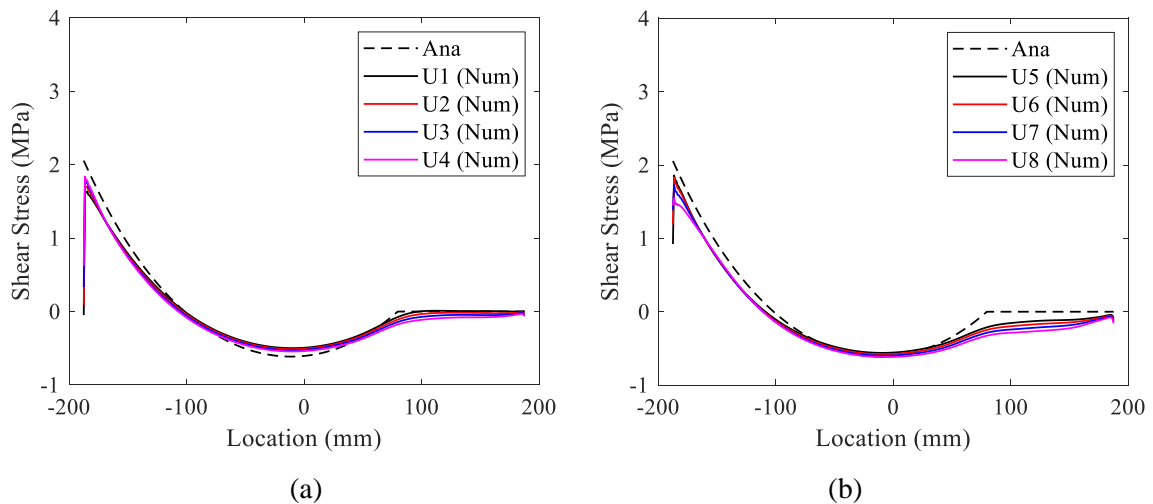


Figure 5-19 Shear stress distribution when rotation is the maximum permitted from CSA S6-14 for (a) Bearings U1 to U4; (b) Bearings U5 to U8.

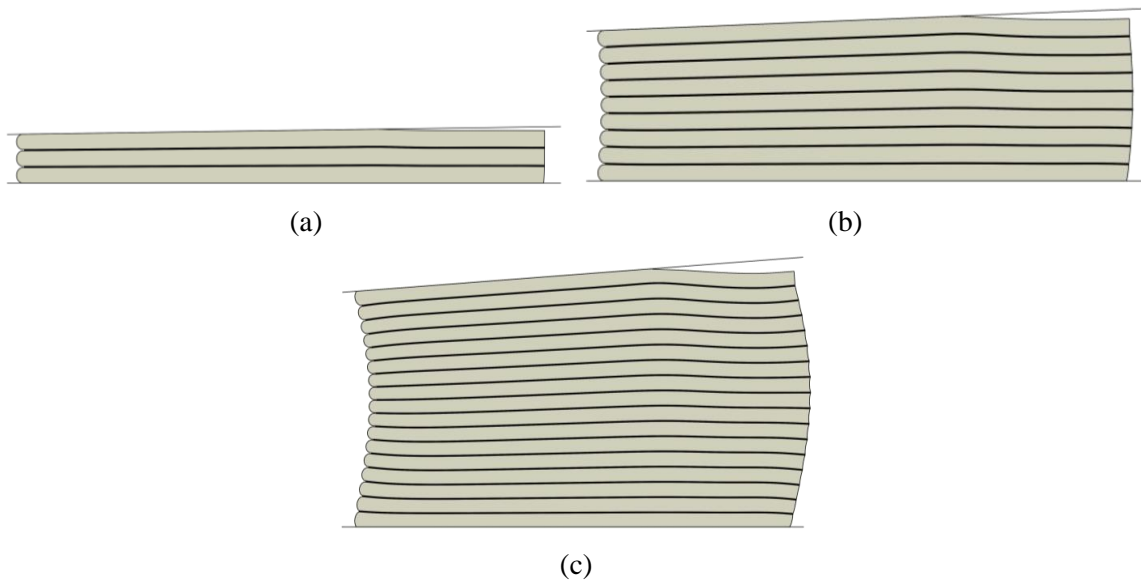


Figure 5-20 Deformed shape of Bearing (a) U1; (b) U4; (c) U8 when the normalized rotation is 3.38.

At the compressive edge, the numerical curves are not smooth, which is caused by numerical errors. The magnitude of the numerical maximum shear stress is determined by 3rd order extrapolation from the data in the nearby stable range. The shear stress distributions (when the normalized rotation equals to 3.38) after extrapolation are shown in Figure 5-21. The shear stress distributions when the rotation per layer is 0.01 radians are shown in Figure F 1.

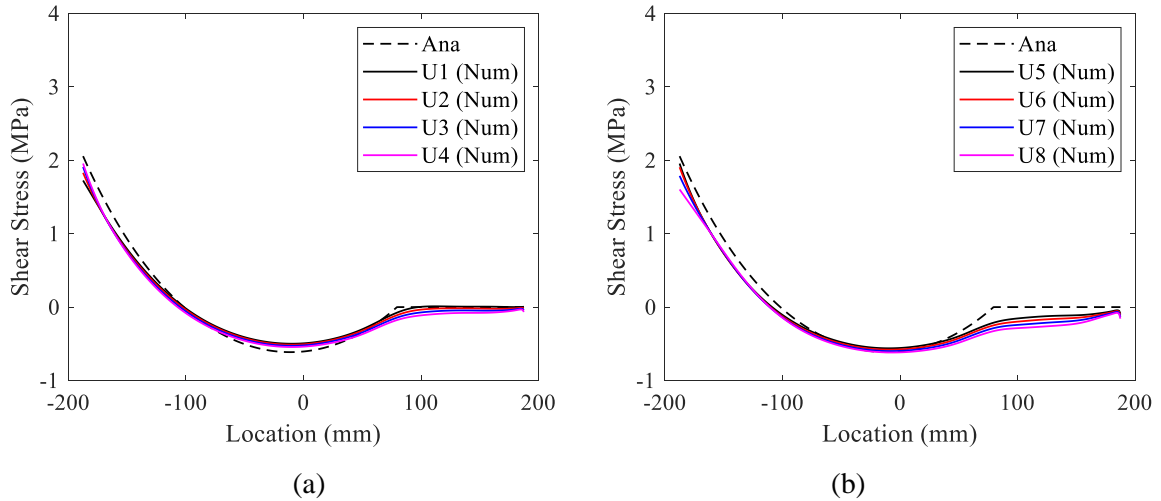


Figure 5-21 Shear stress distribution when the normalized rotation equals to 3.38 after extrapolation for (a) Bearings U1 to U4; (b) Bearings U5 to U8.

The curves become smoother at the compressive edge. The magnitudes of the numerical maximum shear stresses under the two levels of rotation after extrapolation and the corresponding errors compared with the analytical solution are shown in Table 5-4 and Table 5-5, respectively. The overall absolute error under a lower rotation is smaller. The amplitude of the numerical maximum shear stress becomes larger as the number of layers increases from 3 to 9, and then it becomes smaller as the number of layers increases from 11 to 17. The error for Bearing U8 under the 0.01-rotation per layer is -50.4%, which is large, and this also indicates that the analytical solutions cannot predict the maximum shear stress accurately at the rotation levels considered, especially for bearings with large number of layers.

It seems that there are at least two factors that could control the value of the maximum shear stress. As the number of layers increases, one of the factors becomes predominant and changes the

tendency of the maximum shear stress. It is hard to detect what are those factors from the current results, and this could be an interesting direction for future studies. Also, at the compressive edge, the trend of the shear stress distribution are different for bearings with different number of layers. Since the analytical solution is based on one elastomeric pad, it cannot reflect such difference.

Table 5-4 Numerical maximum shear stresses under the 0.01-radian rotation per layer after extrapolation and the corresponding error with respect to the analytical solutions.

Bearing	U1	U2	U3	U4	U5	U6	U7	U8
Numerical maximum shear stress (MPa)	2.68	3.16	3.57	3.80	3.65	3.08	2.16	1.15
Error (%)	-26.6	-13.4	-2.2	3.9	0.0	-15.7	-41.0	-50.4

Table 5-5 Numerical maximum shear stresses under the maximum rotation based on CSA S6-14 after extrapolation and the corresponding error with respect to the analytical solutions.

Bearing	U1	U2	U3	U4	U5	U6	U7	U8
Numerical maximum shear stress (MPa)	1.724	1.829	1.909	1.956	1.955	1.905	1.787	1.603
Error (%)	-16.1	-11.0	-7.1	-4.9	-4.9	-7.3	-13.0	-22.0

5.3.1.4 Normal Stress Distribution

The comparison between the analytical and the numerical normal stress distribution after the occurrence of lift-off is also considered. Note that theoretically, as given by Eq. (3.15), the normal stress distribution is not a function of z . But due to some global effects, this is not strictly true in the FEA results, as shown in Figure 5-4. For comparison, the normal stress distribution along the top surface and along the middle path of the second elastomeric layer when the normalized rotation equals to 3.38 are shown in Figure 5-22 and Figure 5-23, respectively. The numerical curves approximately overlap with each other and the error between the numerical and the analytical maximum normal stress is listed in Table 5-6.

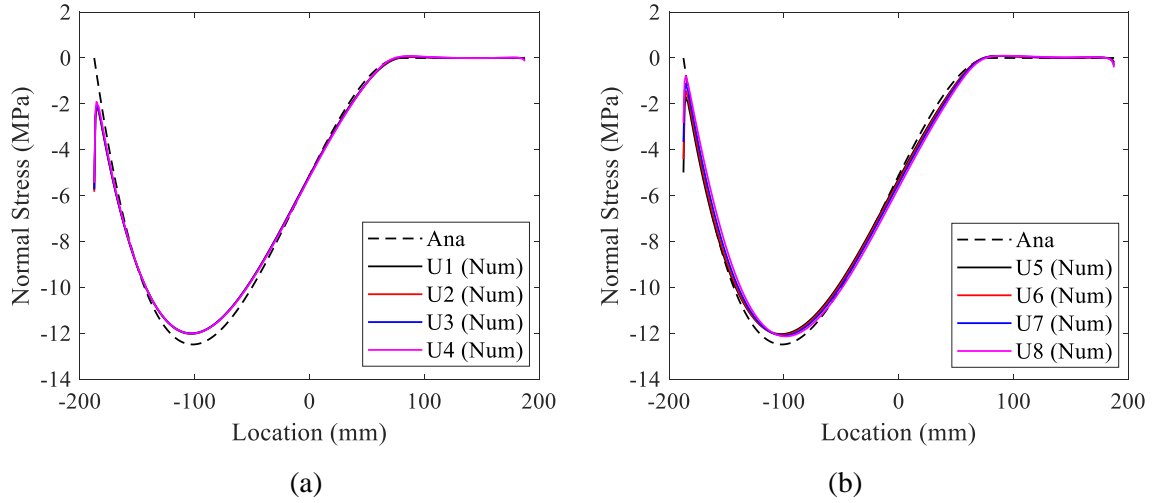


Figure 5-22 Normal stress distribution along the top of the second elastomeric layer when rotation is the maximum from CSA S6-14 for (a) Bearings U1 to U4; (b) Bearings U5 to U8.

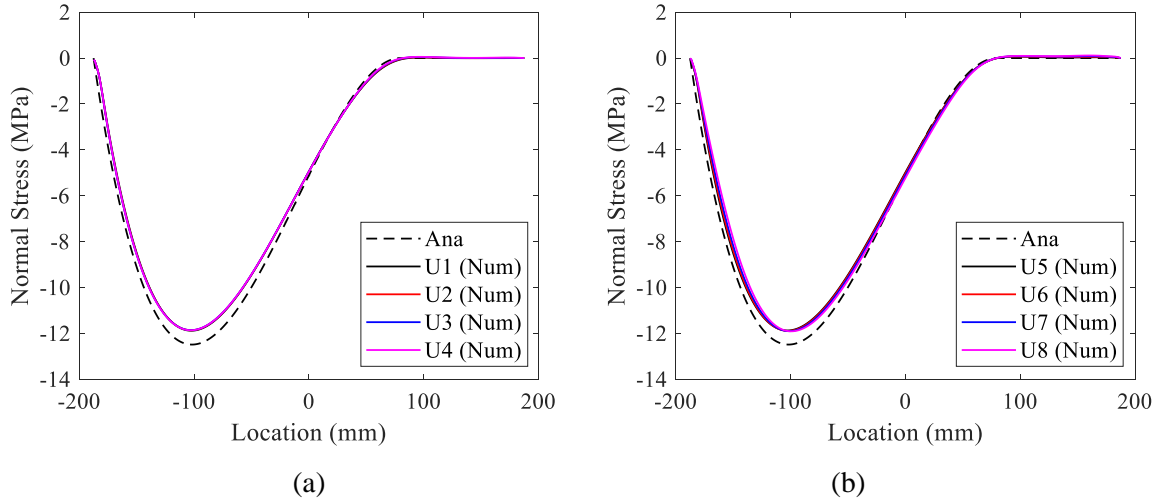


Figure 5-23 Normal stress distribution along the middle of the second elastomeric layer when rotation is the maximum from CSA S6-14 for (a) Bearings U1 to U4; (b) Bearings U5 to U8.

Table 5-6 Error between numerical and analytical maximum normal stress

Bearing	U1	U2	U3	U4	U5	U6	U7	U8
Error along top (%)	-4.47	-4.63	-4.65	-4.56	-4.38	-4.12	-3.85	-3.60
Error along middle (%)	-5.59	-5.75	-5.79	-5.75	-5.67	-5.53	-5.43	-5.38

5.3.1.5 Shear Strain Distribution

Figure 5-24 shows the shear strain distributions when the rotation per layer is 0.01 radians (the extrapolated ones are shown in Figure F 2), and Figure 5-25 shows the ones when the normalized rotation equals to 3.38 (the extrapolated ones are shown in Figure F 3). The errors of the numerical maximum shear strain after extrapolation and the analytical results for all the eight bearings under the two rotation conditions (0.01 radians per layer and $\theta/\theta_0 = 3.38$) are shown in Table 5-7. The absolute errors are smaller when the rotation is smaller ($\theta/\theta_0 = 3.38$).

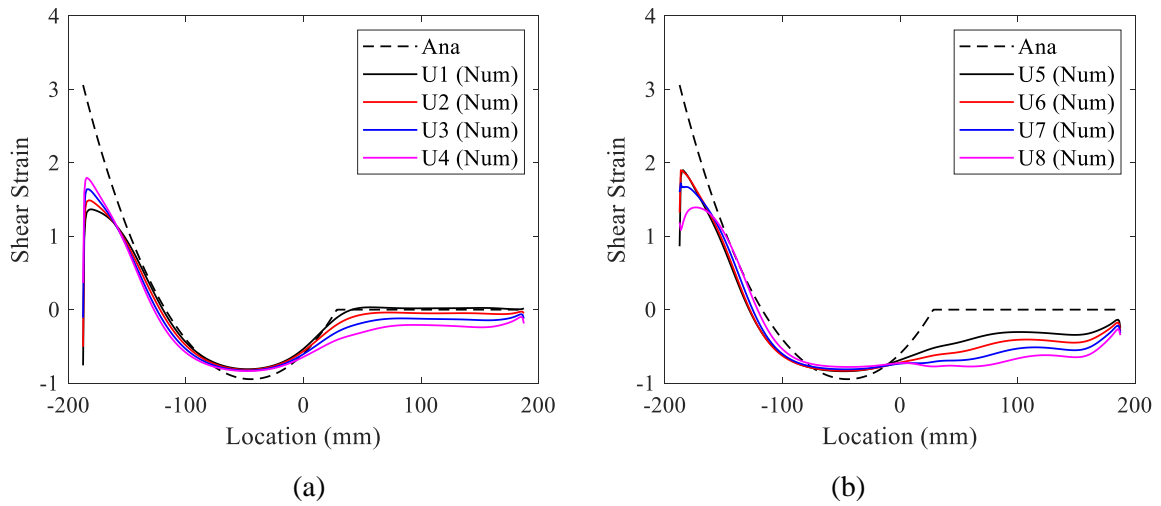


Figure 5-24 Shear strain distribution when rotation per layer is 0.01 radians for (a) Bearings U1 to U4; (b) Bearings U5 to U8.

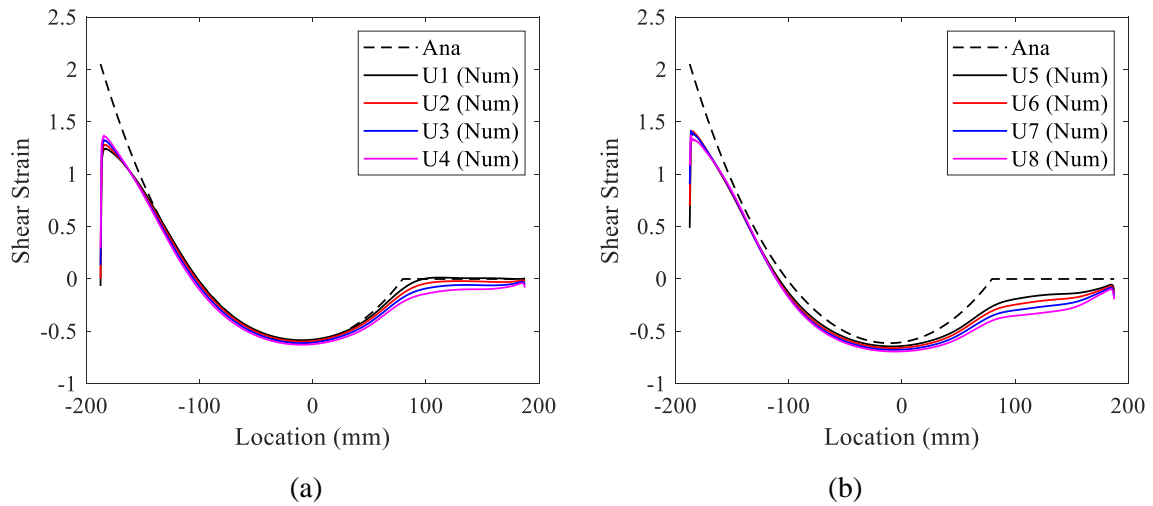


Figure 5-25 Shear strain distribution when rotation is the maximum from CSA S6-14 for (a) Bearings U1 to U4; (b) Bearings U5 to U8.

Table 5-7 Errors of the numerical maximum shear strain after extrapolation and the analytical results for Bearing U1 to U8 under two levels of rotation.

Bearing	U1	U2	U3	U4	U5	U6	U7	U8
Error of the Max. shear strain when rotation per layer is 0.01 radians (%)	-56	-51	-44	-38	-35	-37	-46	-64
Error of the Max. shear strain when normalized rotation is 3.38 (%)	-38	-35	-32	-30	-28	-28	-29	-32

The numerical curves do not fit well with the analytical curve at the compressive edge. Compared to Figure 5-19, when under the maximum rotation based on CSA S6-14, the error of the maximum shear strain with respect to the analytical solution is larger than the maximum shear stress. From the pressure solution, the shear stress and the normal stress have the relationship of

$$\frac{\partial \tau}{\partial z} = \frac{\partial p}{\partial x} \quad (5.2)$$

Therefore, the shear stress distribution along the top surface of elastomeric layer is

$$\tau = \frac{\partial p}{\partial x} \frac{t}{2} \quad (5.3)$$

From Eq. (5.3), the shear strain could be further derived as

$$\gamma = \frac{\partial p}{\partial x} \frac{t}{2G} \quad (5.4)$$

Compared with the expression of shear stress in Eq. (5.3), G is added to the denominator in the expression of shear strain in Eq. (5.4). For the analytical solution, G is simply selected as 1.0 MPa. But during the simulation, G varies with the stress level. Therefore, it is the nonlinearity of G that results in the significant divergence between the numerical and the analytical shear strain distribution, especially in the region close to the compressive edge where the stress level is relatively high.

5.3.2 Effect of the Shape Factor

5.3.2.1 Effective Part of the Bearings

When the applied rotations were to make the analytical $\eta = 0.7$, the numerical η and the error with respect to the analytical η are shown in Table 5-8. As the shape factor decreases, the numerical η becomes smaller, which means the effective part decreases. The deformed shape for Bearings H1 to H6 under the rotations that make the analytical $\eta = 0.7$ are shown in Figure B 5.

Table 5-8 Numerical η for Bearing H1 to H6 and the corresponding error with respect to the analytical η .

Bearing	S	Numerical η	Error between numerical and analytical η (%)
H1	31.25	0.692	-1.1
H2	26.04	0.691	-1.3
H3	22.92	0.689	-1.6
H4	19.54	0.684	-2.3
H5	15.63	0.671	-4.1
H6	11.17	0.650	-7.1

5.3.2.2 Moment-Rotation Relationship

The moment-rotation relationship for Bearings H1 to H6 up to the rotation that makes the analytical $\eta = 0.7$ are shown in Figure D 1. The moment-rotation relationship for Bearings H1 to H6 up to the maximum rotation based on CSA S6-14 are shown in Figure D 2. The error between the analytical and the numerical results of the reaction moment when Bearings H1 to H6 are under two levels of rotation are shown in Table 5-9. Under the two levels of rotation, as the shape factor decreases, the error between the numerical and the analytical results of the reaction moment increases from negative value to positive value, which means the bearing becomes stiffer. As shown in Figure D 2, the numerical curves for Bearings H1 to H6 all cross over with the analytical curve, but the magnitude of rotation when the two curves intersect are different for different bearings.

Table 5-9 Error between the numerical and the analytical results of the reaction moment when Bearings H1 to H6 are under two levels of rotation.

Bearing	H1	H2	H3	H4	H5	H6
Error when under the rotation that makes the analytical $\eta = 0.7$ (%)	-1.50	-1.52	-1.33	-0.76	0.70	4.10
Error when under the maximum rotation based on CSA S6-14 (%)	-0.09	-0.10	-0.04	0.11	0.47	1.89

5.3.2.3 Shear Stress and Normal Stress Distribution

The shear stress distribution along the top surface of the second elastomeric layer for Bearings H1 to H6 under the rotation that makes the analytical $\eta = 0.7$ and under the maximum rotation based on CSA S6-14 are shown in Figure D 3 and Figure D 4, respectively (the plots after extrapolation are shown in Figure F 4 and Figure F 5, respectively). The shear stress distribution for Bearings H1 and H6 under the maximum rotation based on CSA S6-14 are shown in Figure 5-25.

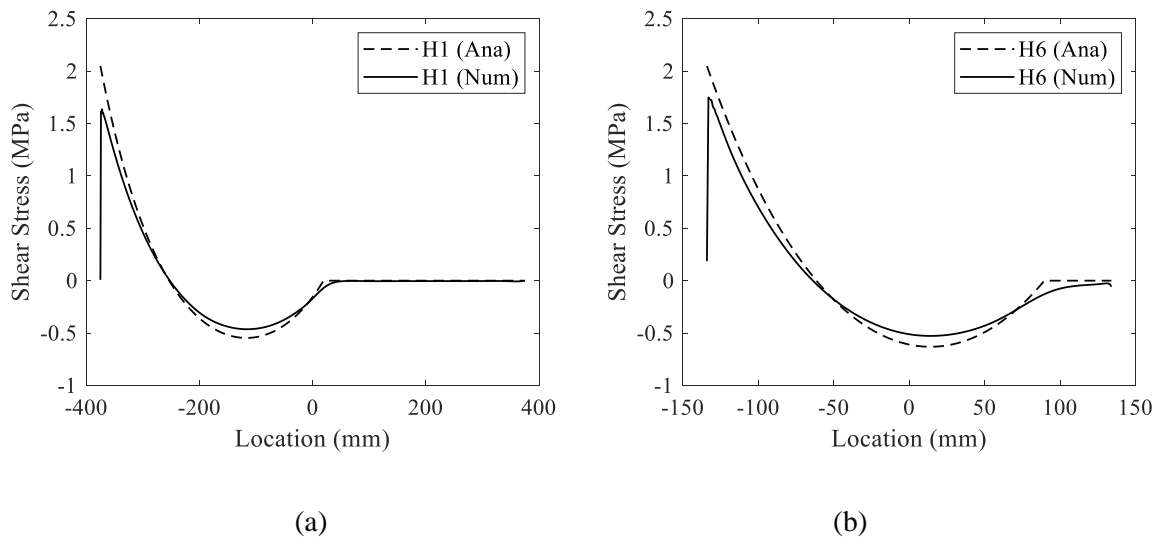


Figure 5-26 Shear stress distribution when rotation is the maximum from CSA S6-14 for Bearing (a) H1; (b) H6.

The error between the extrapolated numerical and the analytical results of the maximum shear stress under these two levels of rotation are shown in Table 5-10. As the shape factor decreases, the

absolute error between the numerical and the analytical results of the maximum shear stress decreases, which means the numerical results are closer to the analytical solution.

Table 5-10 Error between the extrapolated numerical and the analytical results of the maximum shear stress when Bearings H1 to H6 are under two levels of rotation.

Bearing	H1	H2	H3	H4	H5	H6
Error when under the rotation that makes the analytical $\eta = 0.7$ (%)	-18.77	-18.35	-17.35	-15.64	-11.32	4.20
Error when under the maximum rotation based on CSA S6-14 (%)	-16.71	-15.26	-15.05	-13.46	-11.91	-8.82

The normal stress distributions along the middle path of the second elastomeric layer for Bearings H1 to H6 under the rotation that makes the analytical $\eta = 0.7$ and under the maximum rotation based on CSA S6-14 are shown in Figure D 5 and Figure D 6, respectively. The error between the numerical and the analytical results of the maximum normal stress under these two levels of rotation are shown in Table 5-11. As the shape factor decreases, the error between the numerical and the analytical results of the maximum shear stress increases, which means the numerical results increasingly deviated from the analytical solutions.

Table 5-11 Errors between the numerical and the analytical results of the maximum normal stress when Bearings H1 to H6 are under two levels of rotation.

Bearing	H1	H2	H3	H4	H5	H6
Error when under the rotation that makes the analytical $\eta = 0.7$ (%)	-2.37	-2.94	-3.25	-3.57	-3.83	-3.77
Error when under the maximum rotation based on CSA S6-14 (%)	-3.49	-3.90	-4.18	-4.37	-4.99	-5.59

5.3.3 Effect of the Compressibility and Extensibility Index, λ

The analytical curves in this section are included as references. Since the purpose of this section is to compare the numerical results of bearings with different material properties and geometry but same value of λ , it is acceptable if the numerical curves do not fit well with the analytical curve.

5.3.3.1 Effective Part of the Bearings

According to Eq. (2.76) and Eq. (2.54), we have

$$\frac{\lambda^2 \sigma_c}{12\theta G S^3} = \eta^2 \left(\coth \eta \lambda - \frac{1}{\eta \lambda} \right)^2 \quad (5.5)$$

Since G , θ , S , σ_c , and λ are all the same for Bearings L1 to L4, the analytical η is the same. The analytical and the numerical results of η for Bearings L1 to L4 as well as the corresponding errors are shown in Table 5-12. The numerical values of η were determined visually from the deformed shape of the bearings, therefore, the accuracy also depends on the mesh and rotation increment. The numerical η are very closed to each other and the error with respect to the analytical η is approximately -3.8%. The coefficient of variation (CoV) of the four numerical η shown in Table 5-12 is 0.26%, which is small and indicates the four results are close to each other.

The deformed shape of Bearings L1 to L4 under the combination of compression (5 MPa) and rotation (0.02 radians) are shown in Figure 5-27. Visually, the deformation of the elastomeric layers are similar for different bearings.

Table 5-12 Analytical and the numerical results of η for Bearings L1 to L4 as well as the corresponding errors.

Bearing	Analytical η	Numerical η	Error (%)
L1	0.7356	0.7112	-3.31
L2	0.7356	0.7068	-3.92
L3	0.7356	0.7065	-3.96
L4	0.7356	0.7080	-3.75

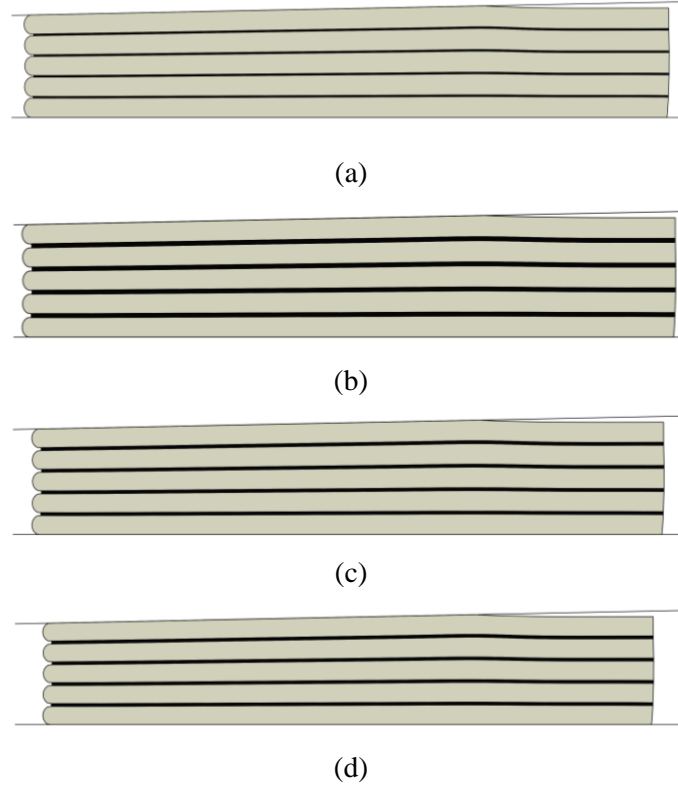


Figure 5-27 Deformed shape of Bearings L1 to L4 under the combination of compression (5MPa) and rotation (0.02 radians)

5.3.3.2 *Moment-Rotation Relationship*

The moment-rotation relationship for Bearings L1 to L4 up to a 0.02-radian rotation are shown in Figure E 1. The normalized moment-rotation relationship is shown in Figure 5-28, the normalized analytical curves of these four bearings overlap with each other, which verifies that by changing the material property and geometry but keeping λ (also S and G) constant, the lift-off behaviour of different bearings are the same. The error between the numerical and the analytical results of the reaction moment when rotation equals to 0.02 radians are shown in Table 5-13. the CoV value of the normalized moment when the four bearings are under a 0.02-radian rotation is 0.32%, which is small and indicates the four results are close to each other.

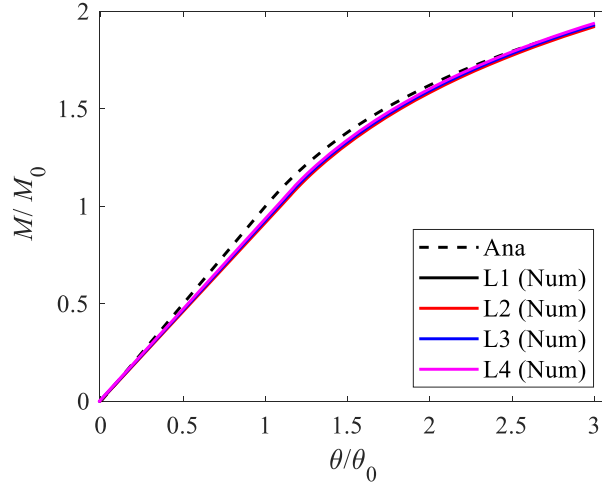


Figure 5-28 Normalized moment as a function of normalized rotation for Bearings L1 to L4.

Table 5-13 Error between the numerical and the analytical results of the reaction moment when rotation equals to 0.02 radians.

Bearing	L1	L2	L3	L4
Error (%)	0.07	-0.35	0.11	0.54

5.3.3.3 Shear Stress and Normal Stress Distribution

The shear stress distribution along the top surface of the second elastomeric layer and the normal stress distribution along the middle path of the second elastomeric layer for Bearings L1 to L4 under the 0.02-radian rotation are shown in Figure E 2 and Figure E 3, respectively. The analytical and numerical shear stress and normal stress distribution as a function of x/b for Bearings L1 to L4 are shown in Figure 5-29 and Figure 5-30, respectively (the extrapolated numerical shear stress distribution are shown in Figure F 6). The error between the numerical and the analytical results of the maximum shear stress (extrapolated) and normal stress when Bearings L1 to L4 are under 0.02-radian rotation are shown in Table 5-14. Regardless of the deviation from the analytical solution, the errors for Bearings L1 to L4 are very close to each other, which confirms that the bearings with the same λ value have the same behaviour. Therefore, λ is an important parameter that should be considered during design. Since keeping the same λ but varying the material properties or bearing

geometry would result in the same bearing behaviour, more design choices of bearings are available.

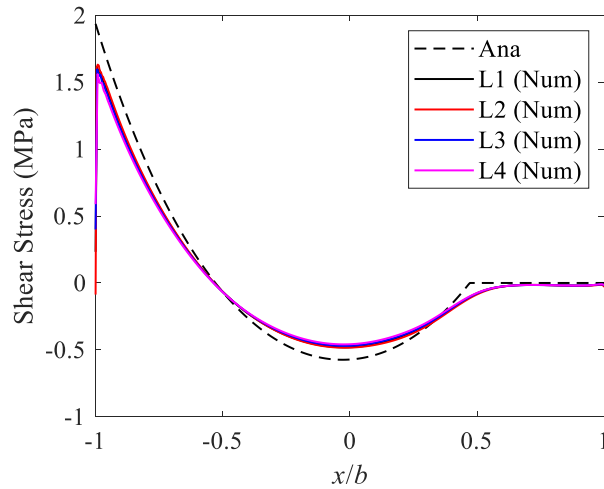


Figure 5-29 Analytical and numerical shear stress distribution as a function of x/b for Bearings L1 to L4.

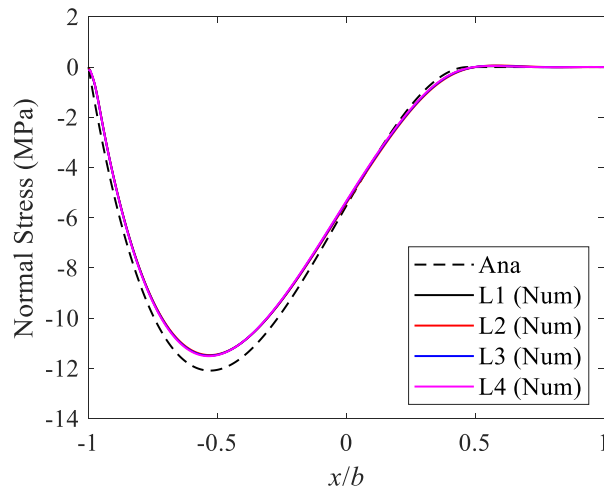


Figure 5-30 Analytical and numerical normal stress distribution as a function of x/b for Bearings L1 to L4.

Table 5-14 Error between the numerical and the analytical results of the maximum shear stress (extrapolated) and normal stress when rotation equals to 0.02 radians.

Bearing	L1	L2	L3	L4
Error of max. shear stress (%)	-12.95	-11.17	-13.51	-15.70
Error of max. normal stress (%)	-4.92	-5.12	-4.93	-4.76

Chapter 6 Conclusions and Recommendations

6.1 Conclusions

Although SREBs are currently widely used around the world, interest in FREBs is growing and may prove to be a popular solution in the future, especially in developing countries. This is because FREBs have been shown to have similar performance as SREBs, and they are potentially lighter, cheaper and easier to manufacture. For unbonded FREBs, lift-off could occur under certain combinations of large rotations and relatively low axial stress. This causes the superstructure to partially lose contact with the bearing and thus decreases the effective part of the bearing. Furthermore, some nonlinearities are developed during this process which renders the problem to be more complex than the bonded cases. The lack of inclusion of FREBs in the current bridge design codes and other standards impede the pace of their popularization. The differences between FREBs and the SREBs in the analytical model is that for the former one, the fiber reinforcement is flexible and extensible; however, in the latter one, the reinforcement is considered rigid.

This research shows the existing analytical solutions based on the pressure solution describing the compression behaviour (force-displacement relationship and the compressive modulus), the bending behaviour (moment-rotation relationship and bending modulus), as well as the stress distribution (shear stress and normal stress) when an infinite strip B-FREB is under pure compression and pure rotation loading conditions. The analytical solution of the lift-off initiation rotation and the moment-rotation relationship (Van Engelen, 2019) for infinite strip U-FREBs under the combination of compression and rotation, which account for the geometric non-linearity of lift-off, were shown. The shear stress, the normal stress, and the shear strain distributions along the width of U-FREBs after lift-off occurs were derived.

Five finite element models of B-FREBs with a different number of layers were developed and used to simulate pure compression (up to 5 MPa) and pure rotation (up to 0.01 radians) cases, with the simulation results being compared with the analytical solutions. For validation of the U-FREBs behaviour, eight bearings with different number of layers were modelled subjected to the combination of 5 MPa compression and two levels of rotation (which makes the rotation per layer equals to 0.01 radians, and the maximum rotation permitted based on CSA S6-14). Bearings with different shape factor values were evaluated under the combination of 5 MPa compression and two levels of rotation (which makes the analytical $\eta = 0.7$, and the maximum rotation based on CSA S6-14). Four bearings with different material properties and geometry but the same λ values were evaluated under the same loading condition (i.e. the combination of 5 MPa compression and a 0.02-radian rotation). Based on the obtained results, the following conclusions can be made.

1. The analytical solutions fit well with the numerical results in terms of the overall tendency for both B-FREBs and U-FREBs, but how well they can match depends on the value of G used in the analytical expressions. For example, the numerical results of the bending modulus of B-FREBs have around 17% error compared with the analytical solutions based on a 1.0 MPa shear modulus, but the error reduces to around 2.5% when compared with the analytical solutions based on a 0.8 MPa shear modulus.
2. For U-FREBs, the overall trend is that as the number of layers increases, and as the applied rotation increases, the global effects, represented by the deformation, become more obvious. Thus, the numerical results of the reaction moment deviate more from the analytical solutions (this can be seen in Figure 5-17). The differences of the assumptions for the analytical model and the numerical model, which are the material property and the boundary condition, account for the deviation between the numerical and the analytical results. When the rotation increases to a certain level, the reinforcement layers will warp, which also deviates the numerical results from the analytical solutions.

3. The analytical results of the maximum shear stress and strain, when considered, were found to be conservative at the maximum rotation based on CSA S6-14, when $G = 1.0$ MPa is substituted into the analytical solution. The accuracy of the analytical maximum shear stress and strain could be further improved, although in absence of alternatives, the analytical solution provides a conservative approximation.
4. The analytical solution of the shear stress and the shear strain distribution is not accurate in the unloaded part (which assumes no stress is developed) under very large global rotations, the numerical results show that some stresses developed in the unloaded part; although, these tend to be small compared to the maximum value on the compression edge.
5. When under the rotation that makes the analytical $\eta = 0.7$, bearings with smaller shape factors give a smaller numerical η , which means the effective part of the bearing decreases.
6. When under the two rotation levels which either makes the analytical $\eta = 0.7$, or the maximum rotation based on CSA S6-14, bearings with a smaller shape factor (S varies from 31.25 to 11.17)
 - a. Show a relatively larger reaction moment compared to the analytical solution. As S decreases, the error increases from 1.50% to 4.10% when at the rotation that makes the analytical $\eta = 0.7$; the error increases from -0.09% to 1.89% when at the maximum rotation based on CSA S6-14;
 - b. Show a relatively larger maximum shear stress compared to the analytical solution. As S decreases, the magnitude of the error decreases from -18.7% to -3.92% when under the rotation that makes the analytical $\eta = 0.7$; the absolute value of the error decreases from 20.17% to 14.63% when under the maximum rotation based on CSA S6-14; and,

- c. show a relatively smaller maximum normal stress compared to the analytical solution. As S decreases, the magnitude of the error decreases from 18.7% to 3.92% when under the rotation that makes the analytical $\eta = 0.7$; the error decreases from 20.17% to 14.63% when under the maximum rotation based on CSA S6-14.
7. The lift-off behaviour (effective part, the moment-rotation relationship, shear stress distribution, and the normal stress distribution) of bearings with the same value of the compressibility and extensibility index λ are approximately the same, which indicates that λ is a controlling parameter that should be considered during the design. By keeping the same λ but varying the material properties or bearing geometry, more design choices of bearings are available.
8. There was a contradiction between the provisions in CSA S6-19 and AASHTO (2017) about the lift-off behaviour, where the former prevents its occurrence whereas the latter allows it. It is important to provide a consistent guideline. Based on the results presented herein, lift-off could be allowed to occur, provided the amplitude of the rotation be controlled to prevent the shear failure of the bearings. Since in reality the bearings are subjected to the combination of shear, rotation, and compression, the proper magnitude of these three types of load should be considered in design according to the real condition. Based on the loading conditions, the material properties and the geometry of the bearings could be determined such that lift-off could occur but the maximum shear strain would be below the level that may cause shear failure.

6.2 Recommendations

1. Overall, the analytical solutions can predict the behaviour of U-FREBs, and the form is simple and thus convenient to use. For a better fitting of the analytical solutions with the numerical results, the following recommendations are made:
 - a. Make finer mesh at the bearing edge to obtain more reasonable numerical results of maximum shear stress and shear strain.
 - b. In the analytical model, consider different boundary conditions for the top and the bottom layers (embedded between a rigid wire and an extensible reinforcement layer), as well as the intermediate layers (embedded between two extensible reinforcement layers).
 - c. Consider the nonlinearity of G in the analytical model. Because the stress level of the elastomer varies within the bearing, in this case, G is a function of both the location and the applied load which makes selecting an appropriate value difficult.
 - d. Consider warping behaviour of the reinforcement in the analytical model.
 - e. Consider global effects in the analytical model when the rotation is large.
2. In reality, bridge bearings are subjected to the combination of compression, rotation, and shear. In this research, only the first two loading conditions are considered. Therefore, future research can be conducted on the behaviour of the bearing under the combination of these three types of load. Also, if the bearing is slender and under large loads, it is necessary to address the stability issue.
3. Based on the paths considered, as the number of layers increases from 3 to 9, the numerical results of the maximum shear stress become larger, and as the number of layers increases from 11 to 17, the numerical results of the maximum shear stress become smaller. It seems

that there are at least two factors that could control the value of the maximum shear stress. It is hard to detect what are those factors from the current results, and this could be an interesting direction for future studies.

4. This research focused on bearings with an infinite-strip shape. Further studies on the lift-off behaviour could be conducted based on rectangular, circular and annular shaped bearings.

References

- AASHTO. (2010). *AASHTO LRFD Bridge Design Specifications*, 8th Ed., Washington, DC
- AASHTO. (2017). *AASHTO LRFD Bridge Design Specifications*, 5th Ed., Washington, DC
- Al-Anany, Y. M., & Tait, M. J. (2015). A numerical study on the compressive and rotational behavior of fiber reinforced elastomeric isolators (FREI). *Composite Structures*, 133, 1249–1266. <https://doi.org/10.1016/j.compstruct.2015.07.042>
- Angeles Contractor Inc. (2019). *Foothill Law & Justice Center*. Retrieved from <http://angelescontractor.com/portfolio-item/foothill-law-justice-center/>
- Ausenco. (2017). Lord Strathcona Elementary School Seismic Upgrade. Retrieved from <https://www.ausenco.com/en/strathcona-seismic-upgrade2>
- Belivanis, K. V. (2017). *Expanding the Use of Elastomeric Bearings for Higher Demand Applications*. The University of Texas at Austin.
- BS (British Standard) EN 15129. (2018). Anti-seismic devices. London
- Buckle, I. G. (2000). Passive control of structures for seismic loads. *Bulletin of the New Zealand Society for Earthquake Engineering*, 33(3), 209–221.
- Chopra, A. K. (2012). Dynamics of structures: Theory and applications to earthquake engineering. In *Sociological Methods & Research* (Fourth Edi). Berkeley.
- Constantinou, M. C., Kalpakidis, I., Filiatrault, A., & Lay, R. A. E. (2011). *LRFD-Based Analysis and Design Procedures for Bridge Bearings and Seismic Isolators*.
- CSA (Canadian Standards Association). (2014). "S6-14 Canadian highway bridge design code." Mississauga, ON, Canada.
- CSA (Canadian Standards Association). (2019). "S6-19 Canadian highway bridge design code." Mississauga, ON, Canada.
- Das, A., & Dutta, A. (2012). Modeling of Fiber-Reinforced Elastomeric Base Isolators. *15th World Conference on Earthquake Engineering (15WCEE)*.
- Derham, C. J., Kelly, J. M., & Thomas, A. G. (1985). Nonlinear natural rubber bearings for seismic isolation. *Nuclear Engineering and Design*, 84(3), 417–428. [https://doi.org/10.1016/0029-5493\(85\)90258-4](https://doi.org/10.1016/0029-5493(85)90258-4)
- D.S. Brown. (2019). Seismic Isolation Bearing Assemblies. Retrieved from <https://www.dsbrown.com/bridges/structural-bearing-assemblies/seismic-isolation-bearing/>
- EPS. (2019). Triple Pendulum Isolator. Retrieved May 31, 2019, from <https://www.earthquakeprotection.com/triple-pendulum>
- Expedia. (2019). *Los Angeles City Hall Pictures: View Photos & Images of Los Angeles City Hall*. Retrieved from <https://www.expedia.com/pictures/los-angeles-county/los-angeles/los-angeles-city-hall.d6069627/>
- Girish, M., & Pranesh, M. (2015). Sliding Isolation Systems : State-of-the-Art Review. *IOSR Journal of Mechanical and Civil Engineering*, 12(4), 30–35.
- Hamakareem Izat, M. (2017). Bridge Bearings -Types of Bearings for Bridge Structures and Details. Retrieved from <https://theconstructor.org/structures/bridge-bearings-types-details/18062/>

- Hengshui Jingtong Rubber Co. (n.d.). Steel Disc Bridge Bearing Designs & Types. Retrieved March 30, 2020, from <https://www.bridgebearings.org/product/disc-bridge-bearing.html>
- ISO (International Organization for Standardization). 22762-3 (2018). "Elastomeric seismic-protection isolators Part 3: Application for buildings-specifications." 3rd Ed., Switzerland.
- Kelly, J. M., M., & Konstantinidis, D. (2009). Effect of Friction on Unbonded Elastomeric Bearings. *Journal of Engineering Mechanics*, 953–960. <https://doi.org/10.1061/ASCEEM.1943-7889.0000019>
- Kelly, J. M., & Calabrese, A. (2013). Analysis of fiber-reinforced elastomeric isolators including stretching of reinforcement and compressibility of elastomer. *Ingegneria Sismica*, 30(3), 5–16.
- Kelly, J. M., & Konstantinidis, D. A. (2011). Mechanics of Rubber Bearings for Seismic and Vibration Isolation. In *A John Wiley & Sons, Ltd.*
- Kelly, J. M., & Takhirov, S. M. (2001). *Analytical and Experimental Study of Fiber-Reinforced Elastomeric Isolators Fiber-Reinforced Elastomeric Isolators*. Berkeley.
- Kelly, J. M., & Takhirov, S. M. (2002). Analytical and Experimental Study of Fiber-Reinforced Strip Isolators. *Report No. PEER 2002/11*, Pacific Earthquake Engineering Research Center, University of California, Berkeley, CA.
- MATLAB. (2018). *version (R2018b)*. Natick, Massachusetts: The MathWorks Inc.
- Moeindarbari, H., & Taghikhany, T. (2012). Optimum Design of Triple Friction Pendulum Bearing Subjected by Near-Field Ground Motions. *15th World Conference on Earthquake Engineering (15WCEE)*.
- Naaseh. (1995). Seismic Retrofit of San Francisco City Hall: the Role of Masonry and Concrete. *The 3rd National Concrete & Masonry Eng. Conf.*, 769–795. San Francisco, California.
- Naeim, F., & Kelly, J. M. (1999). Design of Seismic Isolated Structures: From Theory to Practice. In *John Wiley & Sons* (Vol. 16). <https://doi.org/10.1193/1.1586135>
- Oladimeji, F. A. (2012). *Bridge Bearings: Merits, Demerits, Practical Issues, Maintenance and Extensive Surveys on Bridge Bearings*. Royal Institute of Technology, Stockholm, Sweden.
- Pinarbasi, S., Akyuz, U., & Mengi, Y. (2006). A new formulation for the analysis of elastic layers bonded to rigid surfaces. *International Journal of Solids and Structures*, 43(14–15), 4271–4296. <https://doi.org/10.1016/j.ijsolstr.2005.06.047>
- Pinarbasi, S., & Mengi, Y. (2008). Elastic layers bonded to flexible reinforcements. *International Journal of Solids and Structures*, 45(3–4), 794–820. <https://doi.org/10.1016/j.ijsolstr.2007.08.029>
- Saito, T. (2015). Behaviour of response controlled and seismic isolated buildings during severe earthquake in Japan. *Energia, Ambiente e Innovazione*, 5:31–37. <https://doi.org/10.12910/EAI2015-078>
- Spizzuoco, M., Calabrese, A., & Serino, G. (2014). Innovative low-cost recycled rubber-fiber reinforced isolator: Experimental tests and Finite Element Analyses. *Engineering Structures*, 76, 99–111. <https://doi.org/10.1016/j.engstruct.2014.07.001>
- Stanton, J. F., & Roeder, C. W. (2008). Rotation Limits for Elastomeric Bearings. In *Rotation Limits for Elastomeric Bearings*. <https://doi.org/10.17226/23131>
- Toopchi-Nezhad, H., Tait, M. J., & Drysdale, R. G. (2011). Bonded versus unbonded strip fiber reinforced elastomeric isolators: Finite element analysis. *Composite Structures*, 93(2), 850–

859. <https://doi.org/10.1016/j.compstruct.2010.07.009>

- Tsai, H.-C., & Kelly, J. M. (2001). Stiffness Analysis of Fiber-Reinforced Elastomeric Isolators. *Report No. PEER 2001/05*, Pacific Earthquake Engineering Research Center, University of California, Berkeley, CA.
- Van Engelen, N. C. (2019). "Rotation in rectangular and circular reinforced elastomeric bearings resulting in lift-off." *International Journal of Solids and Structures* 168 (2019): 172-182.
- Van Engelen, N. C., Osgoodei, P. M., Tait, M. J., & Konstantinidis, D. (2014). Experimental and finite element study on the compression properties of Modified Rectangular Fiber-Reinforced Elastomeric Isolators (MR-FREIs). *Engineering Structures*, 74, 52–64. <https://doi.org/10.1016/j.engstruct.2014.04.046>
- Zhou, F. (2015). Earthquake tragedy and application of seismic isolation, energy dissipation and other seismic control systems to protect structures in China. *Energia, Ambiente e Innovazione*, 5:23–30. <https://doi.org/10.12910/EAI2015-077>
- Zhou, F., & Tan, P. (2013). Lu Shan earthquake M7.0 on 2013.4.20 and recent development on seismic isolation, energy dissipation and structural control in China. *Proceedings of 13th World Conference on Seismic Isolation, Energy Dissipation and Active Vibration Control of Structures*. Tokyo.

Appendix A Bonding Levels

The study of bonding levels is shown here. Seven different bonding scenarios for the 5-layer bearings (Bearing 5-1 to Bearing 5-7) and 13-layer bearings (Bearing 13-1 to Bearing 13-7) are modelled, the sketches of the 5-layer bearings are shown in Figure A 1. The solid thick line indicates the elastomeric surface is bonded to the contact support and the dotted line indicates the unbonded connection. Bearing 5-5 and Bearing 5-7 have the upper interaction 25% bonded and 75% bonded, respectively, as shown in Figure A 1 (e) and (g). Note that the bonding condition for the 13-layer bearings are the same with 5-layer bearing, their sketch are not shown.

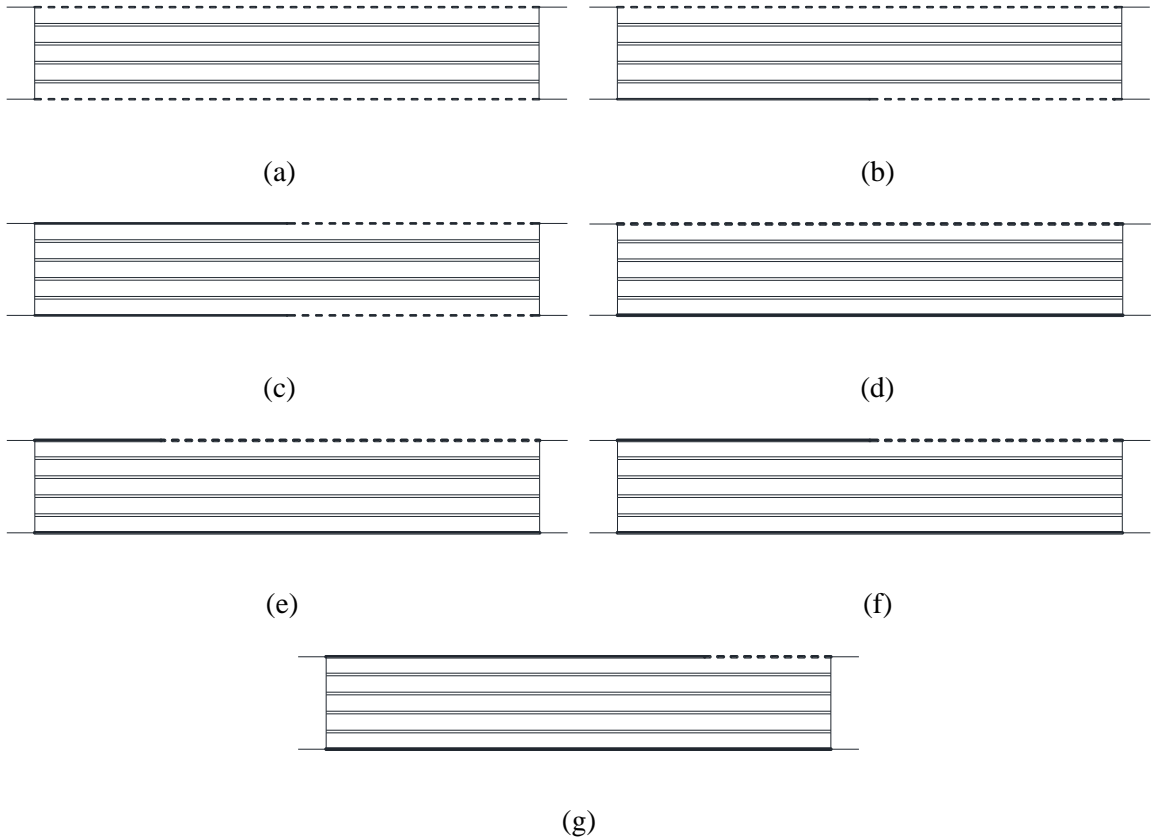
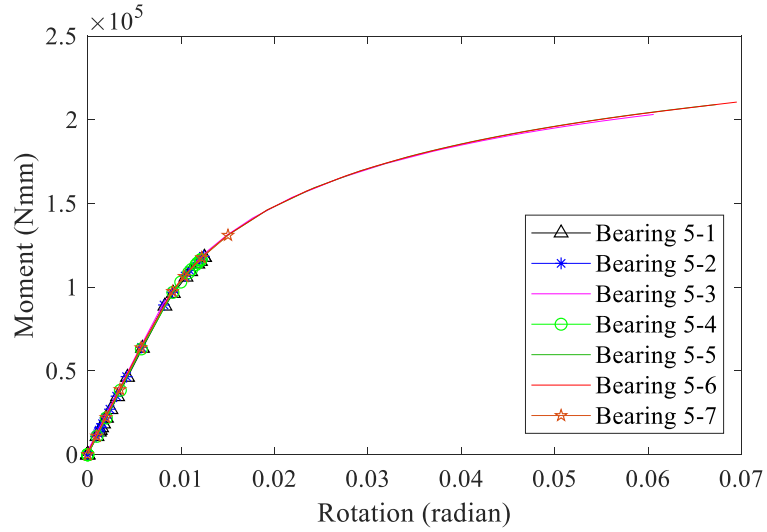
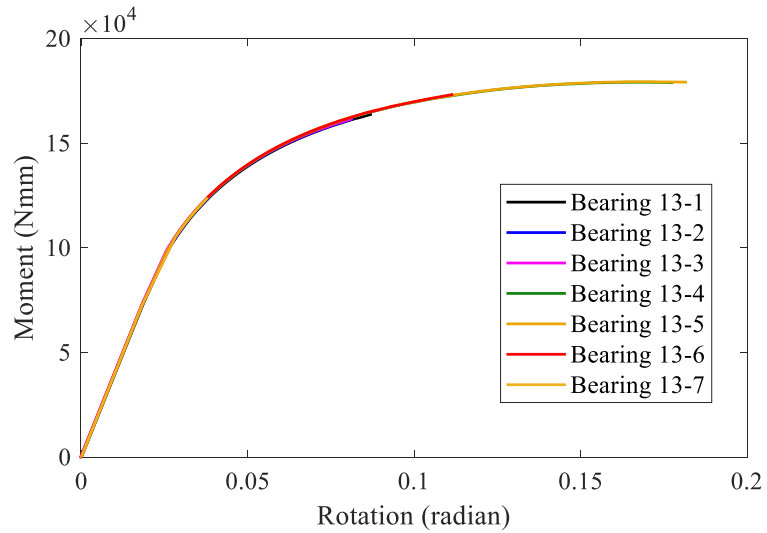


Figure A 1 Sketches of a 5-layer bearing with different bonding levels (a) Bearing 5-1; (b) Bearing 5-2; (c) Bearing 5-3; (d) Bearing 5-4; (e) Bearing 5-5; (f) Bearing 5-6; (g) Bearing 5-7. For 5-layer bearings and 13-layer bearings, 0.1 radians and 0.2 radians rotation are applied, respectively. The magnitude of the rotation was selected to be large enough such that the model

will diverge. The moment-rotation relationship of all the 5-layer and 13-layer bearings are shown in Figure A 2. Note that only the data up to the instant that the lift-off initiation point reaches the point that elastomer is bonded to the upper contact support is considered. The magnitude of the applied rotation when the models diverge are shown in Table A 1 and Table A 2, respectively for 5-layer bearings and 13-layer bearings.



(a)



(b)

Figure A 2 Moment-rotation relationship for different bonding levels of the (a) 5-layer bearing; (b) 13-layer bearing.

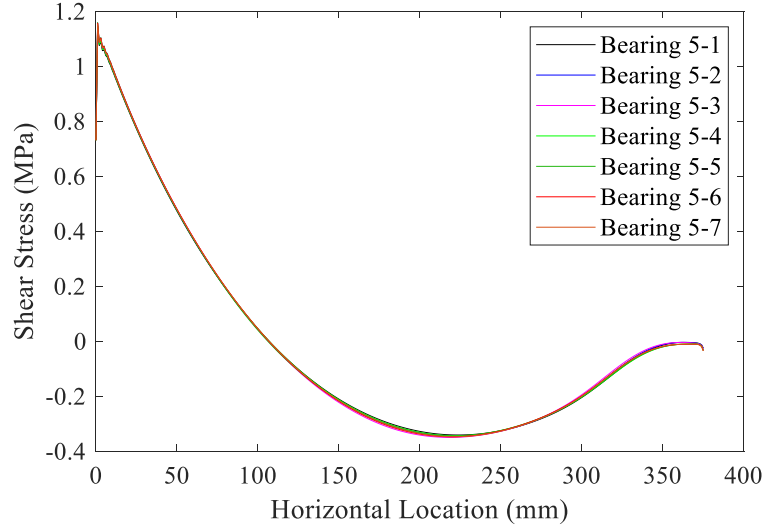
Table A 1 The magnitude of the applied rotation when the 5-layer bearing models diverge

Bearing	5-1	5-2	5-3	5-4	5-5	5-6	5-7
Rotation ($\times 10^{-2}$ radians)	1.25	1.24	6.06	1.21	6.73	6.95	1.50

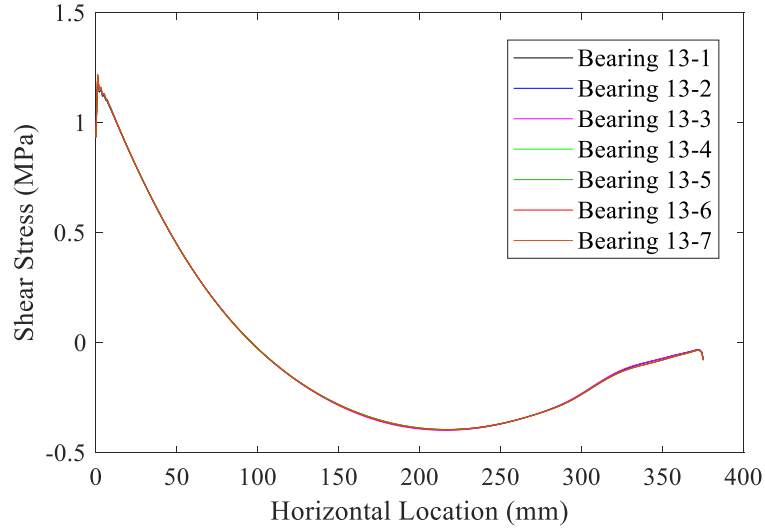
Table A 2 The magnitude of the applied rotation when the 13-layer bearing models diverge

Bearing	13-1	13-2	13-3	13-4	13-5	13-6	13-7
Rotation ($\times 10^{-2}$ radians)	8.72	8.18	8.14	17.78	18.19	11.16	3.79

The shear stress distributions for the upper surface of the second elastomeric layer when rotation reaches 0.01 radians for the 5-layer bearings and 0.03 radians for the 13-layer bearings are shown in Figure A 3.



(a)



(b)

Figure A 3 Shear stress distribution of the second elastomeric layer top surface under specific rotation for different bonding levels of the (a) 5-layer bearing; (b) 13-layer bearing.

There is no significant impact on the results (the curves for different bonding levels overlap) provided the bonding level does not influence lift-off behaviour. But as shown in Figure A 2, the bonding level does influence the divergence of the model. For 5-layer bearings, Bearing 5-6 and Bearing 5-5 reach around 0.07 radians. For 13-layer bearings, Bearing 13-5 reaches the farthest, but Bearing 13-6 diverges early. Based on this result, the bonding scenario of Bearing 5-5 and Bearing 13-5 is to be selected for all the U-FREB model.

Appendix B Deformed Shape and Mesh of FREBs

The deformed shape for all the B-FREBs under 5 MPa compression and 0.01 radians rotation are shown in Figure B 1 and Figure B 2, respectively. The deformed shape for all the U-FREBs under the combination of compression (5 MPa) and rotation (0.01 radians per layer) are shown in Figure B 3. The deformed shape for Bearings U1 to U8 under the combination of compression (5 MPa) and the maximum rotation derived from CSA S6-14 are shown in Figure B 4. The deformed shape for Bearings H1 to H6 under the combination of compression (5 MPa) and the rotation that makes the analytical $\eta = 0.7$ are shown in Figure B 5. The meshing of Bearings B3 and U3 are shown in Figure B 6 and Figure B 7, respectively.

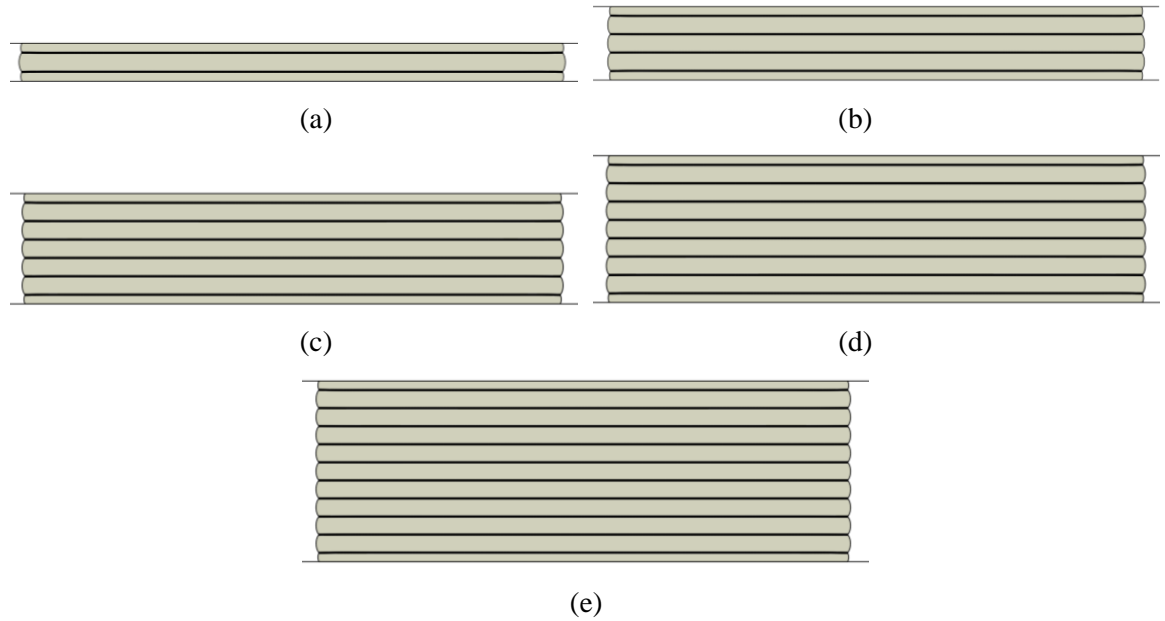


Figure B 1 Deformed shape for Bearing (a) B1; (b) B2; (c) B3; (d) B4; (e) B5 under pure compression (5 MPa).

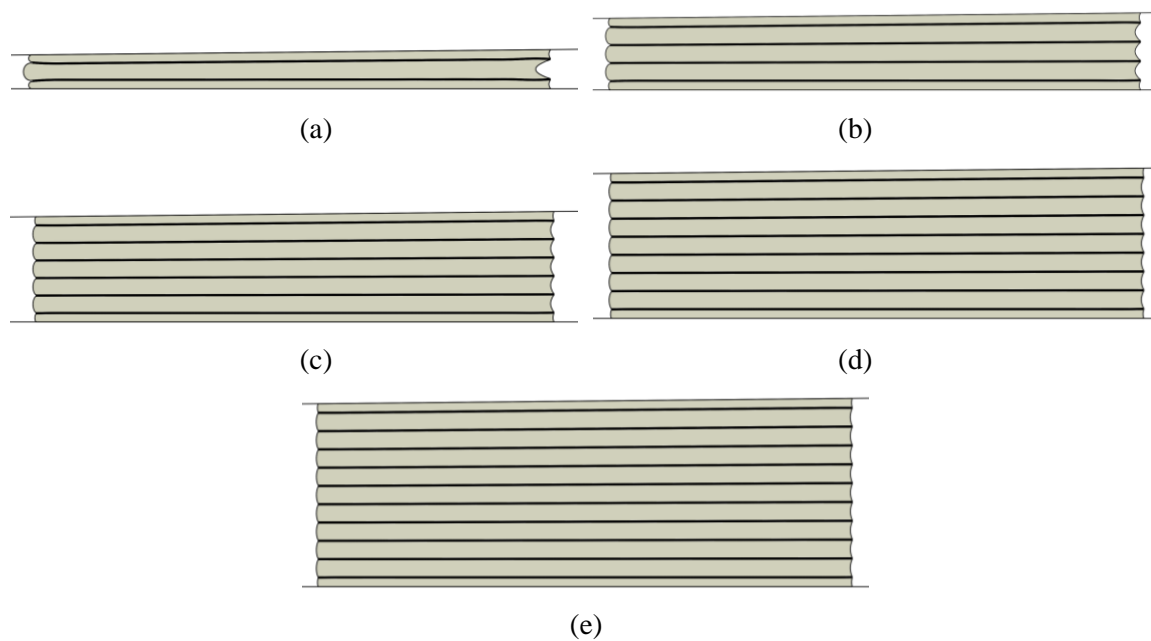


Figure B 2 Deformed shape for Bearing (a) B1; (b) B2; (c) B3; (d) B4; (e) B5 under pure rotation (0.01 radians).

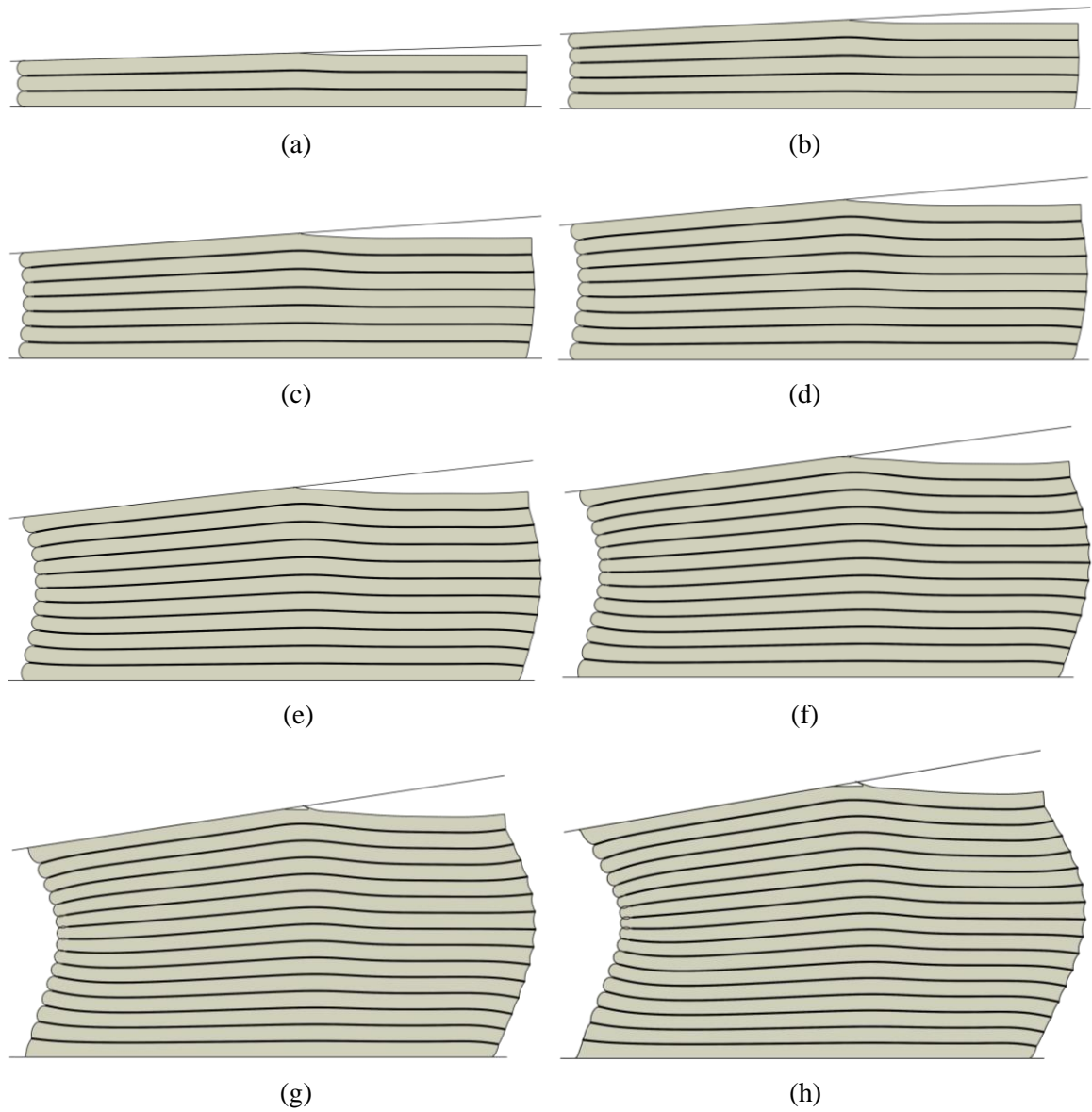


Figure B 3 The deformed shape when under the combination of 5 MPa compression and 0.01-radian rotation per layer for Bearing (a) U1; (b) U2; (c) U3; (d) U4; (e) U5; (f) U6; (g) U7; (h) U8.

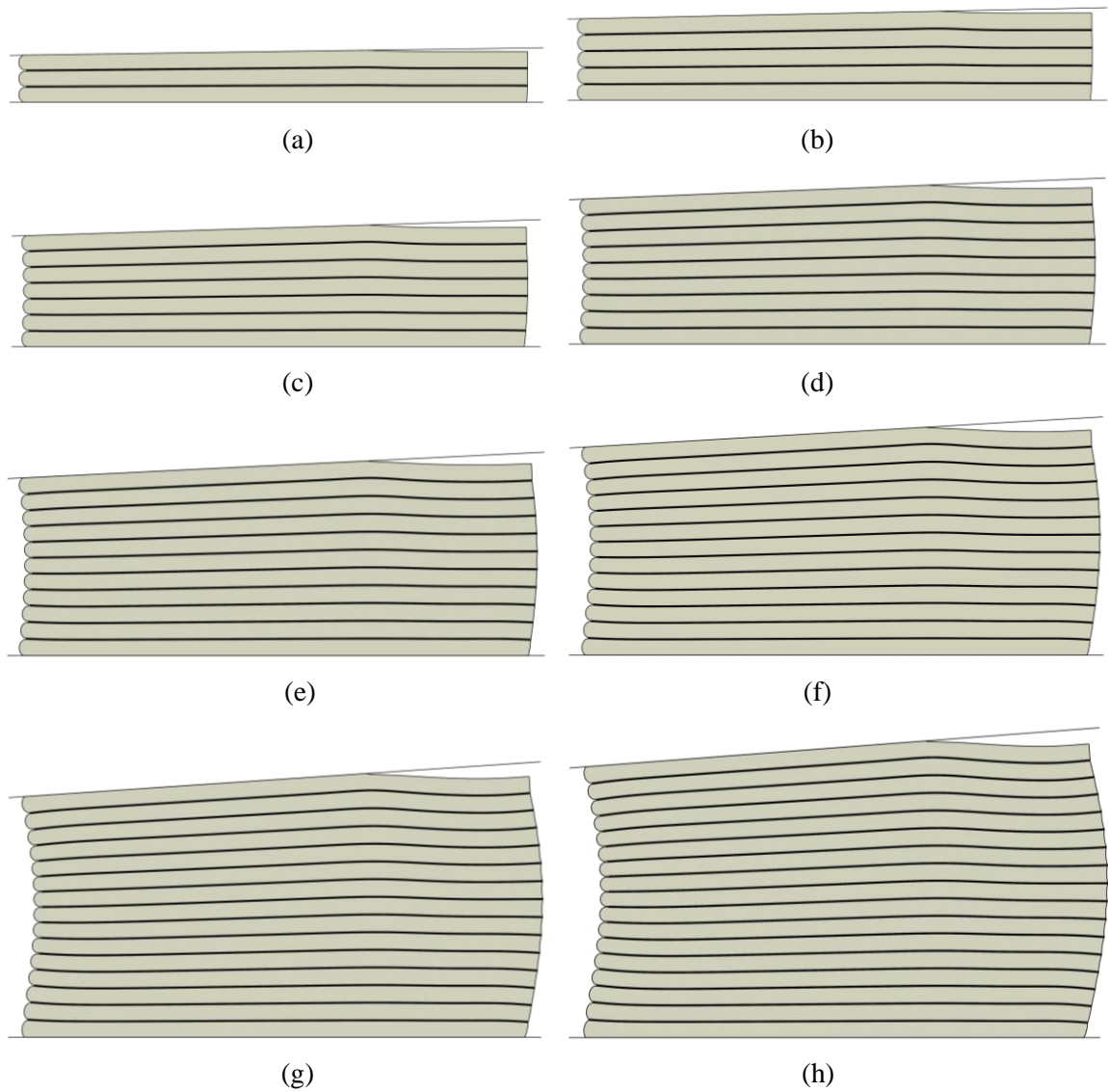


Figure B 4 The deformed shape when under the combination of 5 MPa compression and the rotation that is the maximum from CSA S6-14 for Bearing (a) U1; (b) U2; (c) U3; (d) U4; (e) U5; (f) U6; (g) U7; (h) U8.

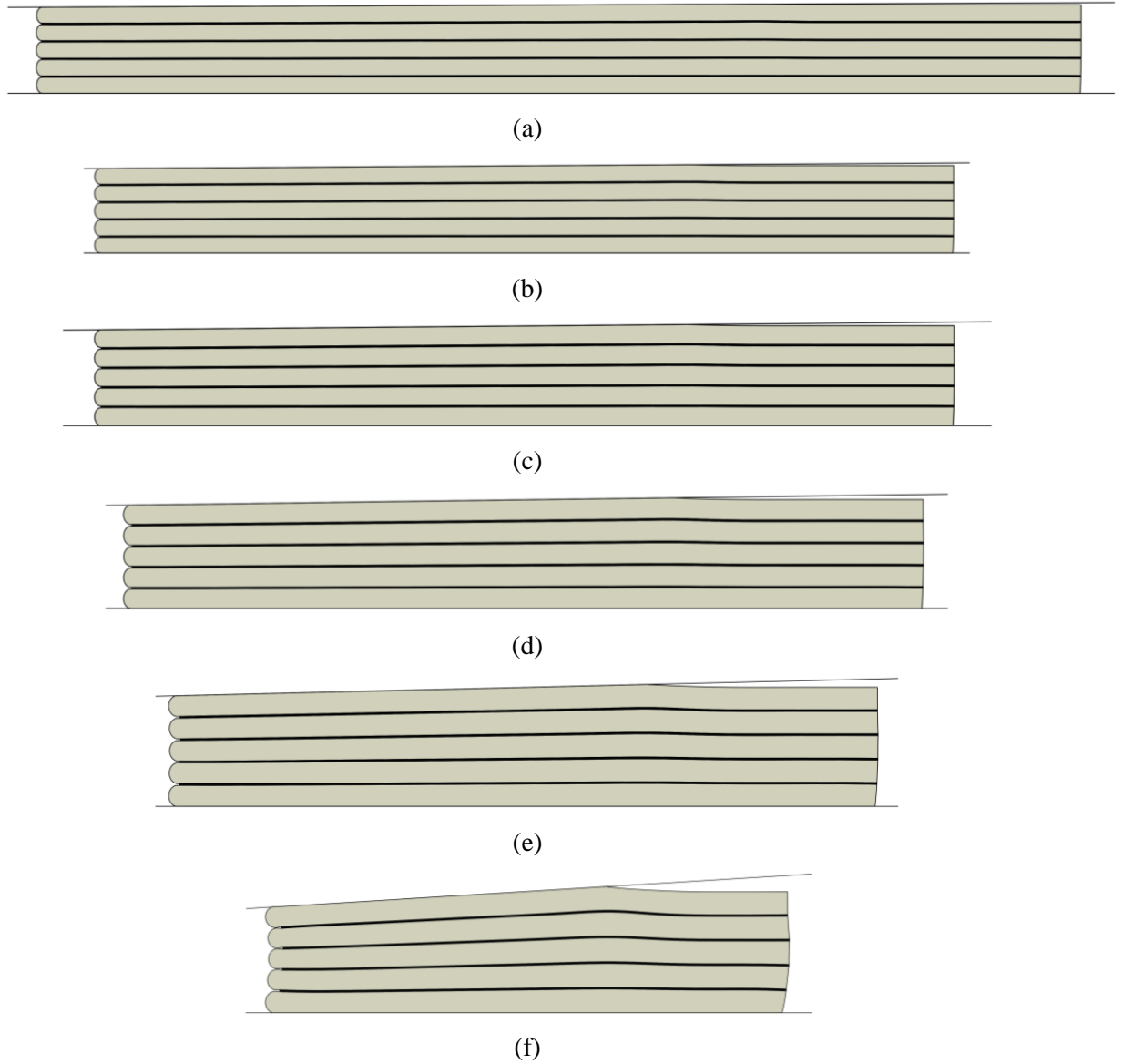
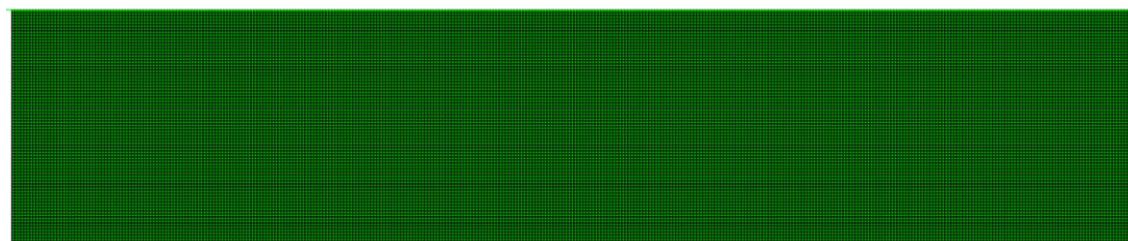
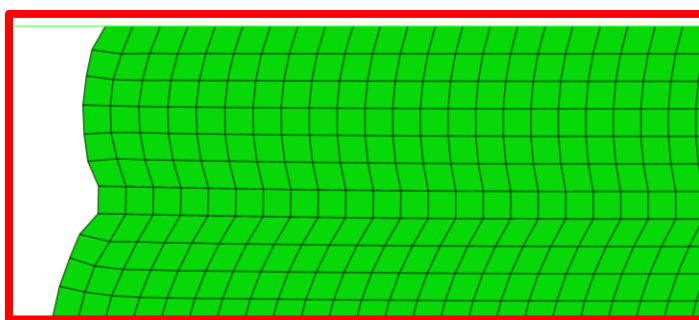


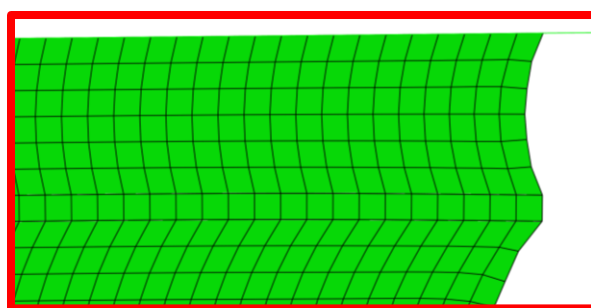
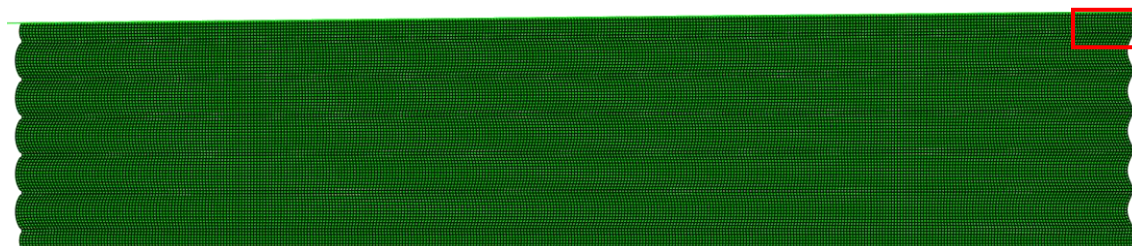
Figure B 5 Deformed shape of Bearing (a) H1; (b) H2; (c) H3; (d) H4; (e) H5; (f) H6 under the combination of 5 MPa compression and the rotation that makes the analytical $\eta = 0.7$.



(a)

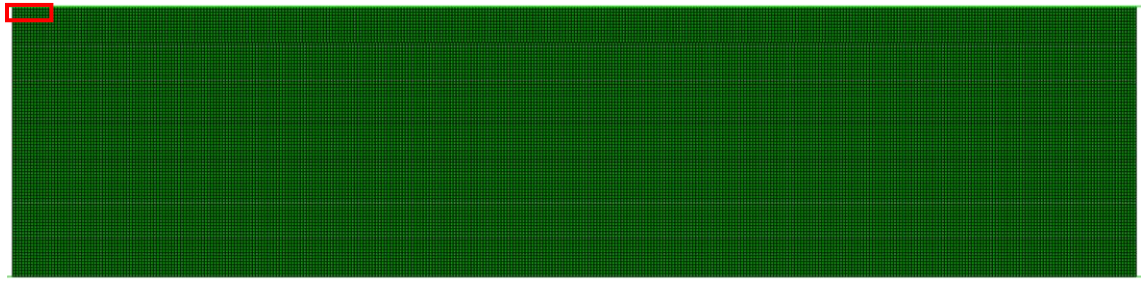


(b)

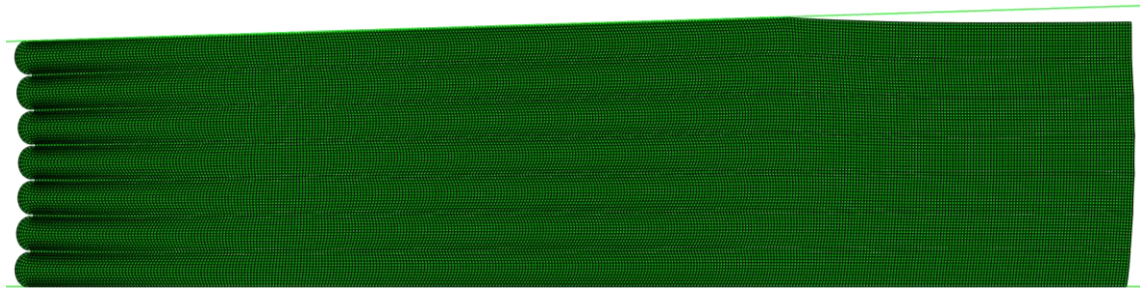


(c)

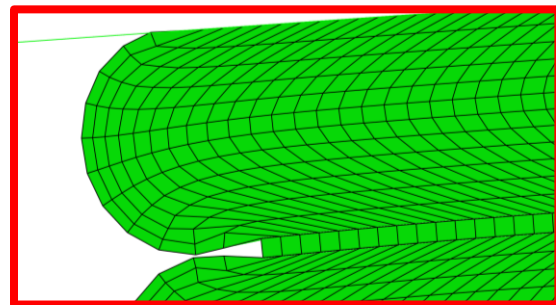
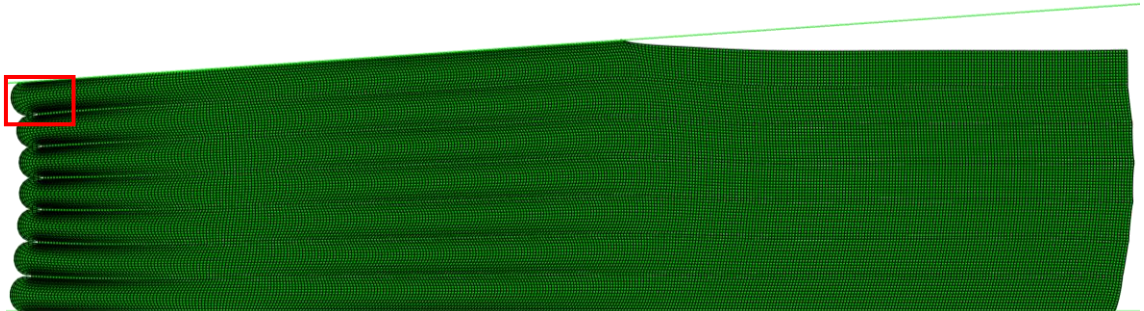
Figure B 6 Meshing of Bearing B3 when (a) no load is applied; (b) under 5 MPa compression; (c) under 0.01-radian pure rotation.



(a)



(b)



(c)

Figure B 7 Meshing of Bearing U3 when (a) no load is applied; (b) under the combination of 5 MPa compression and the maximum rotation based on CSA S6-14; (c) under the combination of 5 MPa compression and 0.01-radian rotation per layer.

Appendix C Results with 0.8 MPa Shear Modulus

If the shear modulus of the elastomer $G = 0.8$ MPa is substituted into the analytical solution for bonded bearings, the comparison with the numerical results are shown below.

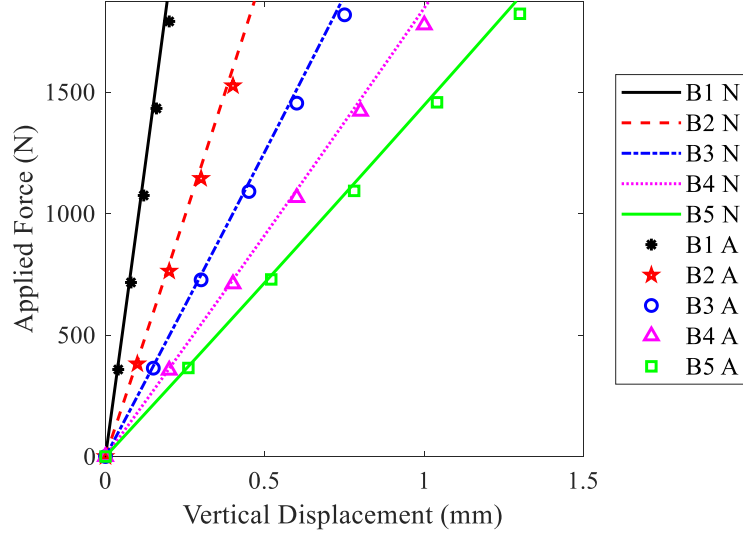


Figure C 1 Force-displacement relationship of B-FREBs.

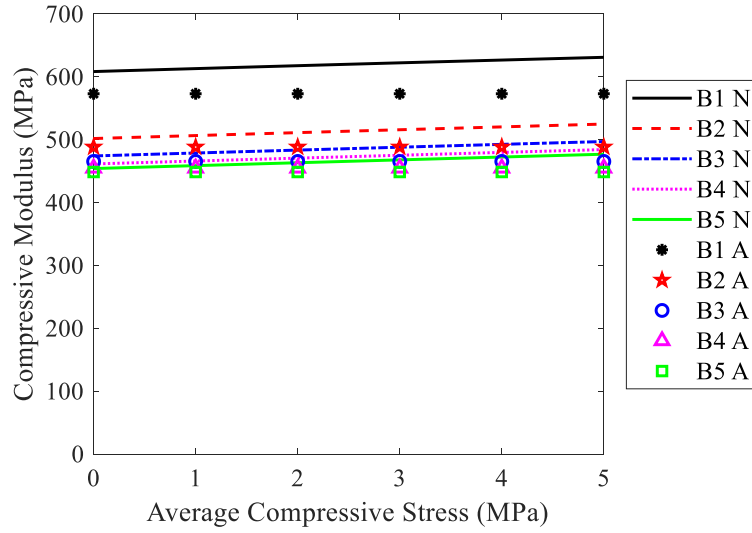


Figure C 2 Compressive modulus under different average compressive stress.

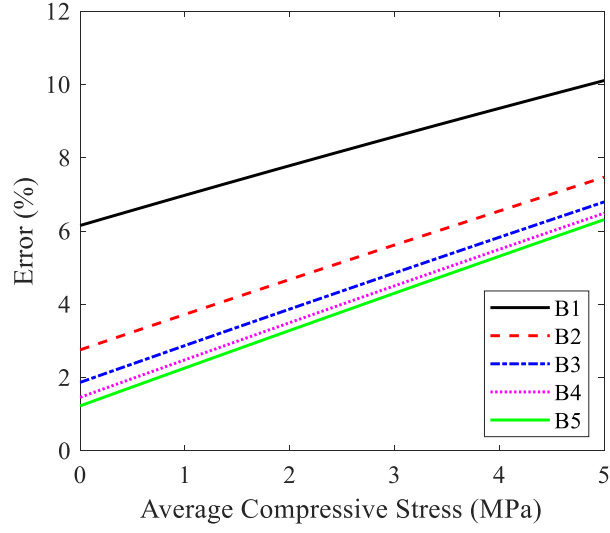


Figure C 3 Error between the numerical results and the analytical solutions of compressive modulus.

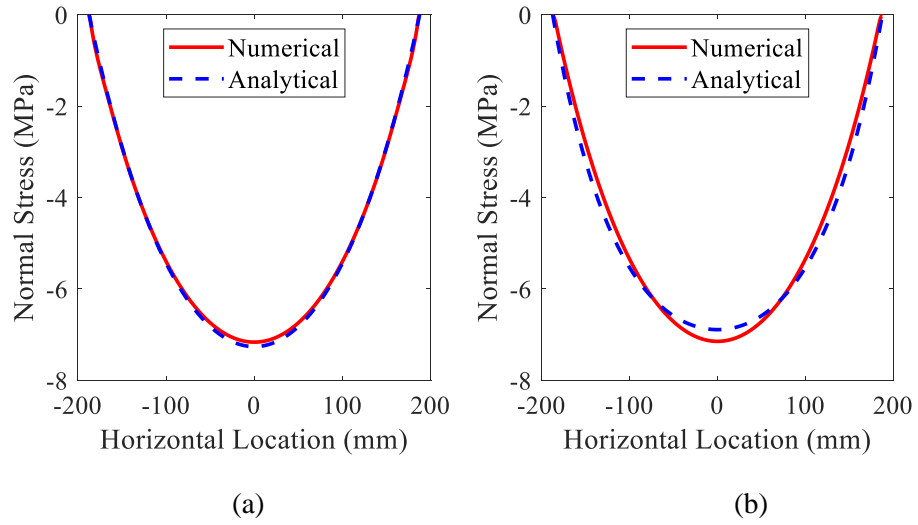


Figure C 4 Analytical and numerical normal stress distribution along the width under pure compression (a) Path-1; (b) Path-2.

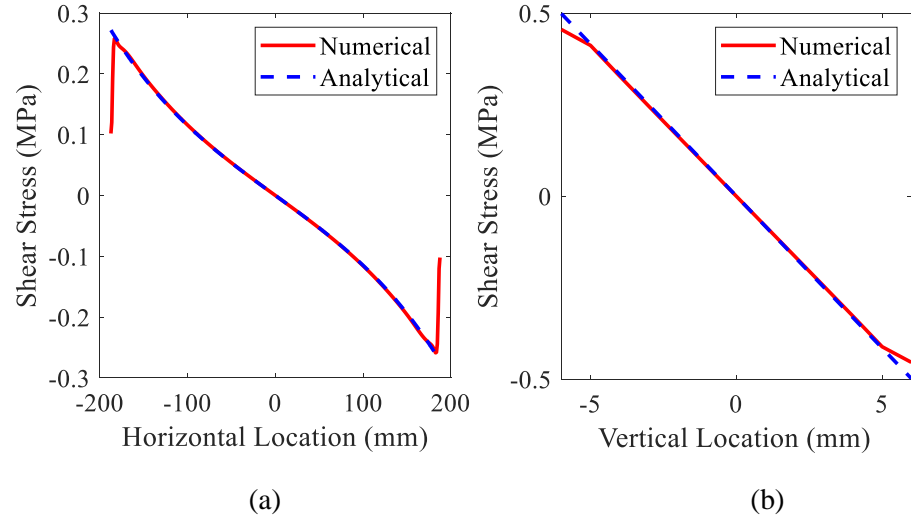


Figure C 5 Analytical and numerical shear stress distribution of the intermediate rubber layer under pure compression (a) Path-3; (b) Path-4.

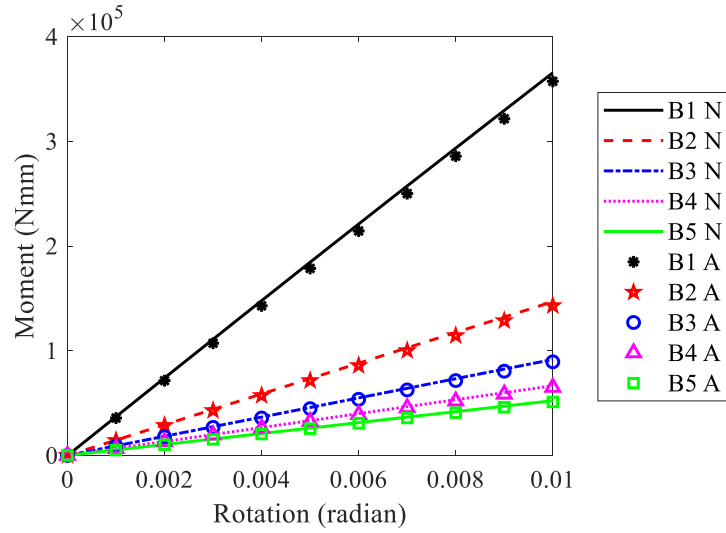


Figure C 6 Rotational behaviour of B-FREBs.

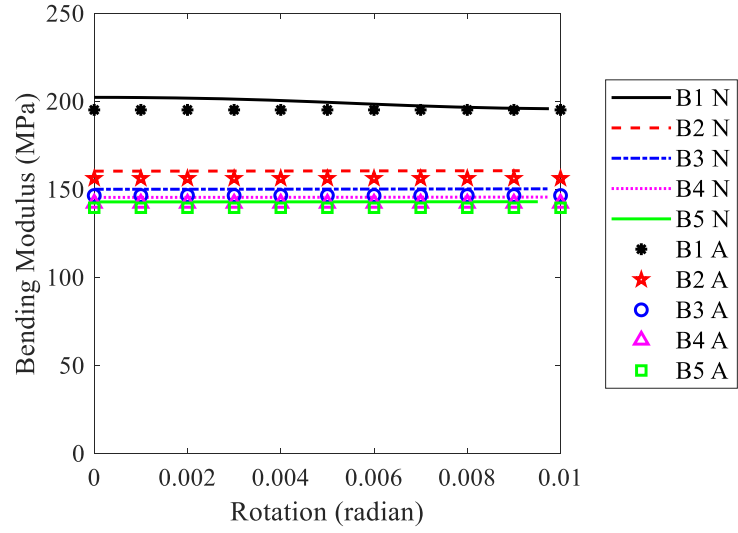


Figure C 7 Bending modulus as a function of rotation.

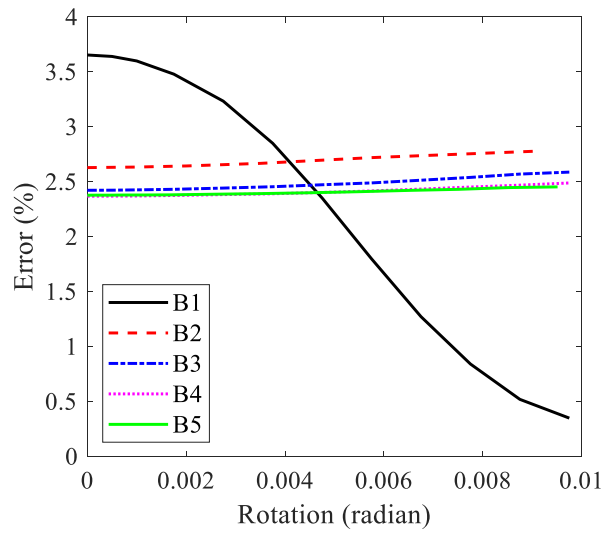


Figure C 8 Error between the analytical solutions and the numerical results of the bending modulus.

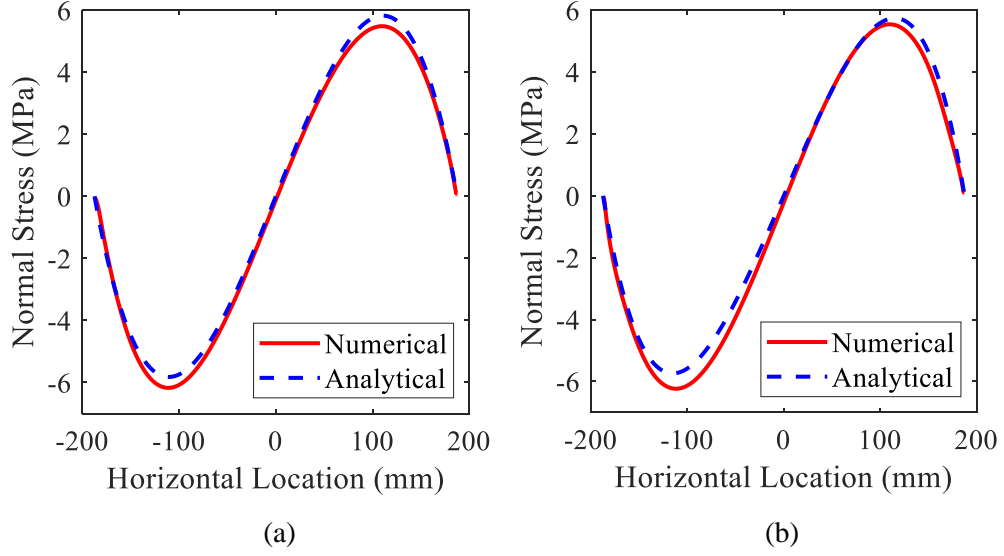


Figure C 9 Analytical and numerical normal stress distribution along the width under pure bending (a) Path-1; (b) Path-2.

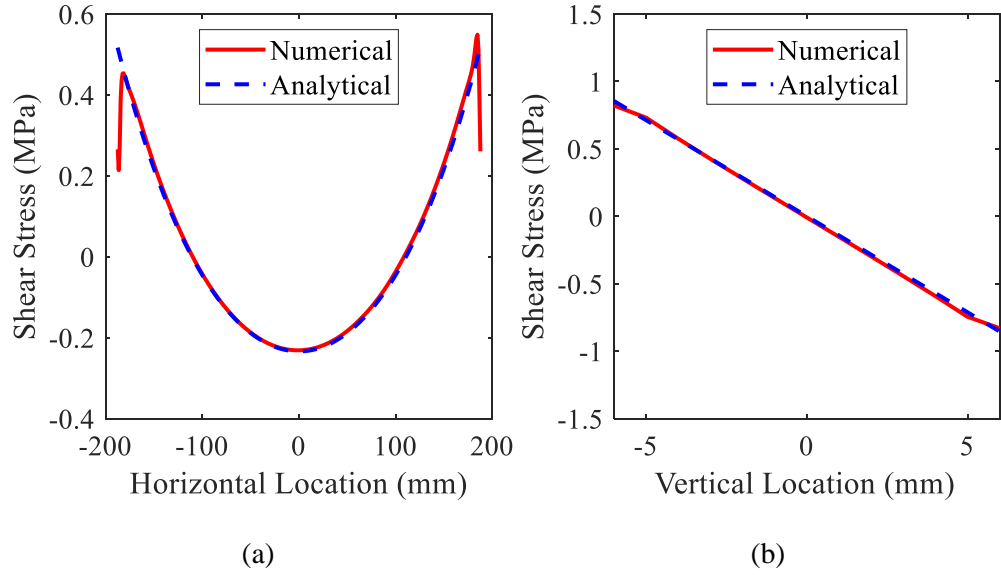


Figure C 10 Analytical and numerical shear stress distribution of the intermediate rubber layer under pure bending (a) Path-3; (b) Path-4.

Appendix D Results for Bearings H1 to H6

The moment-rotation relationship for Bearings H1 to H6 up to the rotation that makes the analytical $\eta = 0.7$ and up to the maximum rotation based on CSA S6-14 are shown in Figure D 1 and Figure D 2, respectively. The shear stress distribution along the top surface of the second elastomeric layer for Bearings H1 to H6 under the rotation that makes the analytical $\eta = 0.7$ and under the maximum rotation based on CSA S6-14 are shown in Figure D 3 and Figure D 4, respectively. The normal stress distribution along the middle path of the second elastomeric layer for Bearings H1 to H6 under the rotation that makes the analytical $\eta = 0.7$ and under the maximum rotation based on CSA S6-14 are shown in Figure D 5 and Figure D 6, respectively.

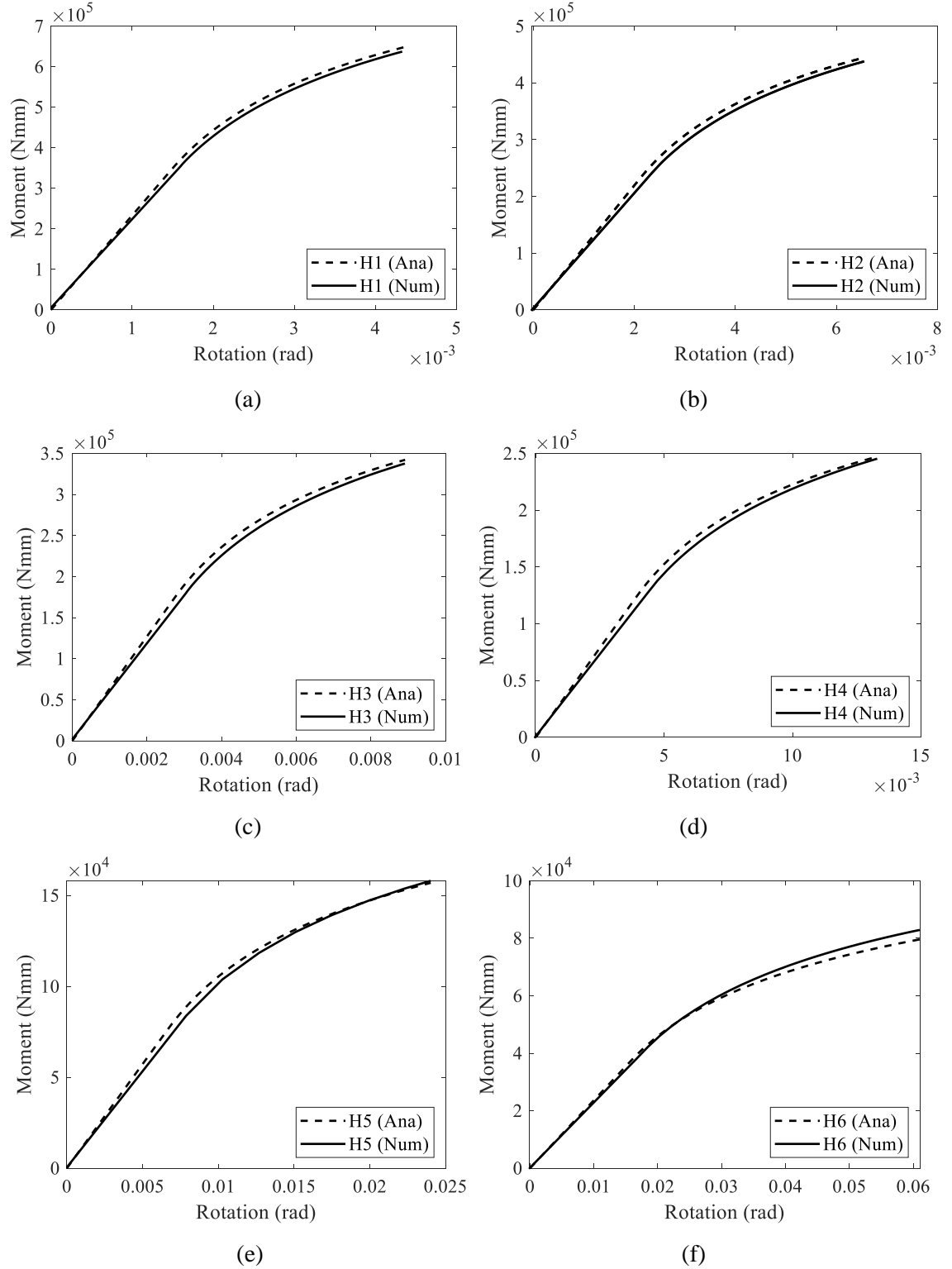


Figure D 1 Moment-rotation relationship for Bearing (a) H1; (b) H2; (c) H3; (d) H4; (e) H5; (f) H6 up to the rotation that make the analytical $\eta = 0.7$.

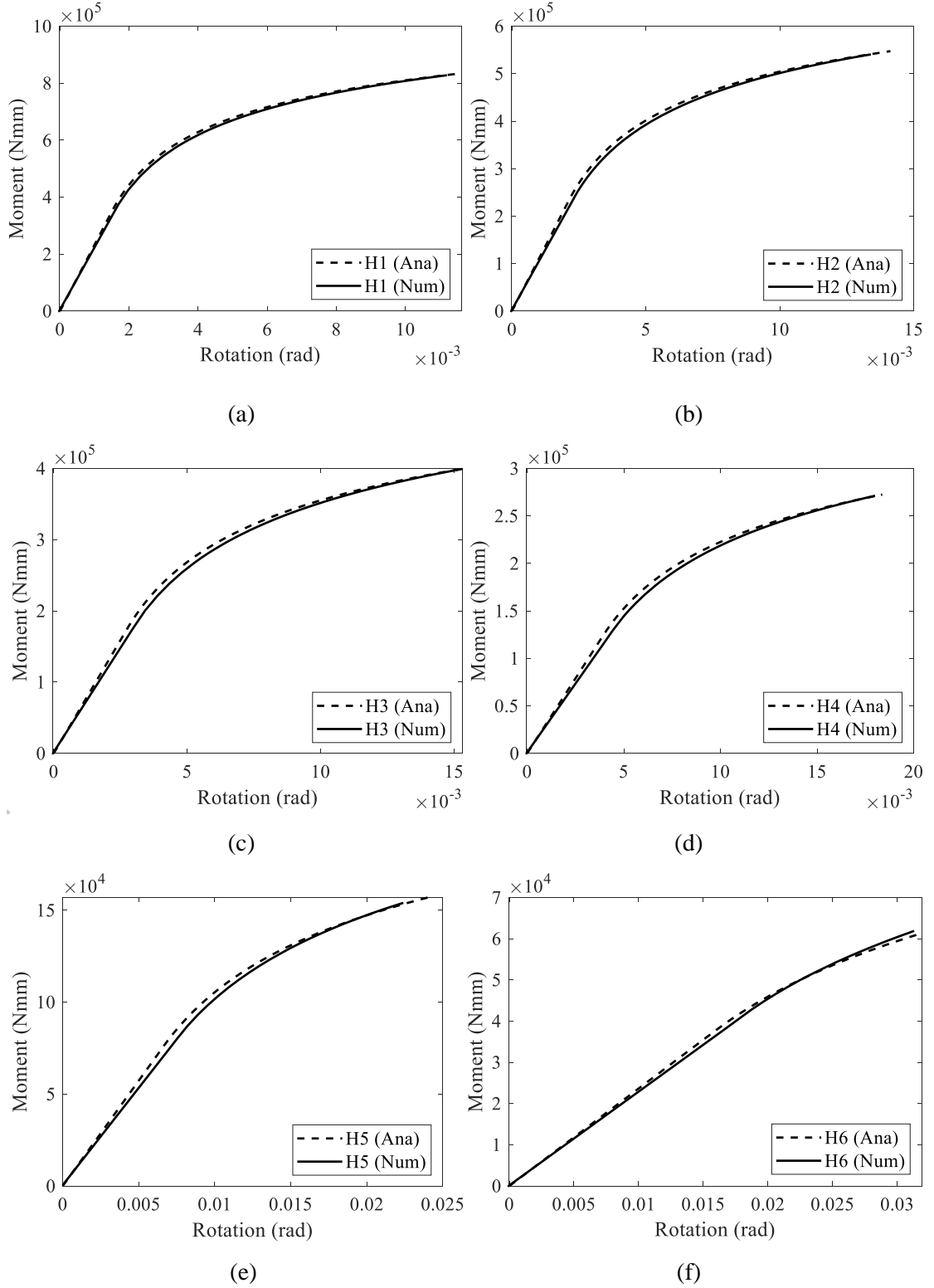


Figure D 2 Moment-rotation relationship for Bearing (a) H1; (b) H2; (c) H3; (d) H4; (e) H5; (f) H6 up to the maximum rotation based on CSA S6-14.

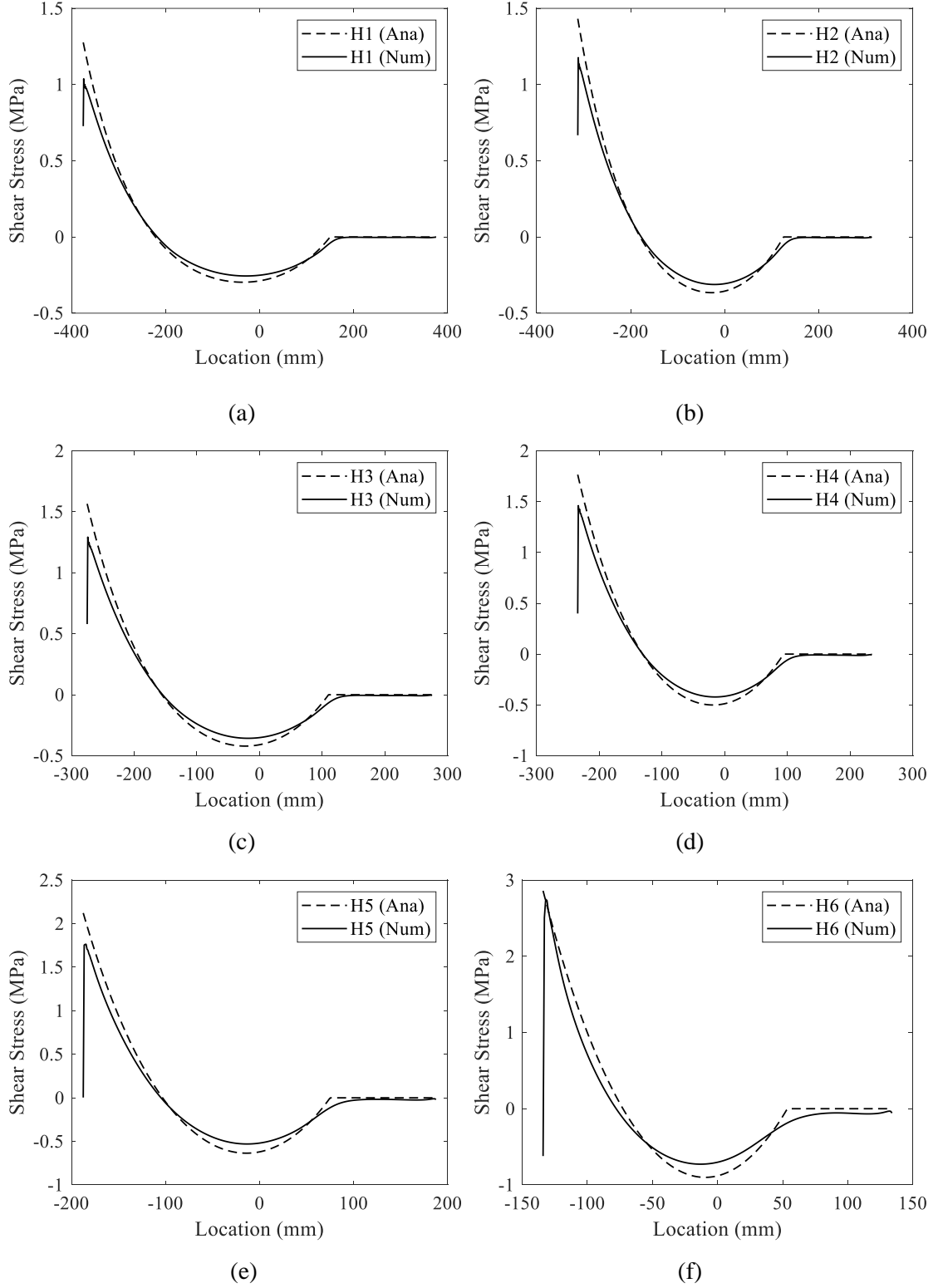


Figure D 3 Shear stress distribution along the top surface of the second elastomeric layer for Bearing (a) H1; (b) H2; (c) H3; (d) H4; (e) H5; (f) H6 under the rotation that makes the analytical

$$\eta = 0.7.$$

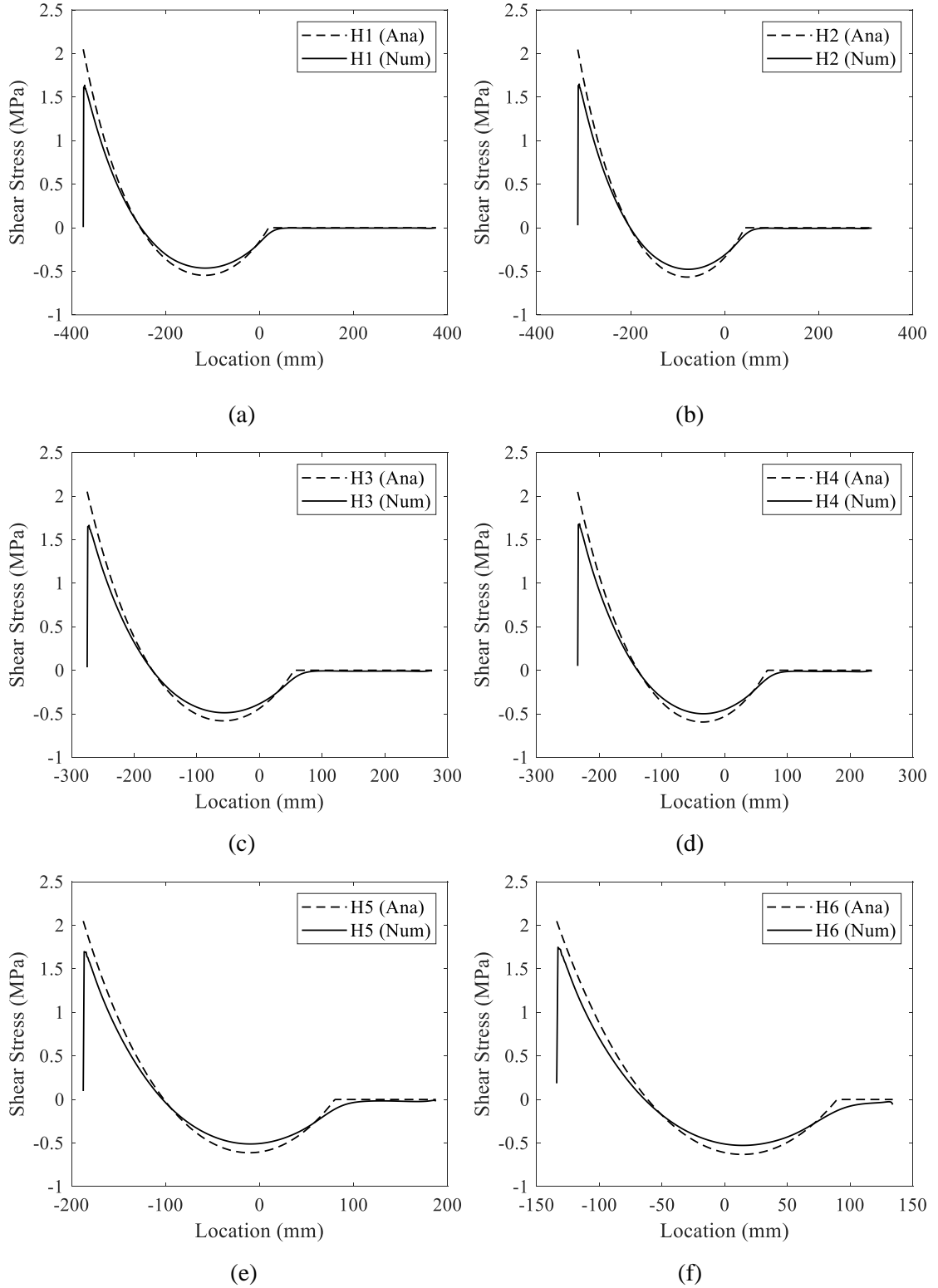


Figure D 4 Shear stress distribution along the top surface of the second elastomeric layer for Bearing (a) H1; (b) H2; (c) H3; (d) H4; (e) H5; (f) H6 under the maximum rotation based on CSA

S6-14.

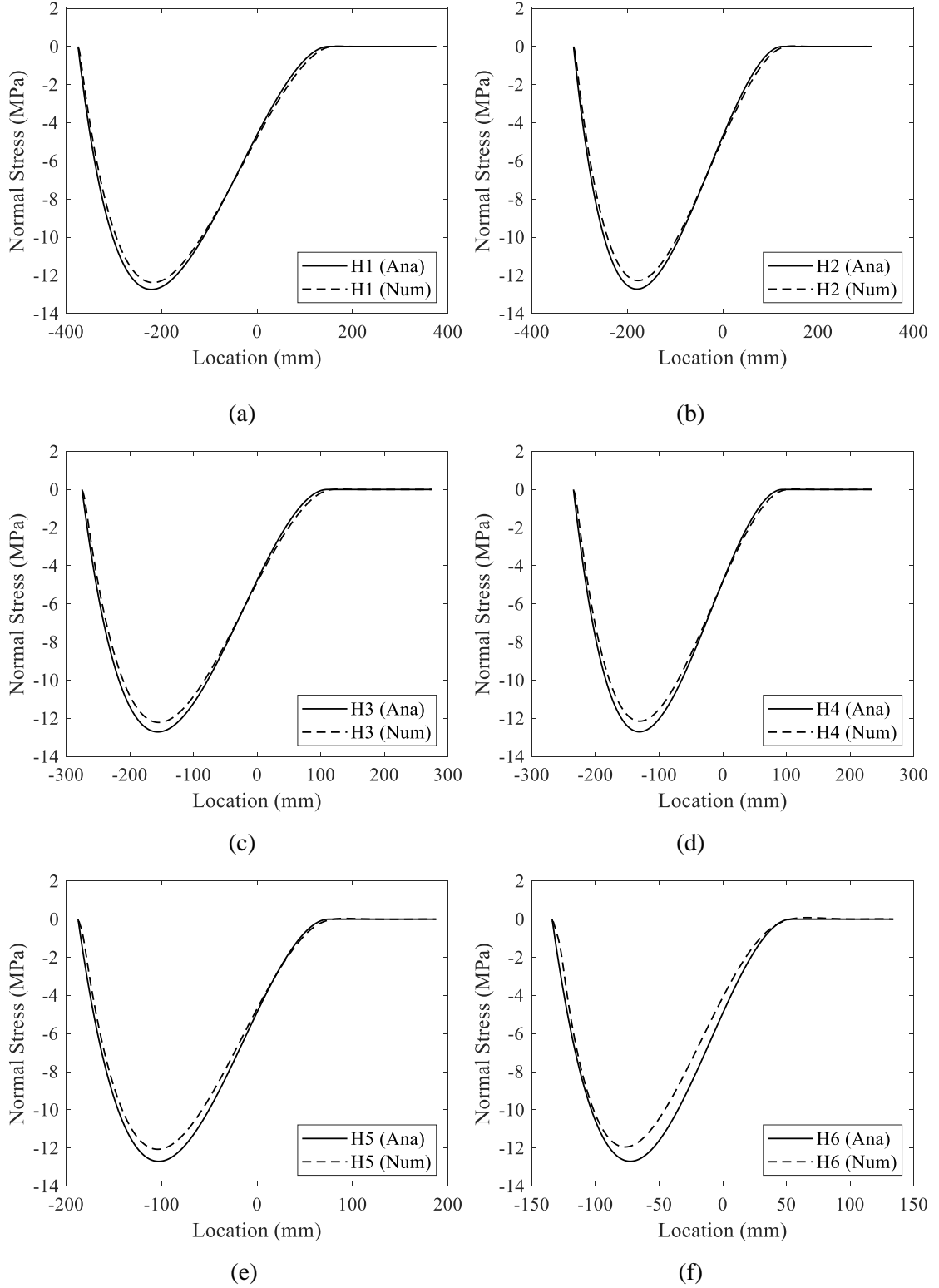


Figure D 5 Normal stress distribution along the middle path of the second elastomeric layer for Bearing (a) H1; (b) H2; (c) H3; (d) H4; (e) H5; (f) H6 under the rotation that makes the analytical

$$\eta = 0.7.$$

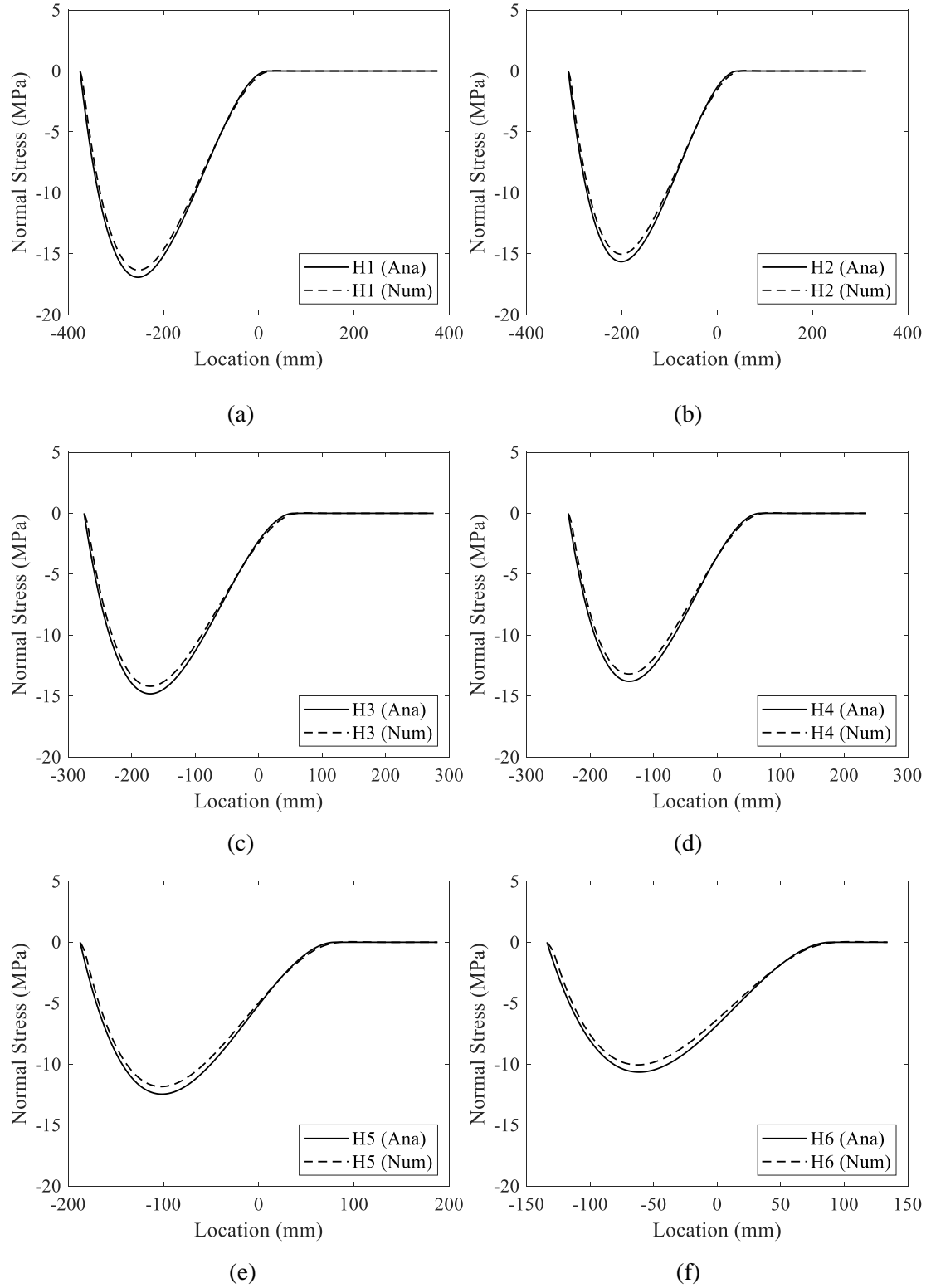


Figure D 6 Normal stress distribution along the middle path of the second elastomeric layer for Bearing (a) H1; (b) H2; (c) H3; (d) H4; (e) H5; (f) H6 under the maximum rotation based on CSA

S6-14.

Appendix E Results for Bearings L1 to L4

The moment-rotation relationship for Bearings L1 to L4 up to a 0.02-radian rotation are shown in Figure E 1. The shear stress distribution along the top surface of the second elastomeric layer and the normal stress distribution along the middle path of the second elastomeric layer for Bearings L1 to L4 under the 0.02-radian rotation are shown in Figure E 2 and Figure E 3, respectively.

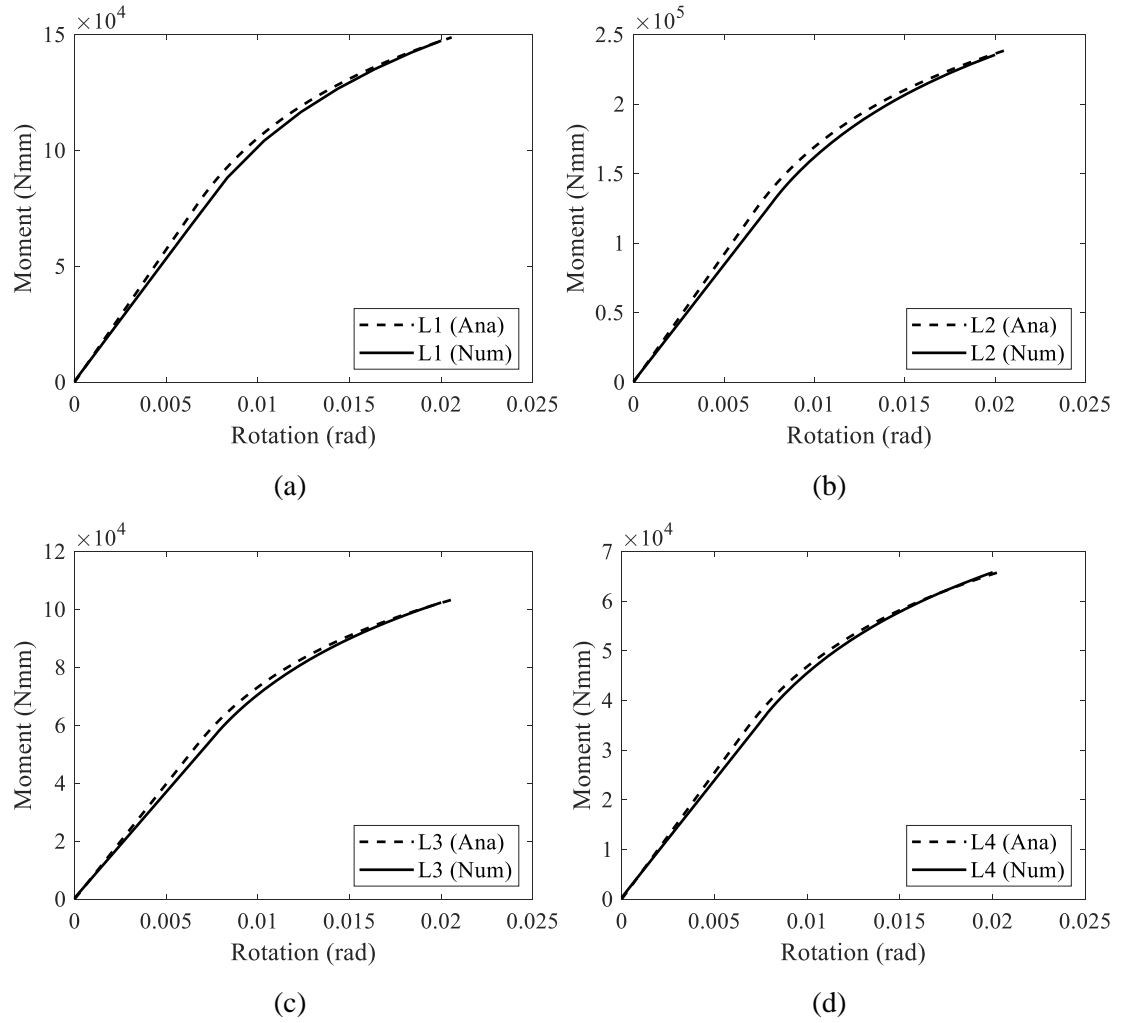


Figure E 1 Moment-rotation relationship for Bearing (a) L1; (b) L2; (c) L3; (d) L4 up to a 0.02-radian rotation.

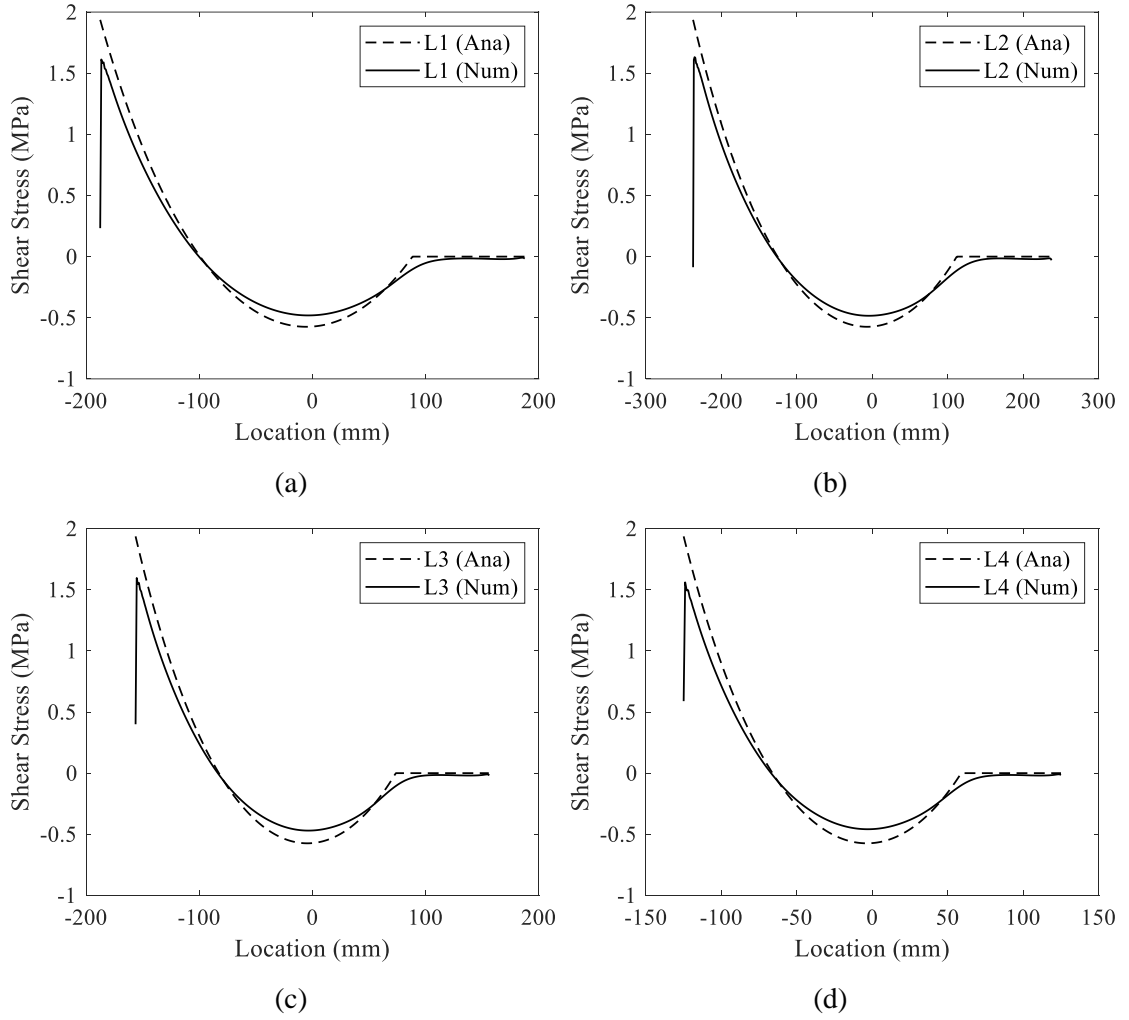


Figure E 2 Shear stress distribution along the top surface of the second elastomeric layer for Bearing (a) L1; (b) L2; (c) L3; (d) L4 under a 0.02-radian rotation.

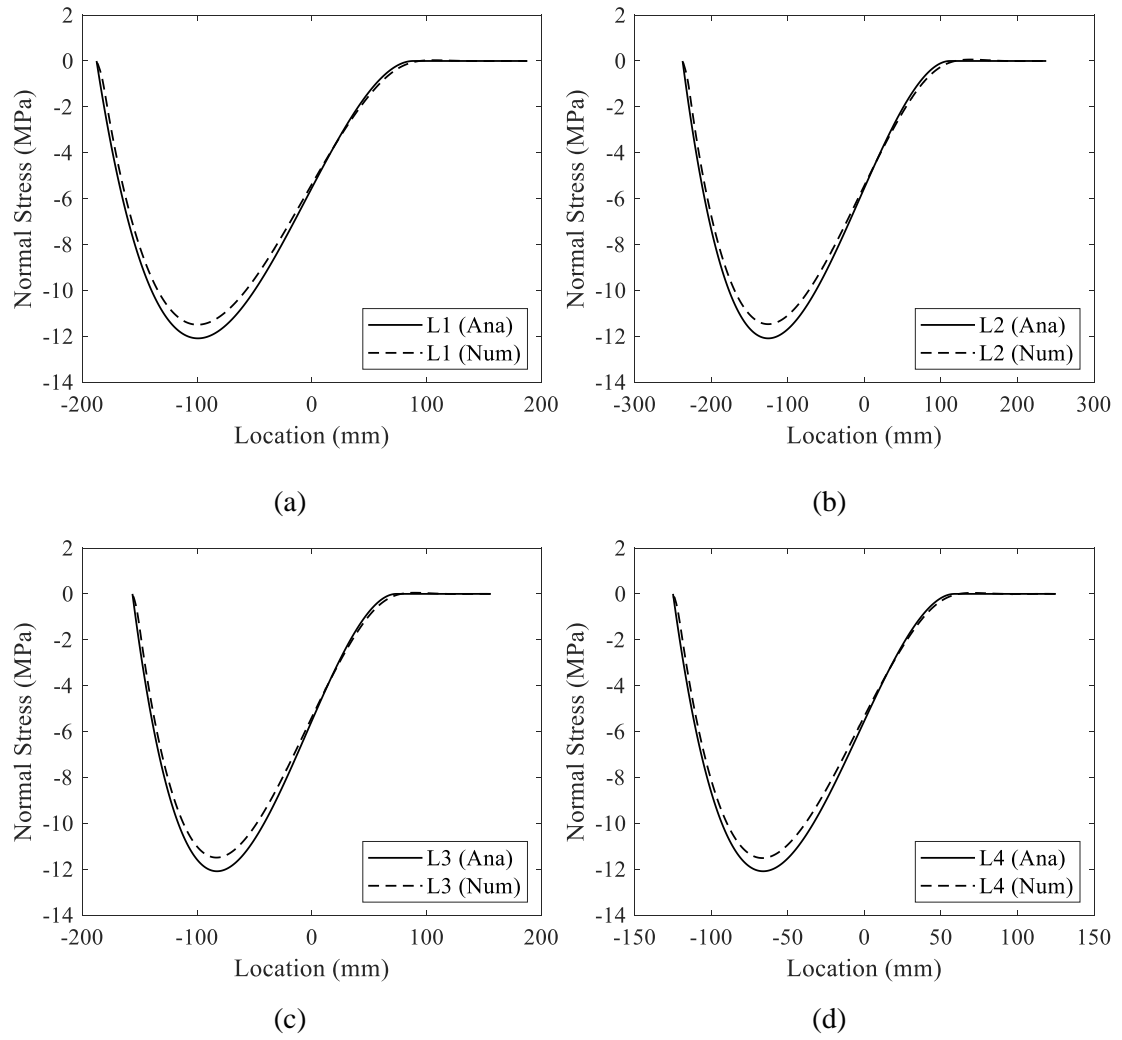


Figure E 3 Normal stress distribution along the middle path of the second elastomeric layer for Bearing (a) L1; (b) L2; (c) L3; (d) L4 under 0.02-radian rotation.

Appendix F Plots after Extrapolation

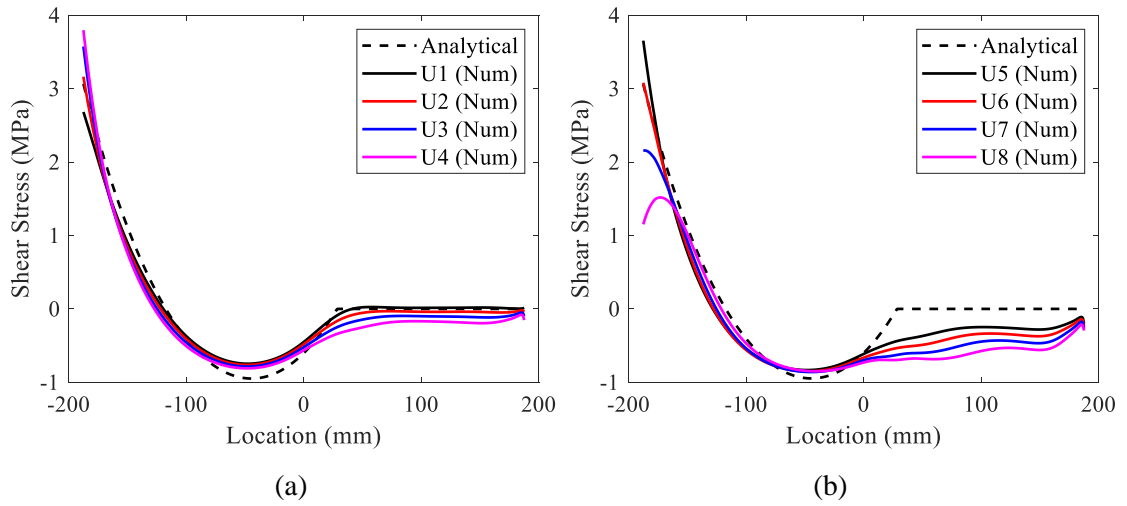


Figure F 1 Shear stress distribution when the rotation per layer is 0.01 radians after extrapolation for (a) Bearings U1 to U4; (b) Bearings U5 to U8

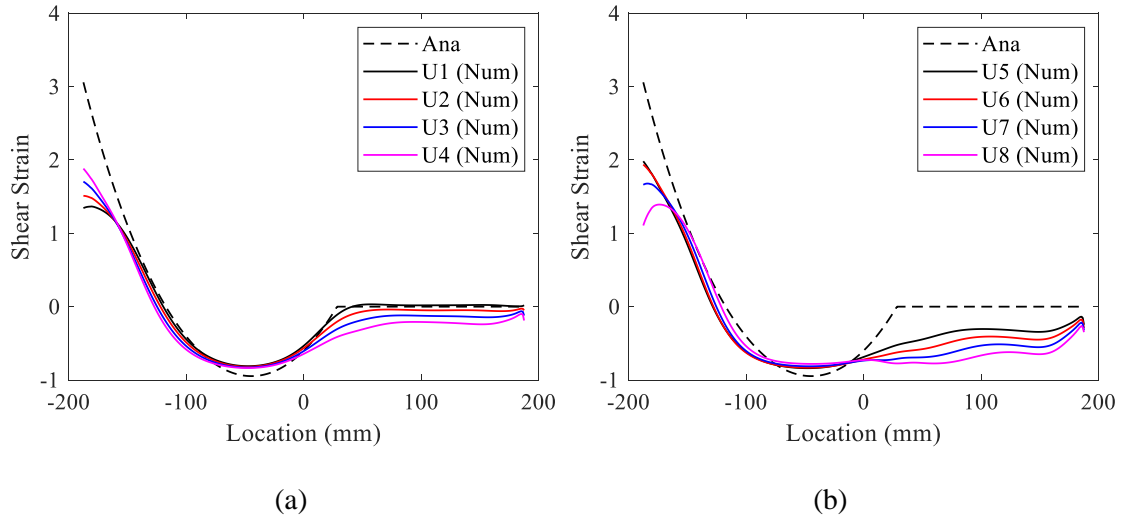


Figure F 2 Shear strain distribution when the rotation per layer is 0.01 radians after extrapolation for (a) Bearings U1 to U4; (b) Bearings U5 to U8.

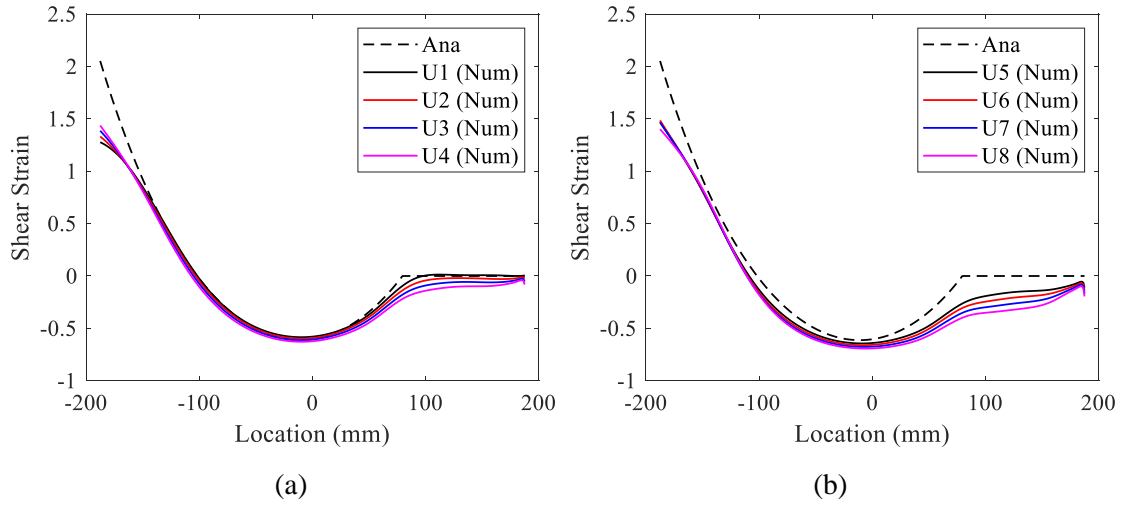


Figure F 3 Shear strain distribution when the rotation is the maximum from CSA S6-14 for (a) Bearings U1 to U4; (b) Bearings U5 to U8.

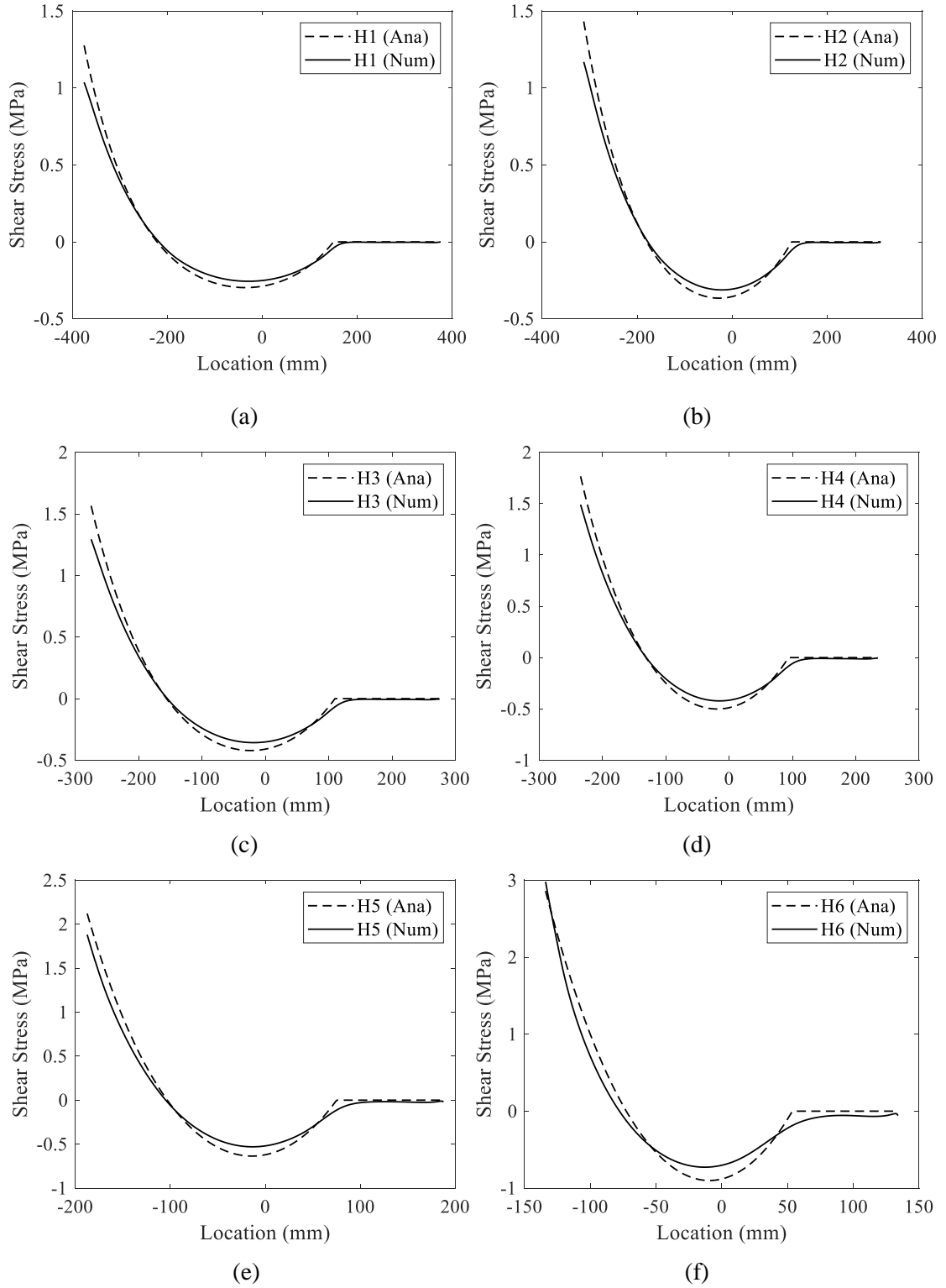


Figure F 4 Shear stress distribution along the top surface of the second elastomeric layer after extrapolation for Bearing (a) H1; (b) H2; (c) H3; (d) H4; (e) H5; (f) H6 under the rotation that makes the analytical $\eta = 0.7$.

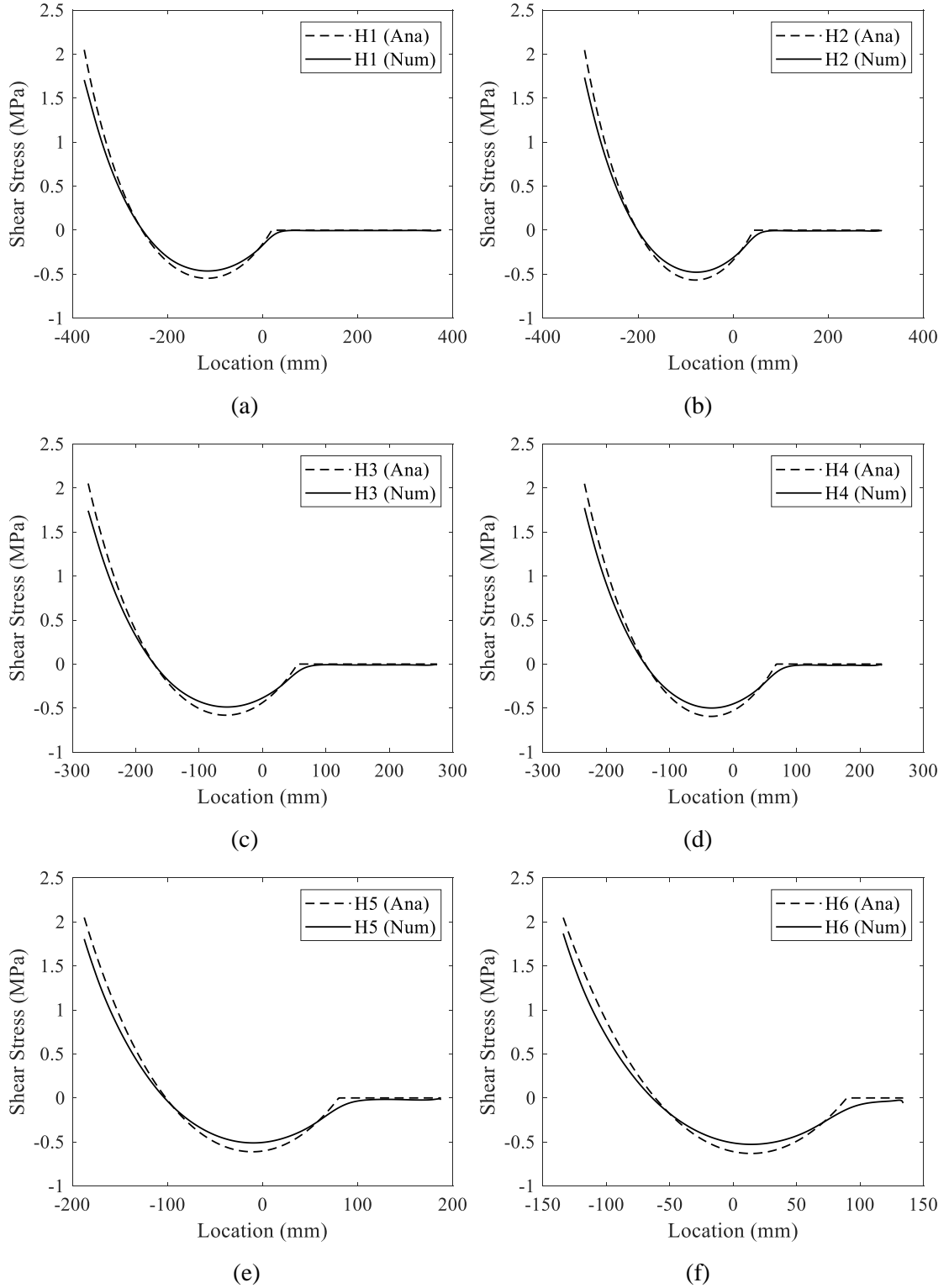


Figure F 5 Shear stress distribution along the top surface of the second elastomeric layer after extrapolation for Bearing (a) H1; (b) H2; (c) H3; (d) H4; (e) H5; (f) H6 under the maximum rotation based on CSA S6-14.

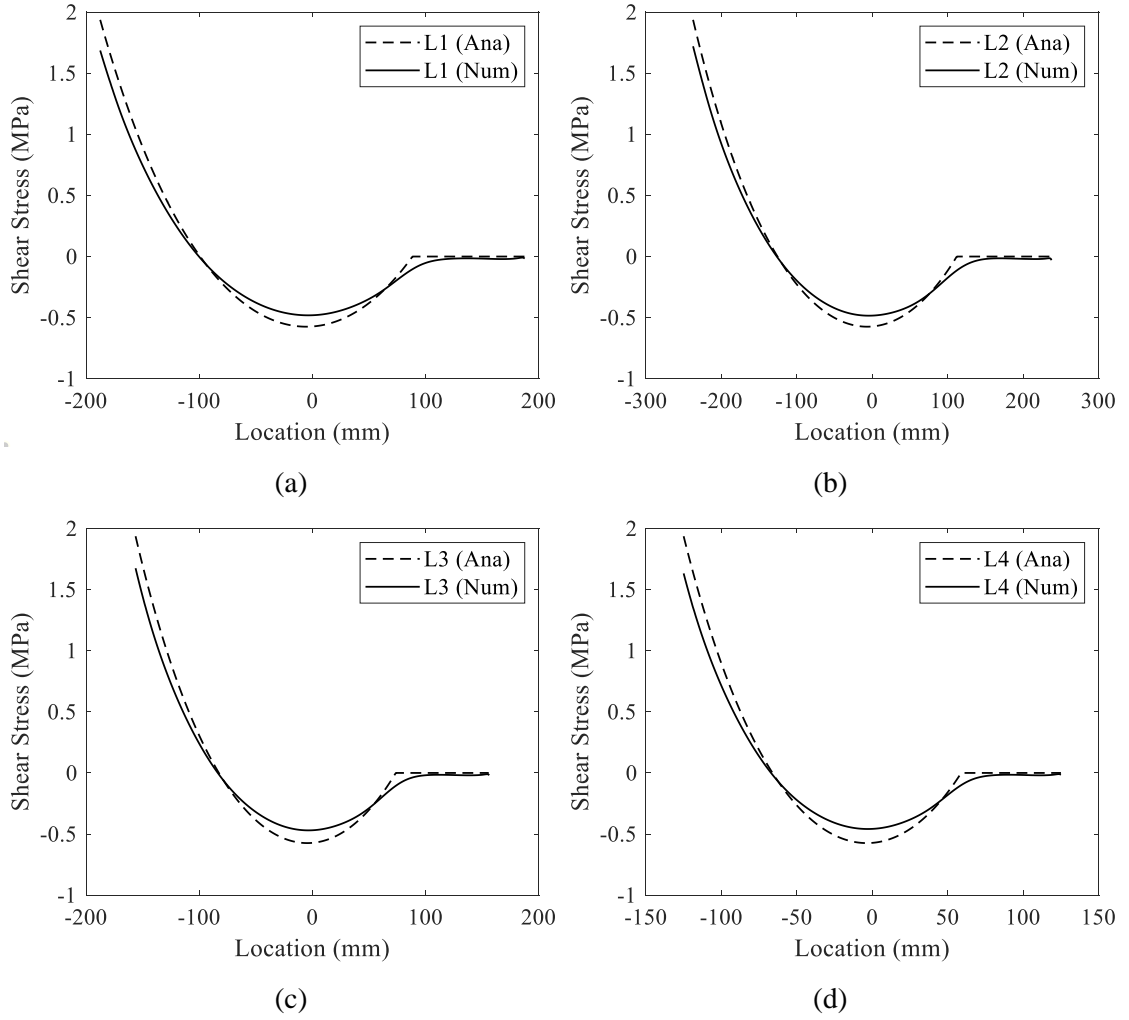


Figure F 6 Shear stress distribution along the top surface of the second elastomeric layer after extrapolation for Bearing (a) L1; (b) L2; (c) L3; (d) L4 under a 0.02-radian rotation.

Vita Auctoris

NAME: Junfu Bai

PLACE OF BIRTH: Anshan, Liaoning, China

YEAR OF BIRTH: 1995

EDUCATION: Angang High School, Anshan 2010-2013

Shengyang Jianzhu University, Shenyang,
Liaohing, China 2013-2017 B.En.

University of Windsor, Windsor, Ontario

2018-2020 M.A.Sc.